8-31-2020

Numerical Modeling of Wave- and Current-supported Turbidity Currents over Erodible Bed

Sahar Haddadian

NUMERICAL MODELING OF WAVE- AND CURRENT-SUPPORTED TURBIDITY CURRENTS OVER ERODIBLE BED

A Dissertation

Submitted to the Graduate Faculty of the
Louisiana State University and
Agricultural and Mechanical College
in partial fulfillment of the
requirements for the degree of
Doctor of Philosophy

in

The Department of Civil and Environmental Engineering

by
Sahar Haddadian
B.S., University of Tabriz, 2011
M.S., University of Tehran, 2013
December 2020

ACKNOWLEDGMENTS

I would like to thank my advisor Dr. Celalettin Emre Ozdemir for his supervision of this work. I am grateful for his valuable suggestions, discussions, and all the opportunities that he has provided me. I also would like to thank my committee members, Dr. Mayank Tyagi, Dr. Clinton S. Wilson, Dr. Frank T. Tsai, and Dr. Giulio Mariotti, for their support and valuable advices along the path of my research.

High-performance computational resources provided by the Louisiana State University (http://www.hpc.lsu.edu) is greatly acknowledged. The support from the Louisiana Board of Regents through research competitiveness subprogram is highly acknowledged. Finally, I would like to thank my parents and my sister, who are always in support of me.

TABLE OF CONTENTS

ABSTRACT

The physical processes that route sediments from nearshore to the continental margin provide vital information to the global assessment of the geochemically important matter and the life in the ocean. Therefore, understanding these processes at the fundamental level will help develop accurate models that can be integrated into operational ocean models. Wave- and current-supported turbidity currents (WCSTCs) are one of the mechanisms that deliver sediments to the continental margin. WCSTCs are slow-moving turbidity currents where near-bed turbulence driven by strong surface waves and/or currents, tide- and/or wind-driven, maintain the turbidity current in motion. This study investigates the along-shelf current-supported turbidity currents (ACSTCs) over an erodible bed, where only the along-shelf current drives the flow, and sediment suspension is sourced from the ephemeral fine sediment deposits. To mimic ACSTCs, direct numerical simulations of a flow in a steady, turbulent, sediment-laden channel with a mild spanwise slope were conducted over an erodible bed. The primary focus of this study is to determine the effect of various sediment settling velocity, erosion parameters, and associated sediment-induced density stratification on total suspended sediment concentration, velocity structure, and turbulent characteristics of the ACSTCs. Specifically, this study aims to analytically and numerically investigates the transition of alongshore current-supported turbidity currents to self-sustaining turbidity currents over erodible seabed composed of fine sediment. Thus, a simplified depth-integrated dynamic equation is developed for suspended sediment concentration. The stability of the developed equation is analyzed both in itself and through temporal linear stability analysis. The analyses find two criteria for the inception of the aforementioned transition. Both criteria indicate that transition is found to reflect the competition between erosion flux, enhanced by the cross-shelf motion of alongshore current-supported turbidity currents, and the deposition flux. In addition, drag coefficient associated with cross-shelf motion of ACSTCs is

formulated as a function of the Reynolds number, sediment concentration, sediment settling velocity, and the bed slope.

1. INTRODUCTION

1.1. OVERVIEW

Turbidity currents are one of the primary sediment transport mechanisms that change marine geomorphology and are one of the conduits of sediment source-to-sink. What drives turbidity currents is the down-slope force created by the excess density of the sediment suspension, where sediments are kept in suspension mainly by the bed-normal turbulent momentum transfer. Due relatively to mild shelf slopes and consequently lack of significant down-slope force to maintain auto-suspension, turbidity currents were generally considered insignificant for the dispersal of sediments over the mild-sloped portions of the continental shelves (Wright and Friedrichs, 2006). However, this paradigm has shifted after the discovery of a new subclass of turbidity currents named wave- and current-supported turbidity currents (WCSTCs). The discovery of WCSTC dates back to the STRATAFORM field observations in the Amazon Delta front (Sternberg *et al*., 1996) which was further supported by the field experiments in the Yellow River mouth and the Eel River shelves (Wright *et al*., 1990, 2001; Ogston *et al*., 2000; Geyer *et al*., 2000; Traykovski *et al*., 2000, 2007). Unlike those that occur at the river mouth and continental margin, WCSTCs are not self-driven and require near-bed turbulence for its maintenance. Strong surface waves -when the depth of closure is sufficiently deep- and/or currents -tidal and/or wind-driven- are the major drivers to agitate and mix the sediment suspension and are therefore the major drivers of WCSTCs (Wright *et al*., 2001; Friedrichs *et al*., 2006).

How WCSTCs are generated and sustained as well as how they differ from auto-suspending turbidity currents, are explained as follows. Over the gentle slopes of the continental shelves, sediment suspension of any source cannot create significant down-slope force. As such, any turbidity current, such as hyperpycnal river plume, entering the mild-sloped portions of the shelves

will conceivably terminate after a runout distance. This is primarily because the turbulence generated by the down-slope motion of the turbidity current is incapable of suspending sediments from the seafloor to balance the sediment settling and thus to sustain its motion. The presence of energetic surface waves increases the closure depth, activating the seabed more towards offshore. Over the active seafloor, wave-associated near-bed boundary-layer turbulence suspends the sediment from the seabed and keeps the cross-shelf moving turbid-layer active. These turbidity currents were observed to be thinner, $\mathcal{O}(0.1\ \mathrm{m})$, and slower, $\mathcal{O}(0.01{\sim}0.5\ \mathrm{m\ s^{-1}})$, compared to auto-suspending turbidity currents. Yet, they can carry fine sediments in substantial amounts. For example, observations of the Trayovski *et al*. (2000) in the Eel River shelves reported the offshore sediment flux of $q = 114\ ton\ \mathrm{s^{-1}}$ by WCSTCs. According to further observations in the Fly River Delta (Ogston *et al*., 2008), Waiapu Shelf (Ma *et al*., 2008), Po Prodelta (Traykovski *et al*., 2007), and sandy Dutch coasts (Flores *et al*., 2018) it is now understood that WCSTCs occur more than that was initially thought.

As will be substantiated in the section that follows, the current state of knowledge on WCSTCs predominantly relies on descriptive information lacking details at the finest scale of their motion. One should note that the finest scale, or the turbulent scale, is particularly essential for the motion of WCSTCs as it dictates the fine sediment suspension. In addition, attempts to quantify WCSTCs (Wright *et al.*, 2001) utilize poorly justified assumptions and parameters that have not been rigorously tested via field, laboratory, and numerical experiments. Therefore, this dissertation focuses on the WCSTC dynamics at its finest scale to address some of the open questions regarding sediment-turbulence interaction. The next section provides a literature survey on WCSTC dynamics.

1.2. MOTIVATION

To point out the knowledge gaps that motivate this study, we review the conceptual studies as well as the field, laboratory, and numerical experiments in this section. As discussed in section 1.1, the discovery of WCSTCs was after the syntheses of the field experiments conducted in the Amazon Delta front (Sternberg *et al*. ,1996), the Yellow River mouth (Wright *et al*., 1990, 2001), and the Eel River shelf (Ogston *et al*., 2000; Geyer *et al*., 2000; Traykovski *et al*., 2000). A conceptual model, in fact, the only model in the literature, was then proposed by Wright *et al*. (2001) by analyzing the data sets collected in the Yellow River mouth and the Eel River shelf. In this model, the downslope component of the submerged weight of the sediment suspension is balanced by the shear force at the bed as

$$\rho_f g(s-1)(\sin\theta)\int_0^h c(z)dz = \rho_f C_d \langle\langle v\rangle\rangle|\langle\langle \boldsymbol{u}\rangle\rangle|, \quad (1)$$

where the left-hand side of the Equation (1) finds the stress due to density difference created by the sediment suspension, and the right-hand side of the equation finds the shear stress at the bed expressed in the form of a modified Chezy equation (Grant and Madsen, 1979; Feddersen *et al.*, 2000). In Equation (1) g is the magnitude of the gravitational acceleration and $s = \rho_s/\rho_w$ is the specific gravity of sediment, with ρ_s being the sediment density and ρ_w being the density of water. In the same equation, h is the thickness of the turbid layer, c is the depth-varying concentration, and θ is the across-shelf bed slope. C_d on the left-hand side of the Equation (1) is the drag coefficient, and $\boldsymbol{u}$ is the velocity vector composed of wave velocity (v_w), along-shelf current velocity (u), and the velocity of the gravity current (v):

$$\boldsymbol{u} = \langle({v_w}^2 + u^2 + v^2)^{\frac{1}{2}}\rangle. \quad (2)$$

Note that plane- and volume-averaged quantities are identified by single and double angle brackets, respectively.

According to previous studies (Howard, 1961; Turner, 1973; Scotti and Corcos, 1972; Eriksen, 1978) and the results of Wright *et al*. (2001), the feedback between flow turbulence and sediment-induced density stratification in a stratified boundary-layer maintains the Richardson number, Ri, close to the critical value of $Ri_c = 0.25$. In detail, when $Ri < 0.25$, increased turbulence suspends additional sediment and increases Ri to the critical value, while for $Ri > 0.25$, due to decreased turbulence, suspended sediments tend to settle and Ri tends to decrease to the critical value again. For the case of stratified boundary-layer, Ri is given as:

$$Ri = g(s-1)\frac{\partial c/\partial z}{(\partial u/\partial z)^2}. \tag{3}$$

Due to the limitations in measuring high suspended sediment concentration inside the turbid layer, Equation (3) is simplified as (Trowbridge and Kineke, 1994)

$$Ri = \frac{\mathfrak{B}/h^2}{\rho_f(\boldsymbol{u}/h)^2}, \tag{4}$$

where

$$\mathfrak{B} = \rho_f g(s-1)\int_0^h c(z)dz. \tag{5}$$

One should note from the above description that the sediment suspension is governed by the erosion/deposition when suspended sediment concentration exceeds or is below a threshold concentration that makes the flow critically stratified. Whether this assumption holds in actual conditions still demands further testing. In addition, the definition of the Richardson number (Equation (4)) in Wright *et al*. (2001) is an oversimplification of stable density stratification without a priori knowledge on the suspended sediment concentration. As such, why the critical Richardson number should be $Ri_c = 0.25$ remains unclear.

Another noteworthy aspect that requires further testing is related to the basis of the drag coefficient to be $C_d \sim 0.003 - 0.005$. The conceptual model proposed by Wright *et al*., (2001)

suggests the value range for the drag coefficient of $C_d \sim 0.003 - 0.005$, based on the experimental study by Van Kessel and Kranunberg (1996) where C_d is evaluated from the flume experiments of unidirectional mud-laden flows. The justification to the selected range of C_d by Wright *et al*. (2001) was that the selected drag coefficient is the limiting value of WCSTCs when WCSTCs become auto suspending or self-accelerating. Quoting Wright and Friedrichs (2006) verbatim, "*…it is also not clear why the range of appropriate drag coefficients (0.002–0.005) determined by others for steady sediment gravity flows should apply equally well to highly unsteady cases. (The work of Wright, Friedrichs, and Scully typically assumed* $C_d = 0.003$ *or* 0.004*.)*" However, it is not clear why $C_d = 0.003 \sim 0.004$ for WCSTCs in the first place. In addition, the variation of C_d with the level of turbulence and the particular characteristics of the near-bed turbulence (such as that occur when waves are alone or when currents are either aligned or normal to the waves) was ignored. Again, quoting Wright *et al*. (2001) verbatim, "*Clearly a more sophisticated formulation for* U_{max} *that accounts for the angle between currents and waves would be slightly more accurate… However, the goal here is to apply the simplest possible model that roughly accounts for the lowest order physical processes.*" Yet, why a model incorporating the angle between waves and currents should only be slightly more accurate remains unjustified. The described concerns regarding the model proposed by Wright *et al.* (2001) mainly stem from the lack of rigorous testing for the proposed model parameters along with the posed assumptions.

The challenge of not being able to test the above-mentioned assumptions arises from that it is not easy to observe WCSTCs in the field. WCSTCs take place due to episodic seasonal storm conditions. In addition, the moving turbid layer is thin, which makes the detailed measurements of the turbidity currents challenging. Variability and/or uncertainty in the driving forces, as well as *in situ* sediment characteristics and field conditions, are also other challenges for rigorous testing

through field experiments. Thus, understanding WCSTCs also requires the knowledge gained from the idealized laboratory and numerical experiments.

In the last two decades, several laboratory experiments on sediment-laden turbulent channel flows have been conducted (Lamb *et al*., 2004; Lamb and Parsons, 2005; Liang *et al*., 2007). These studies are conducted on a wave-sediment U-tube tank that produces turbulent wave boundary-layer with characteristics comparable to that of near the continental shelves, *i.e*., periods of $T \sim 3 - 8\ s$ and orbital velocities of $\omega \sim 15 - 60\ cm\ s^{-1}$. These studies have mostly focused on the interaction between wave boundary-layer turbulence and suspended sediment with a primarily non-uniform silt/clay-sized sediment bed where large concentrations of sediment ($> 10\ g/l$) is suspended. While these studies further our knowledge on the role of wave-induced boundary layer turbulence, however, these studies did not consider the effect of bed slope on the dynamics of the ambient flow and therefore are not simulating wave-supported turbidity currents (WSTCs). Recently, Hooshmand *et al*. (2015) conducted a set of laboratory experiments with the same laboratory setting as Lamb *et al*. (2004) on WSTCs with the focus on the effect of various bed slopes. They investigated the dynamics of WSTCs under different bed slopes and bed sediment characteristics to propose a proper scaling for Richardson number. According to their results, the bulk Richardson number reaches a critical value of $Ri_{cr} = 0.03$, which is about an order of magnitude smaller than the previously proposed critical value of 0.25 for steady flows (Wright *et al*., 2001). However, due to the limitations in laboratory, such as insufficient length of experimental flumes that brings turbulence to the test section, the experimental results are subject to certain errors and further testing is required to validate them. In addition, to the best of the author's knowledge, there is no systematic experimental study focusing on the dynamics of current-supported turbidity currents (CSTCs), as creating a

bidirectional flow in the laboratory is highly complex, if not impossible. Moreover, the state-of-art sensors and instrumentations in the laboratory are still limited to make a detailed quantitative measurement of the wave- and current-induced boundary-layer turbulence. In that regard, high-fidelity numerical simulations become one of the valuable tools to explore the physics of WCSTCs under controlled and idealized conditions.

Over the past few decades, several high-resolution turbulence-resolving numerical studies on sediment-laden turbulent channel flows have been conducted. These studies investigated the interaction between fine sediment suspension and wave boundary-layer turbulence (Hsu *et al*., 2009; Ozdemir *et al*., 2010a, 2011; Cheng *et al*., 2015a, b), which ignored the effect of bed slope. In the numerical study by Ozdemir (2016), a set of idealized numerical simulations were conducted to investigate the internal structure of the WSTCs over a smooth bed with a gentle slope. The effect of variable sediment suspension and bed slope on the interaction between wave boundary-layer turbulence and fine sediments is specifically studied. Later, Ozdemir and Yu (2018) studied the role of sediment settling velocity and suspended sediment concentration on the turbulent characteristics of the WCSTCs due to shore parallel current only, *i.e*., along-shelf current-supported turbidity currents (ACSTCs). By specifying the suspended sediment load constant in each simulation, they investigated the competition between the turbulence-augmenting cross-shelf gravity force and the turbulence-dissipating bed-normal buoyant force as a function of the sediment settling velocity and suspended sediment load. They found that turbulence production due to cross-shelf turbidity current is a quadratic function of the suspended sediment load; whereas, turbulence destruction due to buoyancy is a linear function of the suspended sediment load. It was also observed in the same study that increasing sediment settling velocity increased the buoyant destruction of the near-bed turbulence. By quantifying the normal Reynolds stress budget,

Ozdemir and Yu (2018) observed that when sediment settling velocity gets smaller, and suspended sediment load increases, the cross-shelf current starts generating turbulence more than that created by the shore-parallel current. Hence, for low sediment settling velocity and high suspended sediment load, the flow starts being dominated by the cross-shelf turbidity current and thus tends to become auto-suspending or self-accelerating turbidity current. The findings in Ozdemir and Yu (2018) implicate that the transition of CSTCs to turbidity current in auto-suspension is not solely dictated by the cross-shelf slope but also by the amount of suspended sediment load and the sediment settling velocity. Although valid under specific shelf conditions, such as sediment flux convergence, specifying a constant suspended sediment load may be questioned. Thus, whether the findings in Ozdemir and Yu (2018) is transferrable to a broader range of field conditions, such as when the sediment source is the erosion from the seafloor, needs further investigation. When suspended sediments are sourced from the bed, total suspended sediment load is dictated by the sediment settling velocity, seabed characteristics, and sediment-induced stable density stratification. Therefore, the simulations in Ozdemir and Yu (2018) are enabling in the sense that the role of sediment settling velocity and the suspended sediment concentration on near-bed turbulence destruction and production were assessed individually, which serve as benchmarks for simulations with erodible seafloor conditions.

All the above-mentioned studies are providing the basis for the motivation of this dissertation. These studies provide us with the understanding that WCSTC phenomena needs to be properly parameterized for variables such as drag coefficient, Richardson number, and total suspended sediment concentration. Especially the study of Wright *et al*. (2001) is used as one of the base studies for this dissertation, where the validity of their suggested values for the Richardson number and drag coefficient is analyzed for ACSTCs over an erodible bed. In addition, Wright *et al*. (2001)

proposed a critical value for the bed slope, $\sin\theta = 0.012$, that leads to the transition of CSTCs to self-sustaining turbidity currents. Their finding motivates us to determine all the possible parameters that contribute to the transition of CSTC to a self-sustaining turbidity current. The study of Ozdemir and Yu (2018) implicated that the transition of CSTCs to turbidity currents in auto-suspension is not solely dictated by the cross-shelf slope but also by the amount of suspended sediment load and the sediment settling velocity. The applicability of the results of Ozdemir and Yu (2018) is also tested for ACSTC cases over the erodible seafloor in this dissertation.

Thus, based on the findings of the previous studies focused on WCSTCs, the current state of knowledge lacks the fundamental knowledge of the role of sediment settling velocity and seabed characteristics on WCSTCs, particularly when sediment suspension is sourced from the seafloor. In addition, knowledge on how WCSTC dynamics change under different near-bed turbulence generating mechanisms such as waves and along-shelf currents is still limited. With the given motivations, this dissertation aims at augmenting our understanding of the WCSTC dynamics. Particular focus will be on the erodible seafloor, where WCSTCs are only fed by the sediment suspension from the seabed as in Po River Prodelta (Traykovski *et al*., 2007). Direct numerical simulations (DNS) will be run to conduct a set of virtual experiments, *i.e*., high-fidelity numerical simulations, to assess the physical processes involved in the dynamics of WCSTCs driven by shore-parallel currents only. This dissertation aims to augment the findings of the previous studies and existing models on WCSTCs, improve the parameterization of WSTCS, and take a step forward to mechanically explain the transition of CSTCs to self-sustaining turbidity currents.

1.3. OVERALL GOALS AND OBJECTIVES

The main objective of this study is to investigate the role of shore-parallel currents on the dynamics of WCSTCs and the resultant sediment transport, where sediment suspension is allowed

through sediment mass exchange at the bed, *i.e.*, erodible bed. This study aims to address the effects of various sediment settling velocity and bed erosion characteristics, *i.e.*, critical bed shear stress of erosion and erosion coefficient, on the dynamics of along-shelf current-supported turbidity current (ACSTCs).

Chapter 3 aims to investigate the effect of various sediment settling velocity on flow characteristics of the WCSTCs due only to shore-parallel currents in the absence of waves, *i.e.*, ACSTCs. According to the previous studies (Winterwerp, 2001; Ozdemir *et al.*, 2011; Cantero, 2012; Shringarpore *et al.*, 2012; Ozdemir and Yu, 2018), increasing sediment settling velocity enhances density stratification through increasing the gradient of suspended sediment concentration. Increasing sediment settling velocity also limits the sediment erosion from the bed and hence decreases the density stratification. Augmentation of the near-bed turbulence by ACSTC with increasing suspended sediment concentration further complicates the role of sediment settling velocity. More specifically, with the decrease in sediment settling velocity, the increase in sediment suspension augments the downslope force and, thus, boundary-layer turbulence. Meanwhile, augmented boundary-layer turbulence erodes sediments from the seabed and results in additional sediment suspension. Thus, it can be hypothesized that a positive feedback loop between suspended sediment concentration and flow turbulence exists that continues until ACSTC transitions to a turbidity current in auto-suspension mode. It can also be counter-hypothesized that the increasing sediment concentration enhances stable density stratification and can, therefore, inhibit turbulence growth and even terminate the ACSTC through laminarizing the flow. Thus, the main question to be answered in this chapter is whether the change in sediment settling velocity can lead to the possible transition of ACSTC to a self-driven turbidity current or the termination

of ACSTC by flow laminarization. The threshold flow/sediment characteristics for each of these scenarios to hold true are further studied in this chapter.

Chapter 4 aims to investigate the velocity structure of a miniature along-shelf current supported turbidity current created via sediment suspension over erodible bed. One of the poorly understood aspects of ACSTCs is their velocity structure which is central to quantifying the amount of sediments carried by them. This chapter investigates the velocity structure of such flows and its parameterization in ACSTCs by conducting fine-scale numerical simulations. One of the objectives herein is to analyze the effect of various sediment concentration, sediment settling velocity, and bed erosion parameters on the velocity structure of ACSTCs. Thus, Direct numerical simulations are conducted for various bed erosion parameters and sediment settling velocities. This chapter also aims to formulate drag coefficient associated with cross-shelf motion of ACSTCs as a function of the Reynolds number, sediment concentration, sediment settling velocity, and the bed slope.

Chapter 5 aims to investigate the transition of alongshore current-supported turbidity currents to self-sustaining turbidity currents over erodible seabed composed of fine sediment, both analytically and numerically. Through erosion from the shelf floor, sediments can be slowly carried towards the shelf break with the aid of along-shelf current-supported turbidity currents; however, whether this slow-motion transitions to a massive transport by turbidity currents is not well known. Chapter 5 explores this possibility through the mathematical representation of the slow motion of the eroded sediments carried by along-shelf currents. In this chapter, the amount of fine sediment suspension as a function of sediment settling velocity and erosion parameters is analyzed. Based on these analyses, a simplified depth-integrated dynamic equation is developed for suspended sediment concentration. The inception of aforementioned transition is studied by

analyzing the stability of the developed equation both in itself and through temporal linear stability analysis.

1.4. SIGNIFICANCE TO PRACTICAL IMPLICATIONS

Sediment mass exchange between the continental shelf and the deep ocean is central to the understanding of the global cycles of geochemically important particulate matter. Turbidity currents are one of the agents that rapidly emplace massive sediment from the continental shelf to the deep ocean. Through erosion from the shelf floor, sediments can be slowly carried towards the shelf break with the aid of waves and alongshore currents known as wave- and current-supported turbidity currents; however, whether this slow-motion transitions to a massive transport by turbidity currents are not well known. This dissertation explores this possibility through the mathematical representation of the slow motion of the eroded sediments carried by along-shelf currents. The dependence of this possible transition on the shelf slope, erosion rate, and the size of sediments is studied in detail in this study. In addition, the representational of ACSTCs in large scale models requires efficient and accurate methods to evaluate the governing parameters. In this study, evaluation of these parameters is performed through basic fluid mechanisms perspectives. Methods similar to those applied in pipe flows are developed. With these formulations, one can be able to obtain the drag coefficient and friction coefficient for ACSTCs used in large scale models.

1.5. THE SCOPE OF THE STUDY

To achieve the goals and objectives of this study, we organize this thesis into six chapters. Chapter 1 presents a literature review on the current state of knowledge of WCSTCs. This chapter also introduces the motivations behind this work and the overall goals and objectives of the study. A detailed description of the numerical methodology used in the model is presented in chapter 2. Chapter 3 is intended to study the detailed turbulent characteristics of ACSTCs over an erodible

bed and focuses on the effect of various sediment settling velocities on suspended sediment concentration and offshore sediment transport. Chapter 4 investigates the velocity structure of a miniature along-shelf current supported turbidity current created via sediment suspension over erodible bed. This chapter focuses on attaining a relation for drag coefficient as a function of Reynolds number, sediment concentration, sediment settling velocity, and the bed slope. Chapter 5 studies the effect of bed erosion parameters and sediment settling velocity on total suspended sediment concentration due to ACSTCs. This chapter investigates the transition of alongshore current-supported turbidity currents to self-sustaining turbidity currents over erodible seabed composed of fine sediment, both analytically and numerically. Lastly, chapter 6 finalizes the thesis with discussions and future works.

2. NUMERICAL METHODOLOGY

2.1. GOVERNING EQUATIONS

To fully understand the fundamental characteristics of the wave- and current-supported turbidity currents (WCSTCs), a direct numerical simulation (DNS) study is employed on a fine sediment-laden channel flow over a smooth erodible bed with mild spanwise slope, *i.e.*, $\sin\theta < 0.012$ (Wright *et al*., 2001). The dynamics of turbidity currents, in general, are two-phase flow problems whereby sediment suspension and the carrier fluid, which is water in this study, are treated separately. Following previous studies on WCSTCs, we approximated the velocity of the sediment phase as the vectorial sum of the carrier fluid velocity and the representative sediment settling velocity as (Meiburg and Kneller, 2010; Ozdemir *et al*., 2010, 2011):

$$\boldsymbol{u}^s = \boldsymbol{u}^f + w_s \boldsymbol{e_g}, \tag{1}$$

where $\boldsymbol{u}^f = (u^f, v^f, w^f)$ is the local fluid velocity vector with u^f, v^f, and w^f being the fluid velocity components in the x-, y-, and z-directions, respectively. In Equation (1), $\boldsymbol{u}^s$ is the sediment phase velocity, w_s is the representative sediment settling velocity, and $\boldsymbol{e_g}$ is the unit vector in the direction of the gravitational acceleration.

The chosen sediments in this study are fine and their size ranges between 6 μm to 20 μm. Therefore, the dimensional settling velocity of spherical sediments with uniform diameter, d, can be calculated based on the Stokes Law as

$$w_s = \frac{(s-1)gd^2}{18\nu_f}, \tag{2}$$

here $s = \rho_s/\rho_f$ is the specific gravity of sediment with ρ_s and ρ_f being the sediment density and the density of water, respectively. In Equation (2), g is the magnitude of gravitational acceleration, and ν_f is the kinematic viscosity of water. The use of Stokes Law for calculating sediment settling

velocity is contingent on having a particle Reynolds number, Re_p, smaller than unity. The largest sediment size in our simulations is $d = 20\ \mu m$, and the corresponding sediment settling velocity is $w_s = 3.6 \times 10^{-4}\ m\ s^{-1}$ by using Equation (2). If one calculates the particle Reynolds number

$$Re_p = \frac{w_s d}{\nu_f} = \frac{(3.6 \times 10^{-4}\ \mathrm{m\ s^{-1}})(20 \times 10^{-6}\ m)}{1 \times 10^{-6}\ \mathrm{m^2 s^{-1}}} = 0.0072 \ll 1, \tag{3}$$

which confirms that the particle Reynolds number is far below unity. Thus, the use of Stokes Law is justified.

As will be discussed in detail in the next chapters, the dilute volumetric suspended sediment concentration assumption ($c < 1\%$) is adopted in this study where the sediment phase is considered as a continuum. For dilute sediment suspension, the fluid phase is approximated to satisfy the continuity equation. In addition, the Boussinesq approximation can be adopted in the momentum equation. Thus, the continuity and momentum equations of the fluid phase become

$$\boldsymbol{\nabla} \cdot \boldsymbol{u}^f = 0, \tag{4}$$

and

$$\frac{\partial \boldsymbol{u}^f}{\partial t} + \boldsymbol{u}^f \cdot \boldsymbol{\nabla} \boldsymbol{u}^f = -\frac{u_\tau^2}{h}\boldsymbol{e_x} - \frac{\boldsymbol{\nabla} p'}{\rho_f} + (s-1)gc\boldsymbol{e_g} + \nu_f \nabla^2 \boldsymbol{u}^f, \tag{5}$$

where p' is the dynamic pressure and u_τ is the friction velocity. In Equation (5), c is the volumetric sediment concentration. The first on the right-hand side of Equation (5) is the mean pressure gradient that drives the streamwise flow. The third term on the right-hand side of Equation (5) represents the buoyancy term that accounts for the coupling of the fluid and sediment phases. The sediment-induced stable density stratification is accounted through the vertical component of the buoyancy term, $-(s-1)g\ c \cos\theta\ \boldsymbol{e_z}$. The cross-shelf component of the buoyancy term also drives the turbidity current in the cross-shelf direction.

As mentioned previously, the chosen sediment size is sufficiently small, and the sediment phase is treated as a continuum. The governing equation for sediment phase is given as (Cantero *et al*., 2008):

$$\frac{\partial c}{\partial t} + \boldsymbol{u}^s \cdot \boldsymbol{\nabla} c = \mathfrak{D}\, \nabla^2 c, \tag{6}$$

where $\mathfrak{D}$ is the diffusivity of the sediment concentration.

In this study, the FineSed3D model (Cheng *et al*., 2015a, 2015b) is employed. The FineSed3D model uses a hybrid spectral-compact finite difference scheme to solve the governing equations. Pseudo-spectral methods are utilized in the periodic directions (x- and y-directions) whereby the variables are expanded as Fourier series. A sixth-order accurate compact finite difference scheme is used to evaluate the bed-normal gradients. A hybrid scheme is used for time integration where the diffusive terms are computed via a semi-implicit second-order Crank-Nicolson method. The non-linear terms are also evaluated by the Arakawa method (Arakawa and Lamb, 1981) and integrated by a third order Runge-Kutta method (Cortese and Balachandar, 1995; Cantero *et al.*, 2008). Aliasing errors are minimized by using the "3/2 rule" de-aliasing method (Canuto *et al.*, 1987; Peyret, 2002) and Arakawa method (Arakawa, 1966). The numerical methodology is addressed in detail in the following subsections.

2.2. DISCRETIZATION

While grid spacing is equidistant in the x- and y-directions, to have higher resolution near the top and bottom boundaries, Chebyshev-Gauss-Lobbato collocation points are used for discretization in the bed-normal direction as (Canuto *et al*., 1987):

$$z = \cos(\theta_k), \tag{7a}$$

$$\theta_k = (k-1)\Delta\theta, \tag{7b}$$

and

$$\Delta\theta = \frac{\pi}{N_z}, \tag{7c}$$

where $1 \leq k \leq N_z + 1$ with N_z being the number of grid points in the bed-normal direction. In this setup, collocation points are mostly clustered close to the top and bottom boundaries where gradients are large, and the turbulence level is high (Deusebio *et al*., 2014). The collocation points can be presented as:

$$\boldsymbol{x}(i,j,k) = \left(\frac{iL_x}{N_x}, \frac{jL_y}{N_y}, \cos\left(\frac{(k-1)\pi}{N_z - 1}\right)\right), \tag{8}$$

where $\boldsymbol{x}$ is the position vector. In Equation (8), L_x and L_y are the domain sizes in the x- and y-directions, respectively, and $1 \leq i \leq N_x$ and $1 \leq j \leq N_y$ with N_x and N_y being the number of grid points in the x- and y-directions, respectively.

2.3. BOUNDARY CONDITIONS

Periodic boundary conditions are defined along the streamwise and spanwise directions for both fluid and sediment phases. Periodic boundary conditions are not suitable for classical turbidity currents of highly transient characteristics. However, considering the low velocity of WCSTCs ($\sim$0.1 m s^{-1}), an equilibrium can quickly be established for these types of turbidity currents (Wright *et al*., 2001; Scully *et al*., 2002; Friedrichs and Wright, 2006; Flores *et al*., 2018). Indeed, the equilibrium assumption is tested, and its presence is verified in the field by Flores *et al*. (2018). Therefore, due to the spatial and temporal homogeneity of WCSTCs, imposing periodic boundary conditions is justifiable.

For the velocity field, a no-slip and no-penetration wall boundary is specified at the bottom of the domain, *i.e.*, $\boldsymbol{u}^f = 0$, whereas free-slip and no-penetration boundary (rigid lid) is imposed at the top boundary, *i.e.*, $\frac{\partial u^f}{\partial z} = \frac{\partial v^f}{\partial z} = 0$ and $w^f = 0$. At the bed, erosional/depositional boundary condition is specified to allow sediment erosion (deposition) from (to) the bed:

$$-\mathfrak{D}\frac{\partial c}{\partial z}\Big|_{z=0} = E - D, \tag{9}$$

where E and D are the erosion and deposition fluxes, respectively. The Partheniades-Ariathurai-type formulation is used to calculate the erosion flux as (Sanford and Maa, 2001):

$$E = \begin{cases} m_e(1-\phi)\left(\dfrac{|\boldsymbol{\tau}_b|}{\tau_c} - 1\right) & |\boldsymbol{\tau}_b| \geq \tau_c \\ 0 & |\boldsymbol{\tau}_b| < \tau_c \end{cases}, \tag{10}$$

where m_e is the erosion coefficient, ϕ is the porosity, $|\boldsymbol{\tau}_b|$ is the magnitude of the bed shear stress, and τ_c is the critical shear stress of erosion. The bed shear stress is calculated at each time step as:

$$|\boldsymbol{\tau}_b| = \mu_f \left|\frac{\partial \boldsymbol{u}^f}{\partial z}\right|_{z=0}, \tag{11}$$

where μ_f is the dynamic viscosity of the seawater. The deposition flux is also calculated as (Sanford and Maa, 2001; Winterwerp, 2007):

$$D = w_s c\Big|_{z=0}. \tag{12}$$

2.4. EVALUATION OF FIRST- AND SECOND-ORDER PARTIAL DERIVATIVES

2.4.1. PERIODIC DIRECTION

Periodic boundary conditions are imposed along the x- and y-directions, and Fourier series are selected as base functions in these directions. Fast Fourier transform (FFT) algorithms are used to ease the computational cost. The velocity field can be written as:

$$\boldsymbol{u}(x,y,z,t) = \sum_{k_x=-\frac{N_x}{2}}^{\frac{N_x}{2}-1} \sum_{k_y=-\frac{N_y}{2}}^{\frac{N_y}{2}-1} \sum_{k=0}^{N_z} \widehat{\widehat{\boldsymbol{u}}}\left(k_x, k_y, z, t\right) e^{\mathrm{i}k_x x} e^{\mathrm{i}k_y y}, \tag{13}$$

where the double cap ($\widehat{\widehat{\ }}$) shows that the variable is evaluated in the spectral space in both x- and y-directions, and i stands for the imaginary unit.

The first-order derivatives are evaluated by the multiplication of the quantity of interest with $\mathrm{i}k_x$ and $\mathrm{i}k_y$. The second-order derivatives are also scaled by $-k_x^2$ and $-k_y^2$, which is summarized for the streamwise velocity as:

$$\frac{\partial \widehat{\boldsymbol{u}}}{\partial x} = \mathrm{i}k_x\left(\widehat{\boldsymbol{u}}\right), \tag{14a}$$

$$\frac{\partial \widehat{\boldsymbol{u}}}{\partial y} = \mathrm{i}k_y\left(\widehat{\boldsymbol{u}}\right), \tag{14b}$$

$$\frac{\partial^2 \widehat{\boldsymbol{u}}}{\partial x^2} = -k_x^2\left(\widehat{\boldsymbol{u}}\right), \tag{14c}$$

and

$$\frac{\partial^2 \widehat{\boldsymbol{u}}}{\partial y^2} = -k_y^2\left(\widehat{\boldsymbol{u}}\right). \tag{14d}$$

Thus, the momentum equation in the Fourier space can be written as

$$\frac{\partial \widehat{\boldsymbol{u}}^f}{\partial t} + \mathcal{F}(\boldsymbol{u}^f \cdot \boldsymbol{\nabla}\boldsymbol{u}^f) = -\frac{u_\tau^2}{h}\boldsymbol{e_x} - \frac{\mathcal{F}(\boldsymbol{\nabla}p')}{\rho_f} + (s-1)g\hat{c}\boldsymbol{e_g} + \nu_f\left(-\left(k_x^2 + k_y^2\right) + \frac{\partial^2}{\partial z^2}\right)\widehat{\boldsymbol{u}}^f, \tag{15}$$

where $\mathcal{F}(\quad)$ is the discrete Fourier transform operator. The advection-diffusion equation for the concentration in the Fourier space can also be written as

$$\frac{\partial \hat{\hat{c}}}{\partial t} + \mathcal{F}(\boldsymbol{u}^s \cdot \boldsymbol{\nabla}c) = \mathfrak{D}\left(-\left(k_x^2 + k_y^2\right) + \frac{\partial^2}{\partial z^2}\right)\hat{\hat{c}}. \tag{16}$$

The advection and diffusion operators are simplified as

$$A\left(\widehat{\boldsymbol{u}}^f\right) = -\mathcal{F}(\boldsymbol{u}^f \cdot \boldsymbol{\nabla}\boldsymbol{u}^f), \tag{17a}$$

and

$$D\left(\widehat{\boldsymbol{u}}^f\right) = \nu_f\nabla^2\widehat{\boldsymbol{u}}^f = \nu_f\left(-\left(k_x^2 + k_y^2\right) + \frac{\partial^2}{\partial z^2}\right)\widehat{\boldsymbol{u}}^f. \tag{17b}$$

2.4.2. WALL-NORMAL DIRECTION

A sixth-order compact finite difference scheme is employed on Chebyshev-Gauss-Lobatto collocation points in the wall-normal direction. The general form of the compact finite difference scheme centered at x_i is defined as

$$\frac{\partial^p u_i}{\partial z^p} + \sum_{j \in I_n} a_j \frac{\partial^p u_j}{\partial z^p} = b_i u_i + \sum_{j \in I_{m \neq i}} b_j u_j + \sum_{j \in I_n} c_j u_j. \tag{18}$$

Note that the order of the scheme can be determined as $2n + m - 1$, where m and n represent the point set of I_m and I_n, respectively. For a 6[th] order compact finite difference I_m and I_n are specified as $I_m = \{i-2, i, i+2\}$ and $I_n = \{i-1, i+1\}$. For the interior grid, the centered schemed is implemented as

$$a_{i-1} \frac{\partial^p u_{i-1}}{\partial z^p} + \frac{\partial^p u_i}{\partial z^p} + a_{i+1} \frac{\partial^p u_{i+1}}{\partial z^p} = b_{i-2} u_{i-2} + c_{i-1} u_{i-1} + b_i u_i + c_{i+1} u_{i+1} + b_{i+2} u_{i+2}, \tag{19}$$

while a one-sided scheme is implemented at the top and bottom boundaries. For the bottom boundary

$$a_1 \frac{\partial^p u_1}{\partial z^p} + u_2^{(p)} + a_3 \frac{\partial^p u_3}{\partial z^p} = c_1 u_1 + b_2 u_2 + c_3 u_3 + b_4 u_4 + c_5 u_5, \tag{20a}$$

$$\frac{\partial^p u_1}{\partial z^p} + a_2 \frac{\partial^p u_2}{\partial z^p} = b_1 u_1 + c_2 u_2 + b_3 u_3 + c_4 u_4 + b_5 u_5 + c_6 u_6, \tag{20b}$$

and for the top boundary

$$a_{N-2} \frac{\partial^p u_{N-2}}{\partial z^p} + \frac{\partial^p u_{N-1}}{\partial z^p} + a_N \frac{\partial^p u_N}{\partial z^p} = c_{N-4} u_{N-4} + b_{N-3} u_{N-3} + c_{N-2} u_{N-2} + b_{N-1} u_{N-1} + c_N u_N, \tag{20c}$$

$$\frac{\partial^p u_N}{\partial z^p} + a_{N-1} \frac{\partial^p u_{N-1}}{\partial z^p} = c_{N-5} u_{N-5} + b_{N-4} u_{N-4} + c_{N-3} u_{N-3} + b_{N-2} u_{N-2} + c_{N-1} u_{N-1} + b_N u_N, \tag{20d}$$

where a, b, and c coefficients can be derived based on Lagrangian polynomials (Shukla and Zhong, 2005). For a given set of distinct points $x_i \in I_k$ and numbers u_i, the Lagrange polynomial is the polynomial with the least degree such that $u(x_i) = u_i$. The interpolation polynomial is a linear combination of the Lagrange basis polynomials on the given set I_k:

$$u(x) = \sum_{j \epsilon I_k} u_j l_j^k(x), \tag{21}$$

with the Lagrange basis polynomial on I_k specified as

$$l_i^k(x) = \frac{\Pi_{j \epsilon \mathrm{I}_k \neq i}(x - x_j)}{\Pi_{j \epsilon \mathrm{I}_k \neq i}(x_i - x_j)}, \tag{22}$$

where Π is the operator of the product of a sequence. The general compact scheme for first- and second-order partial derivatives is given in the following.

2.4.2.1. SCHEME FOR THE FIRST-ORDER DERIVATIVE

The general compact scheme for the first-order derivative centered at x_i is as follows:

$$\frac{\partial u_i}{\partial z} + \sum_{j \in I_n} a_j \frac{\partial u_j}{\partial z} = b_i u_i + \sum_{j \in I_{m \neq i}} b_j u_j + \sum_{j \in I_n} c_j u_j. \tag{23}$$

For the points sets given as $I_m = \{i - 2, i, i + 2\}$ and $I_n = \{i - 1, i + 1\}$ the first-order derivative for the interior domain become:

$$a_{i-1} \frac{\partial u_i - 1}{\partial z} + \frac{\partial u_i}{\partial z} + a_{i+1} \frac{\partial u_{i+1}}{\partial z} = b_{i-2} u_{i-2} + c_{i-1} u_{i-1} + b_i u_i + c_{i+1} u_{i+1} + b_{i+2} u_{i+2}. \tag{24}$$

The coefficients of Equation (24) can be found in appendix A1.

2.4.2.2. SCHEME FOR THE SECOND-ORDER DERIVATIVE

The general form of the second-order derivative can be written as:

$$\frac{\partial^2 u_i}{\partial z^2} + \sum_{j \in I_n} a_j \frac{\partial^2 u_j}{\partial z^2} = b_i u_i + \sum_{j \in I_{m \neq i}} b_j u_j + \sum_{j \in I_n} c_j \, u_j. \tag{25}$$

For the points sets given as $I_m = \{i-2, i, i+2\}$ and $I_n = \{i-1, i+1\}$ the second-order derivative for the interior domain become:

$$a_{i-1}\frac{\partial^2 u_{i-1}}{\partial z^2} + \frac{\partial^2 u_i}{\partial z^2} + a_{i+1}\frac{\partial^2 u_{i+1}}{\partial z^2} = b_{i-2}u_{i-2} + c_{i-1}u_{i-1} + b_i u_i + c_{i+1}u_{i+1} + b_{i+2}u_{i+2}. \quad (26)$$

The coefficients of Equation (26) can be found in appendix A2.

2.4.2.3. MATRIX FORMULATION

The first- and second-order derivatives in the matrix form are defined as

$$\boldsymbol{A_1}\frac{\partial u_i}{\partial z} = \boldsymbol{B_1}u_i, \quad (27a)$$

$$\boldsymbol{A_2}\frac{\partial^2 u_i}{\partial z^2} = \boldsymbol{B_2}u_i. \quad (27b)$$

Thus, the first- and second-order derivatives can be written as:

$$\frac{\partial u_i}{\partial z} = \boldsymbol{A_1^{-1}B_1}u_i, \quad (28a)$$

$$\frac{\partial^2 u_i}{\partial z^2} = \boldsymbol{A_2^{-1}B_2}u_i. \quad (28b)$$

2.5. NON-LINEAR TERMS

2.5.1. ALIASING ERRORS

While transferring from real space to Fourier space, aliasing errors are generated by non-linear differential operators. Aliasing errors can be described as the cascade of energy beyond the highest wavenumber that is bounded by the number of collocation points (N). The problem associated with aliasing errors is fixed by using the Arakawa and "3/2" rule de-aliasing methods. The details of these methods are discussed in the following.

2.5.2. "3/2" RULE DE-ALIASING METHOD

The "3/2" rule de-aliasing method is used to solve the aliasing problem along the periodic directions. In this method, the frequency domain of size N is extended to size $3N/2$ in Fourier

space while higher frequencies are set to be zero. The variables with the extended size of $3N/2$ are transferred into real space to calculate the non-linear terms. The calculated non-linear terms are back transferred to the Fourier space, interpolated, and sized back to size N. Therefore, the data leakage to higher wavenumbers is minimized (Canuto *et al*., 2011; Peyret, 2002).

2.5.3. ARAKAWA METHOD

The Arakawa method is a modified second-order finite difference formula used for non-linear advection terms. This method exactly conserves the discretized energy for general flow and prevents the non-linear instability from occurring. In this study, the convective form of the non-linear terms is used at odd time-steps, while the divergence form of non-linear terms is adopted at even time-steps. For odd time steps:

$$u\frac{\partial u}{\partial x}+v\frac{\partial u}{\partial y}+w\frac{\partial u}{\partial z}\rightarrow u, \tag{29a}$$

$$u\frac{\partial v}{\partial x}+v\frac{\partial v}{\partial y}+w\frac{\partial v}{\partial z}\rightarrow v, \tag{29b}$$

and

$$u\frac{\partial w}{\partial x}+v\frac{\partial w}{\partial y}+w\frac{\partial w}{\partial z}\rightarrow w. \tag{29c}$$

For even time steps:

$$\frac{\partial(uu)}{\partial x}+\frac{\partial(uv)}{\partial y}+\frac{\partial(uw)}{\partial z}\rightarrow u, \tag{30a}$$

$$\frac{\partial(vu)}{\partial x}+\frac{\partial(vv)}{\partial y}+\frac{\partial(vw)}{\partial z}\rightarrow v, \tag{30b}$$

and

$$\frac{\partial(wu)}{\partial x}+\frac{\partial(wv)}{\partial y}+\frac{\partial(ww)}{\partial z}\rightarrow w. \tag{30c}$$

2.6. TIME INTEGRATION

The standard projection method is used to solve Equation (14) and (15) (Chorin, 1968) where a hybrid scheme is used for the time integration. In this method, the diffusive terms are calculated through a semi-implicit second-order Crank-Nicolson method, and a third-order accurate Runge-Kutta method is used to calculate the non-linear advection terms (Williamson, 1980; Cortese and Balachandar, 1995; Cantero *et al.*, 2008). The details of the Runge-Kutta and Crank-Nicolson time advancing methods are presented in the following subsections.

2.6.1. RUNGE-KUTTA METHOD

The non-linear advection terms are integrated by a third-order accurate Runge-Kutta method (RK3). The Runge-Kutta formulation used in the present work is as follows (Canuto *et al*., 1987)

$$u^{n+1} = u^n + \frac{1}{9}\Delta t[2k_1 + 3k_2 + 4k_3], \tag{31a}$$

where

$$k_1 = f(u^n, t_n), \tag{31b}$$

$$k_2 = f\left(u^n + \tfrac{1}{2}\Delta t k_1, t_n + \tfrac{1}{2}\Delta t\right), \tag{31c}$$

and

$$k_3 = f\left(u^n + \tfrac{3}{4}\Delta t k_2, t_n + \tfrac{3}{4}\Delta t\right). \tag{31d}$$

Here k_i denotes the three steps of the Runge-Kutta method where $i = 1, 2, 3$.

2.6.2. CRANK-NICOLSON METHOD

The diffusive terms are evaluated with the semi-implicit second-order Crank-Nicolson method. The Crank-Nicolson method used is a combination of the forward Euler method at time step n and backward Euler method at time step $n + 1$:

$$\frac{u_i^{n+1} - u_i^n}{\Delta t} = \frac{1}{2}\left[F_i^{n+1}\left(u, x, t, \frac{\partial u}{\partial x}, \frac{\partial^2 u}{\partial x^2}\right) + F_i^n\left(u, x, t, \frac{\partial u}{\partial x}, \frac{\partial^2 u}{\partial x^2}\right)\right]. \tag{32}$$

2.6.3. NUMERICAL IMPLEMENTATION

The velocity is solved in four steps. At the first step, *i.e.*, the prediction step, the velocity is first calculated at the intermediate level ($\widehat{\widehat{\boldsymbol{u}}}^{(m*)}$). The intermediate velocity is evaluated using advective, $\widehat{\widehat{\boldsymbol{H}}}^{(m)}$, and diffusive terms, $D\left(\widehat{\widehat{\boldsymbol{u}}}^{(m*)}\right)$ and $D\left(\widehat{\widehat{\boldsymbol{u}}}^{(m-1)}\right)$ through the solution of the Helmholtz equation as

$$\widehat{\widehat{\boldsymbol{u}}}^{(0)} = \widehat{\widehat{\boldsymbol{u}}}\left(t^{(n)}\right), \tag{33}$$

$$\widehat{\widehat{\boldsymbol{H}}}^{(m)} = \Delta t\left[A\left(\widehat{\widehat{\boldsymbol{u}}}^{(m-1)}\right) + (s-1)g\hat{\hat{c}}\boldsymbol{e_g} + \mathcal{F}(\nu_f \nabla^2 \boldsymbol{u}^{(m-1)})\right] + \lambda_1(m)\widehat{\widehat{\boldsymbol{H}}}^{(m-1)}, \tag{34}$$

$$\widehat{\widehat{\boldsymbol{u}}}^{(m*)} = \widehat{\widehat{\boldsymbol{u}}}^{(m-1)} + \lambda_2(m)\widehat{\widehat{H}}^{(m)} + \Gamma(m)\left[D\left(\widehat{\widehat{\boldsymbol{u}}}^{(m-1)}\right) + D\left(\widehat{\widehat{\boldsymbol{u}}}^{(m*)}\right)\right]. \tag{35}$$

The star superscript $(*)$ discerns the intermediate step. In the correction step (Steps 2 and 3), the Poisson equation is solved to calculate the pressure in the spectral space as

$$\nabla^2 \hat{\hat{p}}^{(m)} = \frac{1}{2\Gamma(m)} \boldsymbol{\nabla} \cdot \widehat{\widehat{\boldsymbol{u}}}^{(m*)}. \tag{36}$$

The calculated pressure gradient and intermediate velocity are used to evaluate the velocity in a divergence-free field as

$$\widehat{\widehat{\boldsymbol{u}}}^{(m)} = \widehat{\widehat{\boldsymbol{u}}}^{(m*)} - 2\Gamma(m)\boldsymbol{\nabla}\hat{\hat{p}}^{(m)}\,. \tag{37}$$

As a part of the third-order accurate Runge-Kutta method these steps are repeated three times to complete one full time step:

$$\widehat{\widehat{\boldsymbol{u}}}\left(t^{(n+1)}\right) = \widehat{\widehat{\boldsymbol{u}}}^{(3)}. \tag{38}$$

The governing equation for sediment concentration is concurrently evaluated through the solution of the Helmholtz equation in the following steps:

$$\widehat{\widehat{\boldsymbol{H}}}^{(m)} = \Delta t\left[A\left(\hat{\hat{c}}^{(m-1)}\right)\right] + \lambda_1(m)\widehat{\widehat{\boldsymbol{H}}}^{(m-1)}, \tag{39}$$

$$\hat{\hat{c}}^{(m*)} = \hat{\hat{c}}^{(m-1)} + \lambda_2(m)\widehat{\widehat{H}}^{(m)} + \Gamma(m)\left[D\left(\hat{\hat{c}}^{(m-1)}\right) + D\left(\hat{\hat{c}}^{(m*)}\right)\right], \tag{40}$$

$$\hat{\hat{c}}\left(t^{(n+1)}\right) = \hat{\hat{c}}^{(3)}. \tag{41}$$

It is essential to solve Equation (40) before Equation (34) to use the calculated $\hat{\hat{c}}$ value for the evaluation of $\widehat{\widehat{H}}^{(m)}$. In all above equations, $m = 1, 2, 3$, and the coefficients of the non-linear terms at the first- and second-steps are $\lambda_1 = \left\{0, -\frac{5}{9}, -\frac{153}{128}\right\}$ and $\lambda_2 = \{\frac{1}{3}, \frac{15}{16}, \frac{8}{15}\}$, respectively. The coefficients of the diffusive terms are also defined as $\Gamma = \{\frac{\Delta t}{6}, \frac{5\Delta t}{24}, \frac{\Delta t}{8}\}$ with Δt being the time-step that is chosen based on Courant–Friedrichs–Lewy (CFL) criteria.

To force the no-slip boundary condition at the bottom wall, pressure gradients is set to be zero by specifying the Neumann boundary condition at the wall. Defining τ to be the unit vector tangential to the wall, the tangential component of the pressure at the correction step is:

$$\tau . \widehat{\widehat{\boldsymbol{u}}}^{(m)} \Big|_{z=0} = \tau \cdot \left[\widehat{\widehat{\boldsymbol{u}}}^{(m_*)} - 2\Gamma(m)\boldsymbol{\nabla}\hat{\hat{p}}^{(m)}\right]\Big|_{z=0}. \tag{42}$$

The no-slip condition requires the left-hand side of the above equation to be zero. This can be used to obtain the boundary condition for the intermediate velocity as:

$$\widehat{\widehat{\boldsymbol{u}}}^{(m_*)} \Big|_{z=0} = 2\Gamma(m)\boldsymbol{\nabla}\hat{\hat{p}}^{(m)} \Big|_{z=0}. \tag{43}$$

Since the pressure $\hat{\hat{p}}^{(m)}$ has not yet been computed when the intermediate velocity $\hat{\hat{u}}^{(m_*)}$ is calculated, an approximation of $\boldsymbol{\nabla}\hat{\hat{p}}^{(m)}$ must be used instead. A second-order accurate approximation using Taylor series expansion is used in this study, which gives:

$$\boldsymbol{\nabla}\hat{\hat{p}}^{(m)} = \boldsymbol{\nabla}\hat{\hat{p}}^{(m-1)}\left[1 + \frac{\Gamma(m)}{\Gamma(m-1)}\right] - \boldsymbol{\nabla}\hat{\hat{p}}^{(m-2)}\left[\frac{\Gamma(m)}{\Gamma(m-1)}\right] + O(\Delta t^2). \tag{44}$$

Hence, the corresponding boundary conditions for the intermediate velocity components become:

$$\hat{\hat{u}}^{(m_*)} \Big|_{z=0} = 2\Gamma(m)\left\{\frac{\partial \hat{\hat{p}}^{(m-1)}}{\partial x}\left[1 + \frac{\Gamma(m)}{\Gamma(m-1)}\right] - \frac{\partial \hat{\hat{p}}^{(m-2)}}{\partial x}\left[\frac{\Gamma(m)}{\Gamma(m-1)}\right]\right\}\Big|_{z=0}, \tag{45}$$

$$\hat{\hat{v}}^{(m_*)} \Big|_{z=0} = 2\Gamma(m)\left\{\frac{\partial \hat{\hat{p}}^{(m-1)}}{\partial y}\left[1 + \frac{\Gamma(m)}{\Gamma(m-1)}\right] - \frac{\partial \hat{\hat{p}}^{(m-2)}}{\partial y}\left[\frac{\Gamma(m)}{\Gamma(m-1)}\right]\right\}\Big|_{z=0}. \tag{46}$$

Moreover, the pure Neumann boundary condition for the pressure field is:

$$\frac{\partial \hat{\hat{p}}^{(m)}}{\partial z}\Big|_{z=0} = 0, \tag{47}$$

which gives the boundary condition for the vertical component of the intermediate velocity:

$$\hat{\hat{w}}^{(m_*)}\Big|_{z=0} = 0. \tag{48}$$

2.7. SOLUTION OF THE GENERAL METHODOLOGY

The solution procedure of the Helmholtz and Poisson equations are discussed in the following subsections.

2.7.1. SOLUTION OF THE HELMHOLTZ EQUATION

The solution of the Helmholtz equation used for the evaluation of the velocity field in the prediction step is presented in this section. By specifying the diffusion operator, *i.e.*, Equation (17b), as $D(\quad) = \mathbf{D}\boldsymbol{A_2^{-1}}\boldsymbol{B_2} - \left(k_x^2 + k_y^2\right)\mathbf{D}$, Equation (34) can be written as

$$\frac{\hat{\hat{\boldsymbol{u}}}^{(m_*)}}{\Gamma(m)} - D\left(\hat{\hat{\boldsymbol{u}}}^{(m_*)}\right) = \hat{\hat{\boldsymbol{b}}}, \tag{49}$$

where $\hat{\hat{\boldsymbol{b}}} = \frac{\left[\hat{\hat{\boldsymbol{u}}}^{(m-1)} + \lambda_2(m)\hat{\hat{\boldsymbol{H}}}^{(m)}\right]}{\Gamma(m)} - D\left(\hat{\hat{\boldsymbol{u}}}^{(m-1)}\right)$. Equation (49) can be re-written as

$$\mathbf{D}\boldsymbol{A_2^{-1}}\left[\boldsymbol{B_2} - \left(k_x^2 + k_y^2\right)\boldsymbol{A_2} - \frac{1}{\Gamma(m)}\boldsymbol{A_2}\mathbf{D}^{-1}\right]\hat{\hat{\boldsymbol{u}}}^{(m_*)} = \hat{\hat{\boldsymbol{b}}}. \tag{50}$$

By specifying $\hat{\hat{\boldsymbol{b}}}' = \boldsymbol{A_2}\mathbf{D}^{\mathbf{-1}}\hat{\hat{\boldsymbol{b}}}$, and $\boldsymbol{C} = \boldsymbol{B_2} - \left(k_x^2 + k_y^2\right)\boldsymbol{A_2} - \frac{1}{\Gamma(m)}\boldsymbol{A_2}\mathbf{D}^{-1}$, Equation (50) becomes

$$\boldsymbol{C}\hat{\hat{\boldsymbol{u}}}^{(m_*)} = \hat{\hat{\boldsymbol{b}}}'. \tag{51}$$

Equation (51) is solved using lower-upper (LU) decomposition method.

2.7.2. SOLUTION OF THE POISSON EQUATION

The pressure Poisson equation form Equation (36) can be written as

$$\nabla^2\hat{\hat{p}} = \frac{1}{2\Gamma(m)}\left(\hat{\hat{u}}_x + \hat{\hat{u}}_y + \boldsymbol{A_1^{-1}}\boldsymbol{B_1}\hat{\hat{w}}\right), \tag{52}$$

where $\hat{\hat{u}}_x = -\mathrm{i}k_x\hat{\hat{u}}$ and $\hat{\hat{u}}_y = -\mathrm{i}k_y\hat{\hat{v}}$. According to Boersma (2011) the second-order derivative discretization is not compatible with the first-order derivative discretization for compact finite difference scheme (See Equation (27a) and (27b)), which means:

$$\boldsymbol{A_2^{-1}B_2\hat{\hat{u}} \neq A_1^{-1}B_1\left(A_1^{-1}B_1\hat{\hat{u}}\right)}. \tag{53}$$

Thus, it will introduce large numerical errors if we direct use the second-order derivative scheme to solve the pressure Poisson equation and correct the velocity field using the first-order derivative scheme. Thus, the right discretization for the pressure Poisson equation becomes (Boersma, 2011):

$$-\left(k_x^2 + k_y^2\right)\hat{\hat{p}} + \boldsymbol{A_1^{-1}B_1}\left(\boldsymbol{A_1^{-1}B_1}\hat{\hat{p}}\right) = \frac{1}{2\Gamma(m)}\left(\hat{\hat{u}}_x + \hat{\hat{u}}_y + \boldsymbol{A_1^{-1}B_1}\hat{\hat{w}}\right). \tag{54}$$

By defining $\boldsymbol{F} = (\boldsymbol{A_1^{-1}B_1})^2$ and taking the Eigen-decomposition, we obtain:

$$\boldsymbol{F = R\Lambda R^{-1}}, \tag{55}$$

where $\boldsymbol{\Lambda}$ is a diagonal matrix with the Eigen values of matrix $\boldsymbol{F}$ as its elements. Equation (55) can be re-written as:

$$\boldsymbol{R}\left(\boldsymbol{\Lambda} - \left(k_x^2 + k_y^2\right)\boldsymbol{I}\right)\boldsymbol{R^{-1}}\hat{\hat{p}} = \frac{1}{2\Gamma(m)}\left(\hat{\hat{u}}_x + \hat{\hat{u}}_y + \boldsymbol{A_1^{-1}B_1}\hat{\hat{w}}\right), \tag{56}$$

and can be solved with given $\boldsymbol{R}$, $\boldsymbol{\Lambda}$, and $\boldsymbol{R^{-1}}$.

3. ROLE OF SEDIMENT SETTLING VELOCITY ON ALONG-SHELF CURRENT-SUPPORTED TURBIDITY CURRENTS OVER ERODIBLE BED

3.1. INTRODUCTION

3.1.1. BACKGROUND AND MOTIVATION

Sea level rise and global change in extreme weather patterns change the nearshore ocean dynamics and alter the intensity of exchange mechanisms of sediments that contain carbon, nitrogen, and other geochemically important matter from nearshore to the deep ocean. Such a change makes the global assessment of these geochemical species more challenging. Therefore, accurate quantification of the physical processes that route sediments from nearshore to the continental margin provides vital information to the global assessment of these chemical species and the life in the ocean. One of the processes that route sediments from inner to outer shelves are wave- and current-supported turbidity currents (WCSTCs). These are a subclass of turbidity currents and take place within a thin layer close to the seafloor. As such, WCSTCs cannot be resolved in operational ocean models (Harris *et al*., 2003; 2005) and need to be integrated into operational models through accurate modeling with appropriate parameterization. Such an endeavor cannot proceed without a fundamental understanding of the governing processes of WCSTCs. With the motivation to understand these processes at the fundamental level, this chapter aims at understanding the dynamics of this special class of turbidity currents when driven by only along-shelf currents over erodible seafloor.

WCSTCs are slow-moving turbidity currents that occur along the mild-sloped portions of the continental shelves. They are recognized to be one of the significant agents to emplace sediments in the continental shelves worldwide (Sternberg *et al*., 1988; Wright *et al*., 1990, 2001; Ogston *et al*., 2000; Geyer *et al*., 2000; Traykovski *et al*., 2007). Unlike classical turbidity currents, where

turbulence is generated by the forward motion of the turbidity currents (Parker *et al*., 1986; Cantero *et al*., 2008; Meiburg and Kneller, 2010; Francisco *et al*., 2018; Hermidas *et al*., 2018), WCSTCs are aided by the near-bed (or boundary-layer) turbulence in association with waves and/or currents. Wave- and current-induced near-bed turbulence keeps the sediments suspended, and the mild cross-shelf slope drives the cross-shelf turbidity current. In the absence of current- and wave-induced near-bed turbulence, sediment suspension will cease and hence WCSTCs will annihilate. This characteristic of WCSTCs differentiates them from the classical turbidity currents.

A subclass of WCSTCs is the along-shelf current-supported turbidity currents (ACSTCs) where sediment suspension is created and sustained by the along-shelf currents, and the downslope gravity force moves the turbidity current (See Fig. 1). ACSTCs are particularly important in regions where tidal currents are the dominant hydrodynamic drivers such as that in the Gulf of Bohai. Indeed, ACSTCs were first documented at the Gulf Bohai in close proximity to the mouth of the Yellow River in northeast China (Wright *et al*., 1988). The same study also reports that the waves were absent and the tidal currents, ranging from $0.12\ \mathrm{m\ s^{-1}}$ to $0.40\ \mathrm{m\ s^{-1}}$, were the only drivers of sediment suspension. It was also reported that over $5\ \mathrm{m/km}$ shelf-slope ACSTCs may reach up to $0.40\ \mathrm{m\ s^{-1}}$.

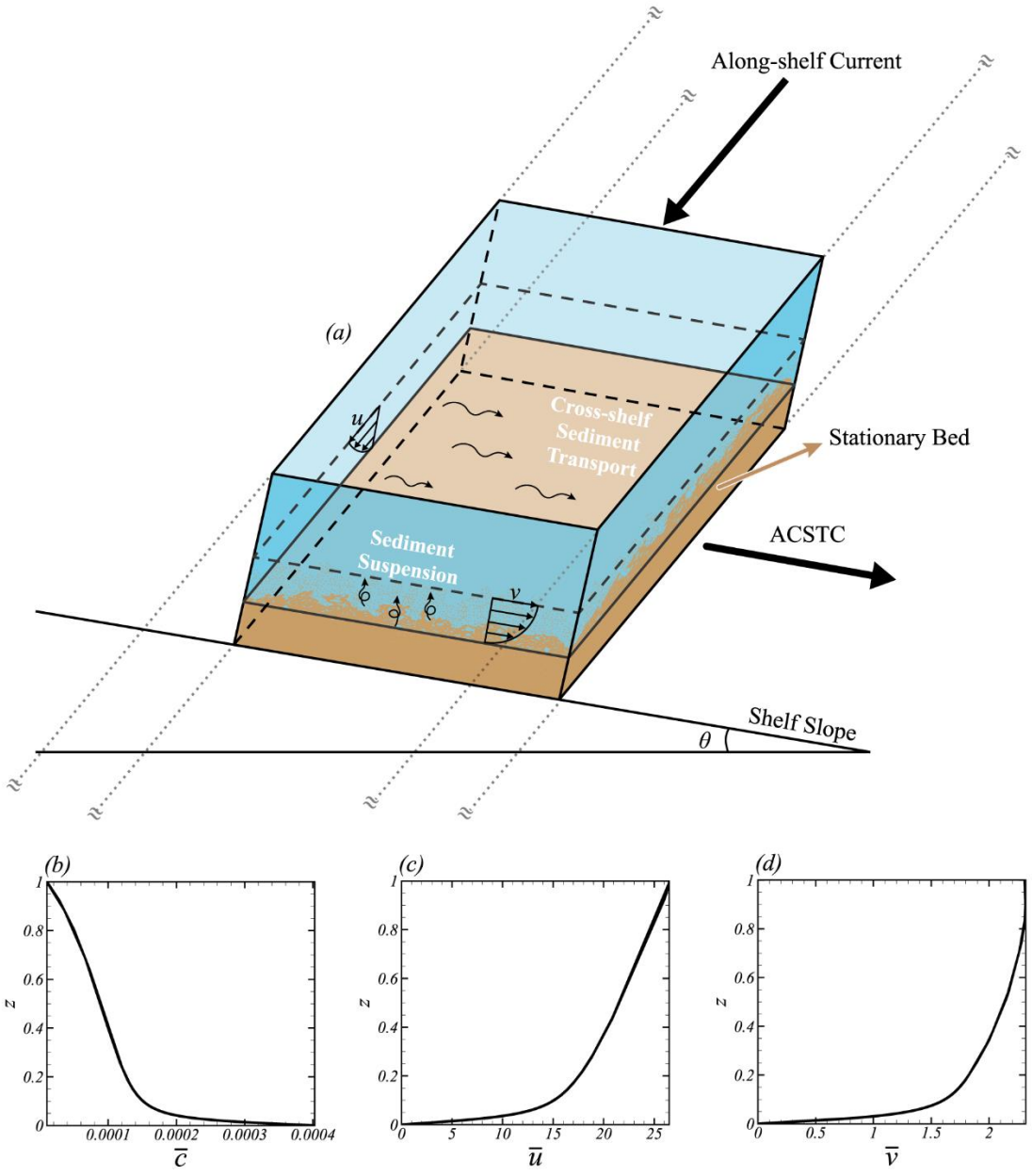

Figure 3.1. (a) Descriptive sketch of the problem (not to scale). The shear stress associated with the along-shelf current erodes sediment from the stationary bed and suspends them into the water column. At the same time, sediment suspension creates a cross-shelf (down-slope) gravity force and initiates a flow in the direction of the shelf-slope. The flow generated in the cross-shelf direction is a close approximation of ACSTCs. Representative (b) concentration, $\bar{c}$, (c) streamwise velocity, $\bar{u}$, and (d) spanwise velocity, $\bar{v}$, profiles.

Sediment source for WCSTCs were initially thought to be associated with rapid river-borne sediment delivery to the shelves and/or sediment flux divergence due to estuarine-like shelf processes (Stenberg *et al*., 1988; Geyer *et al*., 2000). However, sediment reworking and erosion in

ephemeral fine sediment deposits were also recognized as triggering mechanisms that initiate WCSTCs, which was observed from the sediment deposits in Po Prodelta (Traykovski *et al*., 2007) and Eel River (Geyer *et al*., 2000). Yet, erosion and deposition in these turbidity currents were hypothesized to be dictated by sediment-induced density stratification (for details see Wright *et al*., 2001). To the best of our knowledge, this hypothesis has not been rigorously tested. Therefore, the current state of knowledge lacks a fundamental knowledge on the role of suspended sediment and bed sediment characteristics, *i.e.,* sediment settling velocity, on WCSTCs, especially when sediment suspension is sourced from the seafloor.

3.1.2. BACKGROUND OF GOVERNING PHYSICS AND RESEARCH QUESTIONS

Dependence of WCSTCs and ACSTCs on near-bed turbulence makes the interaction between the suspended sediments and the ambient turbulence a critical factor to limit the cross-shelf sediment flux of WCSTCs (Wright *et al*., 2001). Physical mechanisms that affect the aforementioned interaction can be manifold: sediment-induced stable density stratification, enhanced viscosity due to cohesive sediment suspension, and hindered settling are to name a few. Among these processes, sediment-induced stable density stratification is one of the most significant mechanisms affecting WCSTCs, which is, in fact, the only mechanism to affect ACSTCs. This is because in ACSTCs, the suspended sediment concentration is dilute, *i.e.,* $\sim 1\ \mathrm{kg\,m^{-3}}$ (Wright *et al*., 2001). In such dilute sediment suspensions, sediment-sediment interaction becomes negligible, and sediment-induced stable density stratification becomes the dominant mechanism. Indeed, the only available conceptual framework for WCSTCs (Wright *et al*., 2001) considers the sediment-induced stable density stratification as the sole governing physical process in WCSTCs.

In a non-cohesive sediment-laden turbulent channel flow, stable density stratification is primarily affected by the total sediment concentration and the sediment settling velocity. If the total suspended sediment load is constant, sediment settling velocity enhances sediment-induced stable density stratification because the concentration gradient of sediment suspension increases with the increasing settling velocity (Winterwerp, 2001; Ozdemir *et al.*, 2011; Cantero, 2012; Shringarpore *et al.*, 2012). When suspended sediment is sourced from bed erosion only, however, the role of sediment settling velocity becomes more than merely affecting the density stratification because it also imposes control on the amount of sediment suspension. To elucidate this point, let us assume Partheniades-Ariathurai-type erosion flux formula (Sanford and Maa, 2001) represents the fine sediment erosion over the bed: $E \sim (\tau_b/\tau_c - 1)$, where E is the erosion flux, τ_b is the bed shear stress, and τ_c is the critical shear stress for erosion. When $\tau_b > \tau_c$, the flow equilibrates once erosion flux becomes equal to the deposition flux, D. Denoting c_b as the volumetric sediment concentration at the bed, the deposition flux is $D \sim w_s c_b$, where w_s is the sediment settling velocity, and thus $c_b \sim w_s^{-1}(\tau_b/\tau_c - 1)$. This suggests that decreasing sediment settling velocity will lead to a higher sediment concentration at the bed and, likely, higher total sediment concentration. From the above description, one can infer two counter roles of settling velocity over the erodible bed. Increasing sediment settling velocity itself enhances the density stratification through increasing the sediment concentration gradient, but limits the sediment suspension from the bed, and hence decreases the density stratification. Limited sediment suspension will reduce the cross-shelf velocity of the turbidity current; conversely, decreasing sediment settling velocity will increase the sediment suspension and thus the cross-shelf velocity of the turbidity current.

The fact that near-bed turbulence is augmented by the ACSTC with increasing suspended sediment concentration further complicates the role of settling velocity. Over an erodible bed,

decreasing settling velocity, and thus increasing sediment suspension, can initiate a positive feedback loop between the sediment concentration and the near-bed turbulence whereby augmented turbulence due to increasing down-slope force, conceivably, erodes sediments further; increased suspension can further augment the down-slope force and further suspend sediments. Here, it is hypothesized that the given positive feedback loop continues until the ACSTC transitions to an auto-suspending or self-accelerating turbidity current. Alternatively, it can be counter-hypothesized that increasing suspension enhances the stable density stratification, and can, therefore, inhibit turbulence growth and even terminate the ACSTC through laminarization as was observed in wave-driven boundary-layer flows (Cheng *et al.*, 2015a).

Direct numerical simulation results reported in Ozdemir and Yu (2018) provide partial support to both hypotheses above. In Ozdemir and Yu (2018), the role of total sediment concentration and the settling velocity on ACSTCs was investigated; however, in Ozdemir and Yu (2018) the total sediment concentration was fixed, and no erosion from the bed was allowed. The results in the same study suggest that a high-concentration turbidity current, *i.e.,* $\sim\mathcal{O}(1\ \mathrm{kg\ m^{-3}})$, with low sediment settling velocity, *i.e.,* $\sim\mathcal{O}(1\times10^{-5}\ \mathrm{m\ s^{-1}})$, can transition to a self-driven turbidity current for bed shear stress on the order of $\sim\mathcal{O}(1\times10^{-3}\ \mathrm{Pa})$. Ozdemir and Yu (2018) also reported that an order of magnitude increase in settling velocity would make the density stratification the limiting physical mechanism, and ACSTCs are terminated for a sediment load of $0.1\sim0.5\ \mathrm{kg\ m^{-3}}$. Over an erodible bed, however, sediment concentration is governed by erosion and deposition fluxes, where sediment settling velocity becomes one of the governing parameters of sediment suspension. These observations motivated us to investigate the two competing roles of decreasing settling velocity. Particularly, we seek answers to the following research questions.

(i) Does a decreasing settling velocity, thus increasing sediment suspension, lead to a continuous erosion that will create a self-driven turbidity current due to enhanced turbulence production, or terminate the ACSTC by laminarizing the flow due to stable density stratification?

(ii) If either of the above scenarios holds, what is the critical sediment settling velocity that delineates continuous erosion or termination of ACSTCs for a given set of erosion parameters?

To help quantify the limits of possible laminarization and transition to self-driven turbidity current for a given near-bed turbulence level, we further ask the following:

(iii) What are the relationships between the settling velocity and total sediment concentration, the settling velocity and turbulence production, as well as the settling velocity and buoyant dissipation?

This chapter is structured as follows. In Section 1, the characteristics of WCSTCs, and the research objectives with relevant literature are described. In Section 2, the description of the problem, the governing equations, the numerical methods, the selection of the parametric space, and the justification for the selected parameters are provided. Section 3 presents the simulation results with detailed analyses. Section 4 summarizes the findings and gives conclusions with research prospects.

3.2. METHODS

3.2.1. PROBLEM DESCRIPTION AND DESIGN OF NUMERICAL EXPERIMENTS

To address the research questions posed in Section 1, we employed DNS of a steady, fully-developed, turbulent, fine particle-laden channel flow over a smooth erodible bed with mild spanwise slope, *i.e.*, $\sin\theta < 0.012$ (Wright *et al.*, 2001). Along-shelf, or shore-parallel, currents are mimicked by a unidirectional turbulent flow in the streamwise direction. The shear stress associated with the along-shelf current, or the streamwise flow in our numerical setup, erodes

sediments from the bed and suspends them into the water column. At the same time, sediment suspension creates a spanwise gravity force and initiates a flow in the same direction. The flow generated in the spanwise direction is a close approximation of the ACSTC.

While designing our numerical experiments, we took the hydrodynamic conditions similar to those in the Gulf of Bohai (Wright *et al*., 1988, 2001). In the Gulf of Bohai, the depth was 5 m, and the current velocity at the sea surface ranged from 0.15 m s^{-1} to 0.70 m s^{-1}. We assumed the surface current velocity as 0.10 m s^{-1} for a five-meter depth, which is reasonably close to the least energetic hydrodynamic conditions in the Gulf of Bohai. Assuming that the law of the wall applies, one can obtain the friction velocity to be $\tilde{u}_{\tau o} = 3.6 \times 10^{-3}$ m s^{-1} and the bed shear stress to be $\tilde{\tau}_{bo} = 0.013$ Pa. Note that the tilde caps differentiate the dimensional variables and parameters from their non-dimensional counterparts in this chapter. The values obtained for the bed shear stress and the friction velocity form the basis of our hydrodynamic conditions. However, simulating the flow in the entire depth would be prohibitively expensive in terms of its computational cost. Therefore, we only selected a rectangular prism-shaped computational domain extending 0.1 m above the seafloor (See Fig. 2). The range of sediment size we selected is $\tilde{d} = [6\ \mu\text{m}, 20\ \mu\text{m}]$, and for the selected sediment size, suspended sediment concentration mostly remains close to the seafloor and diminishes to negligible values at the top of the domain, which justifies the vertical extent of the domain. Associated with the domain we selected, further description of the boundary conditions and the domain size along with their justifications are deferred to Section 2.4, where their detailed mathematical description will be provided.

3.2.2. DIMENSIONAL GOVERNING EQUATIONS

Dynamics of turbidity currents in general and that of ACSTCs are two-phase flow problems whereby sediment suspension and the carrier fluid, which is water in this study, are treated

separately. According to previous studies on WCSTCs (Meiburg and Kneller, 2010; Ozdemir *et al*., 2010, 2011), the sediment phase velocity, $\widetilde{\boldsymbol{u}}^s$, is expressed in terms of the fluid velocity and the sediment settling velocity as

$$\widetilde{\boldsymbol{u}}^s = \widetilde{\boldsymbol{u}}^f + \widetilde{w}_s \boldsymbol{e_g}, \tag{1}$$

where $\widetilde{\boldsymbol{u}}^f = (\tilde{u}^f, \tilde{v}^f, \widetilde{w}^f)$ is the fluid velocity vector, and $\tilde{u}^f$, $\tilde{v}^f$, and $\widetilde{w}^f$ are the velocity components in the streamwise, spanwise, and bed-normal directions, respectively. In Equation (1), the representative sediment settling velocity is denoted as $\widetilde{w}_s$, and the unit vector that points in the direction of the gravitational acceleration is denoted as $\boldsymbol{e_g}$, where $\boldsymbol{e_g} = \sin\theta\, \boldsymbol{e_y} - \cos\theta\, \boldsymbol{e_z}$ with $\boldsymbol{e_y}$ and $\boldsymbol{e_z}$ being the unit vectors pointing in the spanwise and bed-normal directions, respectively. The size of sediments ranges between 6 μm to 20 μm, which is small; therefore, the dimensional settling velocity of spherical sediments with uniform diameter, $\tilde{d}$, can be calculated based on the Stokes Law:

$$\widetilde{w}_s = \frac{(s-1)\tilde{g}\tilde{d}^2}{18\tilde{\nu}_f}. \tag{2}$$

In Equation (2), $s = \tilde{\rho}_s/\tilde{\rho}_f$ is the specific gravity of sediment, $\tilde{\rho}_s$ is the sediment density, $\tilde{\rho}_f$ is the density of water, $\tilde{g}$ is the magnitude of gravitational acceleration, and $\tilde{\nu}_f$ is the kinematic viscosity of water.

For dilute sediment suspension ($c < 1\%$), it can be approximated that the fluid phase satisfies the continuity equation. Dilute sediment concentration also allows for adopting the Boussinesq approximation in the momentum equation. Thus, the continuity and momentum equations of the fluid phase become

$$\widetilde{\boldsymbol{\nabla}}.\widetilde{\boldsymbol{u}}^f = 0, \tag{3}$$

$$\frac{\partial \tilde{\boldsymbol{u}}^f}{\partial \tilde{t}} + \tilde{\boldsymbol{u}}^f . \tilde{\boldsymbol{\nabla}} \tilde{\boldsymbol{u}}^f = -\frac{\tilde{u}_{\tau 0}^2}{\tilde{h}} \boldsymbol{e_x} - \frac{\tilde{\boldsymbol{\nabla}} \tilde{p}'}{\tilde{\rho}_f} + (s-1)\tilde{g} c \boldsymbol{e_g} + \tilde{\nu}_f \tilde{\nabla}^2 \tilde{\boldsymbol{u}}^f, \quad (4)$$

where $\tilde{u}_{\tau o} = \left(\tilde{\tau}_{bo}/\tilde{\rho}_f\right)^{1/2}$ is the initial friction velocity with $\tilde{\tau}_{bo}$ being the initial bed shear stress, and $\tilde{h}$ is the channel depth. Here, the initial bed shear stress and the friction velocity correspond to those when sediment suspension is absent or the sediments are neutrally buoyant (Case 0 in Table 1); therefore, both $\tilde{\tau}_{bo}$ and $\tilde{u}_{\tau o}$ are the measures of the bed shear associated with along-shelf currents only. The first term on the right-hand side of the Equation (4) is the mean pressure gradient that drives the streamwise flow. The spanwise component of the buoyancy term, $(s-1)\tilde{g}\ c \sin\theta\ \boldsymbol{e_y}$, drives the spanwise motion. The sediment-induced stable density stratification is accounted through the vertical component of the buoyancy term, $-(s-1)\tilde{g}\ c \cos\theta\ \boldsymbol{e_z}$. The sediment phase is treated as a continuum, and the governing equation for sediment phase is given as

$$\frac{\partial c}{\partial \tilde{t}} + \tilde{\boldsymbol{u}}^s . \tilde{\boldsymbol{\nabla}}\, c = \tilde{\mathfrak{D}} \tilde{\nabla}^2 c, \quad (5)$$

where $\tilde{\mathfrak{D}}$ is the diffusivity of the sediment concentration. The governing equations are solved in their dimensionless form. Therefore, the dimensionless form of the equations will be provided in the next subsection.

3.2.3. DIMENSIONLESS EQUATIONS AND PARAMETERS

The length and velocity scales that normalize the governing equations are the channel depth, $\tilde{h}$, and the initial friction velocity, $\tilde{u}_{\tau o}$, respectively. Hence, the time scale becomes $\tilde{h}/\tilde{u}_{\tau o}$, and the non-dimensional variables are obtained as

$$\boldsymbol{u}^f = \frac{\tilde{\boldsymbol{u}}^f}{\tilde{u}_{\tau 0}}, \quad (6a)$$

$$\boldsymbol{x} = \frac{\tilde{\boldsymbol{x}}}{\tilde{h}}, \quad (6b)$$

$$t = \frac{\tilde{t}\tilde{u}_{\tau 0}}{\tilde{h}}, \tag{6c}$$

and

$$p' = \frac{\tilde{p}'}{\tilde{\rho}_f \tilde{u}_{\tau 0}^2}, \tag{6d}$$

where $\boldsymbol{x} = (x, y, z)$ is the position vector. With the given scaling, Equation (3-5) become

$$\boldsymbol{\nabla}.\boldsymbol{u}^f = 0, \tag{7}$$

$$\frac{\partial \boldsymbol{u}^f}{\partial t} + \boldsymbol{u}^f.\boldsymbol{\nabla}\,\boldsymbol{u}^f = -\boldsymbol{e_x} - \boldsymbol{\nabla}p' + \frac{1}{Fr_{\tau 0}^2} c\boldsymbol{e_g} + \frac{1}{Re_{\tau 0}} \nabla^2\,\boldsymbol{u}^f, \tag{8}$$

$$\frac{\partial c}{\partial t} + \boldsymbol{u}^s.\boldsymbol{\nabla}\,c = \frac{1}{Re_{\tau 0} Sc} \boldsymbol{\nabla}^2 c. \tag{9}$$

Note from Equation (7-9) that there are three dimensionless parameters. These are the densimetric Froude number, $Fr_{\tau o}$, the Reynolds number, $Re_{\tau o}$, and the Schmidt number, S_c, which are defined as

$$Fr_{\tau 0} = \tilde{u}_{\tau 0}[(s-1)\tilde{g}\tilde{h}]^{-1/2}, \tag{10a}$$

$$Re_{\tau 0} = \frac{\tilde{u}_{\tau 0}\tilde{h}}{\tilde{\nu}_f}, \tag{10b}$$

and

$$Sc = \frac{\tilde{\nu}_f}{\tilde{\mathfrak{D}}}. \tag{10c}$$

Here, the densimetric Froude number, $Fr_{\tau o}$, is a measure of the buoyancy force per unit sediment concentration, $Re_{\tau o}$ is the Reynolds number for the clear fluid case and is a measure of boundary-layer turbulence. The Schmidt number, S_c, is the ratio between the kinematic viscosity and sediment diffusivity. The effect of sediment diffusion on the ambient flow is considered

negligible provided that $\widetilde{\mathfrak{D}} \leq \tilde{\nu}_f$ (Härtel *et al.*, 2000). Therefore, the Schmidt number is specified to be equal to unity.

To address the questions posed in Section 1, six cases were simulated for various settling velocities, while other parameters are kept constant. In these simulations, the spanwise slope is selected as $\sin\theta = 0.01$. The selected spanwise slope is sufficiently mild based on the criterion proposed by Wright *et al.* (2001), where they define a critical slope of $\sin\theta_c = 0.012$. Slopes steeper than the critical slope was conjectured to become auto-suspending (Wright *et al.*, 2001). As mentioned in Section 3.2.1, a domain height of $\tilde{h} = 0.1$ m is selected due to computational limitations. Also mentioned in Section 3.2.1, we assumed a surface current velocity of 0.10 m s^{-1}, which yields a bed friction velocity of $\tilde{u}_{\tau o} = 3.6 \times 10^{-3}$ m s^{-1}. Assuming the kinematic viscosity of seawater as $\tilde{\nu}_f = 1 \times 10^{-6}$ m^{2}s^{-1}, one can obtain $Re_{\tau o} = \tilde{u}_{\tau o}\tilde{h}/\tilde{\nu}_f = 360$. It is worth noting that at $Re_{\tau o} = 360$, turbulence becomes sufficiently developed, and hence shows the main features of a turbulent boundary-layer with a reasonable computational expense. Although $Re_{\tau o} = 360$ characterizes the turbulence generated by the along-shelf current, the spanwise turbidity current introduces additional turbulence. Therefore, it is more appropriate to calculate the viscous length and velocity scales by taking the bed shear stress created by both the streamwise and spanwise flows into account. Once the dynamic equilibrium is established, the shear stress opposing the spanwise turbidity current is obtained as the total gravity force of the sediment suspension in the spanwise direction, which is $\tilde{\tau}_{b,y} = \tilde{\rho}_f(s-1)\tilde{g}\tilde{h}\langle\langle c\rangle\rangle \sin\theta$. Having $\tilde{\tau}_{bo}$ as the bed shear stress in the streamwise direction, the total stress can be calculated as

$$|\tilde{\boldsymbol{\tau}}_b| = (\tilde{\tau}_{b0}^2 + \tilde{\tau}_{b,y}^2)^{1/2} = \left\{(\tilde{\rho}_f\tilde{u}_{\tau 0}^2)^2 + [\tilde{\rho}_f(s-1)\tilde{g}\tilde{h}\langle\langle c\rangle\rangle \sin\theta]^2\right\}^{1/2}. \qquad (11)$$

It is worth noting that such evaluation of total bed shear stress is commonly utilized in flows that have directional variation such as those in the turbulent Ekman boundary layers (Spalart *et al.*,

2008; Schlatter *et al*., 2010; Deusebio *et al*., 2014). Total bed shear stress in dimensionless form is obtained after its dimensional counterpart is normalized by $\tilde{\rho}_f \tilde{u}_{\tau o}^2$:

$$|\boldsymbol{\tau}_b| = \left[1 + \left(\frac{\langle\langle c\rangle\rangle \sin\theta}{Fr_{\tau 0}^2}\right)^2\right]^{1/2}. \tag{12}$$

Correspondingly, the total bed friction velocity becomes

$$u_\tau = \left[1 + \left(\frac{\langle\langle c\rangle\rangle \sin\theta}{Fr_{\tau 0}^2}\right)^2\right]^{1/4}. \tag{13}$$

where $\langle\langle c\rangle\rangle$ is the volume-averaged sediment concentration in the domain. Note that plane- and volume-averaged quantities are identified by the single and double angle brackets, respectively. Thus, $Re_\tau = \tilde{u}_\tau \tilde{h}/\tilde{\nu}_f$ is a more proper measure of boundary-layer turbulence, where one can obtain the relation between Re_τ and $Re_{\tau 0}$ as

$$Re_\tau = Re_{\tau 0}\left[1 + \left(\frac{\langle\langle c\rangle\rangle \sin\theta}{Fr_{\tau 0}^2}\right)^2\right]^{1/4}. \tag{14}$$

Similarly, Fr_τ can also be defined as

$$Fr_\tau = \tilde{u}_\tau\left[(s-1)\tilde{g}\tilde{h}\right]^{-1/2}. \tag{15}$$

Since the only difference between $Fr_{\tau o}$ and the Fr_τ is the velocity scale, the following equation can be used to convert $Fr_{\tau o}$ to Fr_τ

$$Fr_\tau = Fr_{\tau 0}\left[1 + \left(\frac{\langle\langle c\rangle\rangle \sin\theta}{Fr_{\tau 0}^2}\right)^2\right]^{1/4}. \tag{16}$$

As will be substantiated in Section 3.3.2, suspended sediment concentration is sufficiently small. Hence, sediment-sediment interaction is considered to be negligible. Therefore, any physical mechanism associated with sediment-sediment interaction such as flocculation and hindered settling are neglected. With these simplifications, the sediment settling velocity, w_s,

becomes constant for uniform sediment size distribution. The range of non-dimensional settling velocity is chosen within $w_s \sim 0.01 - 0.1$ which corresponds to a particle size range of $\tilde{d} \sim 6.3 \times 10^{-6}$ m $- \ 19.8 \times 10^{-6}$ m, which is typical for turbidity currents in general (Meiburg and Kneller, 2010).

As will be noted in the following sections, a reference case without sediments at $Re_{\tau o} = 360$ (Case 0 in Table 1) will be used for baseline comparison. The velocity field of Case 0 at its latest time step is used as the initial condition for cases 1-6 with lower resolution, *i.e.*, $N_x \times N_y \times N_z = 192 \times 96 \times 129$. The velocity and concentration of the lower resolution cases at their latest time step are later used as the initial condition for the same cases with higher resolution, *i.e.*, $N_x \times N_y \times N_z = 256 \times 128 \times 257$. To obtain accurate and reliable statistics, we ran the simulations long enough after the statistical equilibrium is established. The inception of stationarity is determined from the volume-averaged spanwise velocity, which reaches the stationarity the latest.

Table 3.1. List of conducted simulations. All parameters are in their non-dimensional forms. The number of grid points in x-, y-, and z-directions are denoted as N_x, N_y, and N_z, respectively. Reynolds number ($Re_{\tau o} = 360$) and Froude number ($Fr_{\tau_o} = 2.8 \times 10^{-3}$) are specified as constants for all the cases. To characterize the boundary-layer turbulence created by both streamwise and spanwise flows, Re_τ and Fr_τ parameters (See Equations (14-16)) are defined that are changing with respect to settling velocity, w_s, and total sediment concentration, $\ll c \gg$. Since cases 1 and 2 have not reached the stationarity state, Re_τ and Fr_τ cannot be determined for these cases. The spanwise bed gradient, $\sin\theta$, erosion coefficient, m_e, and critical shear stress, τ_c, are also kept constant for all the cases.

Case	$N_x \times N_y \times N_z$	w_s	Re_τ	Fr_τ	$\sin\theta$	$m_e(1-\phi)$	τ_c
0	192×96×129	-	360	-	0	-	-
1	256×128×257	0.01	-	-	0.01	0.0001	0.9
2	256×128×257	0.02	-	-	0.01	0.0001	0.9
3	256×128×257	0.04	365	2.9×10^{-3}	0.01	0.0001	0.9
4	256×128×257	0.06	361	2.84×10^{-3}	0.01	0.0001	0.9
5	256×128×257	0.08	360.3	2.81×10^{-3}	0.01	0.0001	0.9
6	256×128×257	0.1	360.1	2.8×10^{-3}	0.01	0.0001	0.9

3.2.4. BOUNDARY CONDITIONS AND DOMAIN SIZE

After normalizing by $\tilde{h}$, the size of the computational domain is 4π, 2π, and 1 in the streamwise, spanwise, and bed-normal directions, respectively (Fig. 2). The number of grid points is 256, 128, and 257 in the streamwise, spanwise, and bed-normal directions, respectively. The domain size and grid resolution are specified such that they are sufficient to capture the whole spectrum of turbulent scales (See Appendices B1 and B2). While the grid spacing is uniform in x- and y-directions, Chebyshev-Gauss-Lobbato collocation points are used for discretization in the bed-normal direction (Canuto *et al.*, 1987).

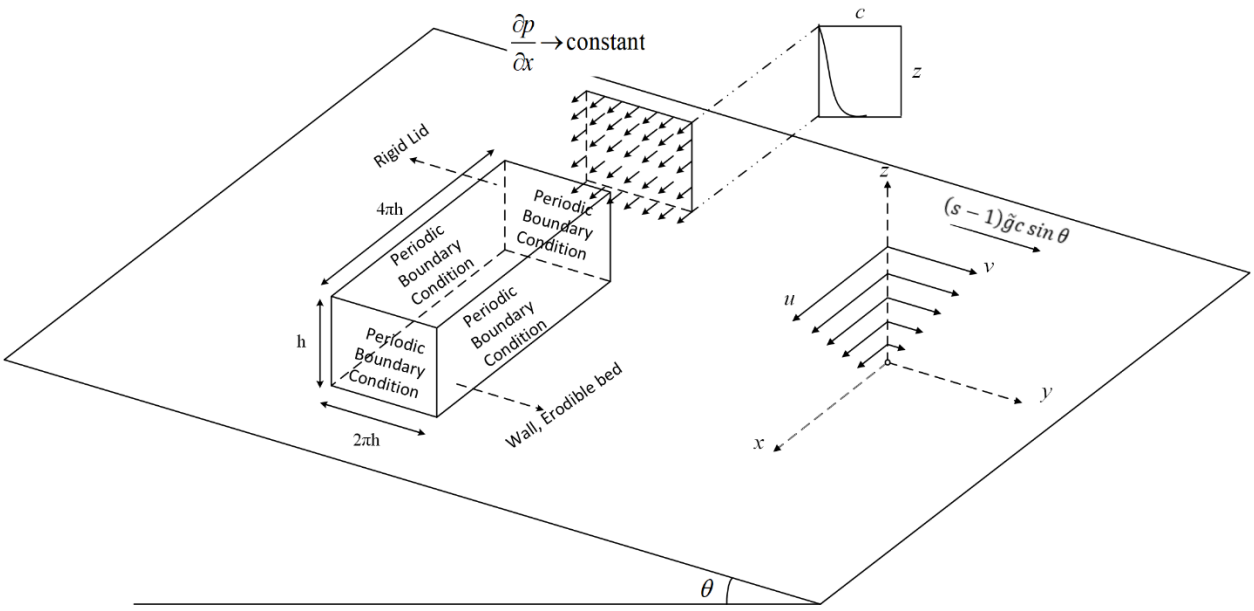

Figure 3.2. Illustrative sketch of the model domain. The dimensional size of the computational domain is $\tilde{L}_x \times \tilde{L}_y \times \tilde{L}_z = 4\pi\tilde{h} \times 2\pi\tilde{h} \times \tilde{h}$ in the streamwise, spanwise, and bed-normal directions, respectively (not to scale). While periodic boundary condition is adopted in the $x-y$ planes, wall and rigid-lid boundary conditions are imposed at the top and bottom planes, respectively, for the velocity field. Erosional/depositional boundary condition is applied at the bed. The mean current is forced by a uniform pressure gradient in the x-direction, while the spanwise turbidity current is driven by depth-dependent buoyancy force due to suspended sediment concentration, $(s-1)\tilde{g}c\,sin\,\theta$, in the y-direction due to bed gradient, $sin\,\theta$. Arrows in x- and y-directions represent the components of the velocity vector in the streamwise and spanwise directions, respectively. The panel at the topmost part of the figure represents the suspended sediment concentration profile.

Periodic boundary conditions are imposed along the streamwise and spanwise directions for both the fluid and sediment phases. Periodic boundary conditions are not suitable for

classical turbidity currents of highly transient characteristics. However, it should be noted that ACSTCs last over time scales of tidal cycles. Considering that the velocity of ACSTCs are slower (~ 0.1 m s^{-1}), an equilibrium can quickly be established (Wright *et al*., 2001; Scully *et al*., 2002; Friedrichs and Wright, 2006; Flores *et al*., 2018). Indeed, the equilibrium assumption is tested, and its presence is verified in the field by Flores *et al*. (2018). Therefore, due to the spatial and temporal homogeneity of ACSTCs, we believe that imposing periodic boundary conditions is justifiable.

For the velocity field, the bottom plane of the domain is specified as no-slip and no-penetration wall boundary, *i.e.*, $\boldsymbol{u}^f = 0$, and the top of the domain is specified as free-slip and no-penetration boundary (rigid lid), *i.e.*, $\frac{\partial u^f}{\partial z} = \frac{\partial v^f}{\partial z} = 0$ and $w^f = 0$. The velocity at the top, *i.e.*, $\tilde{z} = 0.10\ m$, without any sediment suspension, using law of the wall, is $\tilde{u} = 0.07$ m s^{-1}. Here, we would like to point out the fact that the difference between the velocities at $\tilde{z} = 0.10\ m$ and the assumed sea surface level, *i.e.*, $\tilde{z} = 5$ m, is only 0.03 m s^{-1}. This suggests that the shear at the top boundary is negligible, and the free-slip boundary condition at the top has minimal impact on the flow.

At the bed, erosional/depositional boundary condition is specified to allow sediment erosion (deposition) from (to) the bed:

$$-\frac{1}{Re_{\tau 0} Sc}\frac{\partial c}{\partial z}\Big|_{Z=0} = E - D. \tag{17}$$

In Equation (17), E is the erosion flux, which is calculated through Partheniades-Ariathurai-type formulation (Sanford and Maa, 2001):

$$E = \begin{cases} m_e(1-\phi)\left(\dfrac{|\boldsymbol{\tau}_b|}{\tau_c} - 1\right) & |\boldsymbol{\tau}_b| \geq \tau_c \\ 0 & |\boldsymbol{\tau}_b| < \tau_c \end{cases}, \tag{18}$$

where m_e is the empirical coefficient of erosion rate, and ϕ is the porosity. The bed shear stress, $\boldsymbol{\tau}_b$, used in Equation (18) is calculated in each time step as

$$|\boldsymbol{\tau}_b| = \frac{1}{Re_{\tau o}} \left| \frac{\partial \boldsymbol{u}^f}{\partial z} \right|_{z=0}. \tag{19}$$

Note that m_e and τ_c are dimensionless and are obtained after normalizing their dimensional counterparts, namely $\widetilde{m}_e$ (m s^{-1}) and $\tilde{\tau}_c$ (Pa), which are given as

$$m_e = \frac{\widetilde{m}_e}{\tilde{u}_{\tau o}}, \tag{20}$$

and

$$\tau_c = \frac{\tilde{\tau}_c}{\tilde{\rho}_f \tilde{u}_{\tau o}^2}. \tag{21}$$

The deposition flux is specified as in the following:

$$D = w_s c \Big|_{z=0}. \tag{22}$$

For simplicity, we assumed that sediments are sourced from loose fine sediment deposits. Therefore, both $m_e(1-\phi)$ and τ_c are considered to be constant and equal to $m_e(1-\phi) = 1 \times 10^{-4}$ and $\tau_c = 0.9$. The selected erosion parameter values are based on the study by Curran *et al.* (2007), where a loose fine sediment layer can be suspended by the bottom shear stress as low as $0.01\ Pa$, which becomes close to 0.9 upon normalization.

3.2.5. NUMERICAL METHODS

In this study, the FineSed3D model (Cheng *et al.*, 2015a, 2015b) is employed. An in-depth description of the model can be found in Cheng *et al.* (2015a). Therefore, we will briefly describe the numerical methods. FineSed3D uses a hybrid spectral-compact finite difference scheme to solve the governing equations. Pseudo-spectral methods are utilized in the periodic directions whereby the variables are expanded as Fourier series. In the inhomogeneous bed-normal direction

a sixth-order accurate compact finite difference scheme is implemented to evaluate the bed-normal gradients. Time integration is performed through a low-storage hybrid scheme, where the diffusive terms are computed via semi-implicit second-order Crank-Nicolson method, and the non-linear terms are integrated by third-order-accurate, low-storage Runge-Kutta method (Cortese and Balachandar, 1995; Cantero *et al.*, 2008). Aliasing errors are minimized by using 3/2 rule (Canuto *et al.*, 1987; Peyret, 2002), and Arakawa method (Arakawa, 1981). For further details, the reader is referred to Cheng *et al.* (2015a).

3.3. RESULTS

3.3.1. OVERVIEW

One of the objectives of this chapter is to test the hypothesis that decreasing the settling velocity of suspended fine sediments can lead an ACSTC to a turbidity current in auto-suspension or self-accelerating modes over an erodible bed. The aforementioned hypothesis can be tested by realizing the possible positive feedback loop between the suspended sediment concentration and the near-bed turbulence that leads to continually increasing the erosion flux. It is expected that the continual increase will terminate once the turbidity current reaches the auto-suspension mode or continue to grow indefinitely in self-accelerating mode. The setup of the numerical simulations allows for infinite sediment erosion from the seafloor. As such, the self-accelerating current may occur upon further running the simulations that are continually eroding sediments from the bed. However, the specified domain size will not be sufficient to capture the natural growth of either auto-suspending or self-accelerating turbidity currents. While growing, the turbidity current will upraise due to additional suspension and turbulence. However, if the simulations are kept running for growing turbidity currents, the turbidity current will be forced to reside in a 0.1-m layer from the seafloor due to boundary conditions at the top of the domain. The results of those simulations would,

therefore, be unphysical. In addition, due to growing turbulence, the resolution of the numerical simulations will be inadequate for self-accelerating and auto-suspending turbidity currents. Yet, one can obtain sufficient information for the transition of ACSTCs to either auto-suspending or self-accelerating turbidity currents via the time history of the volume-averaged sediment concentration, $\langle\langle c\rangle\rangle$, the spanwise velocity, $\langle\langle v\rangle\rangle$, and the plane-averaged wall shear stress relative to the initial bed shear stress, $\langle\tau_b\rangle/\tau_{bo}$. If $\langle\langle c\rangle\rangle$, $\langle\langle v\rangle\rangle$, and $\langle\tau_b\rangle/\tau_{bo}$ exhibit a continual increase in time without reaching a statistical equilibrium, and $\langle\tau_b\rangle/\tau_{bo}$ shows substantial deviation from unity, it can be conjectured that the positive feedback loop between the suspended sediment concentration and the near-bed turbulence is established. The time history of $\langle\langle c\rangle\rangle$, $\langle\langle v\rangle\rangle$, and $\langle\tau_b\rangle/\tau_{bo}$ are shown in Fig. 3.

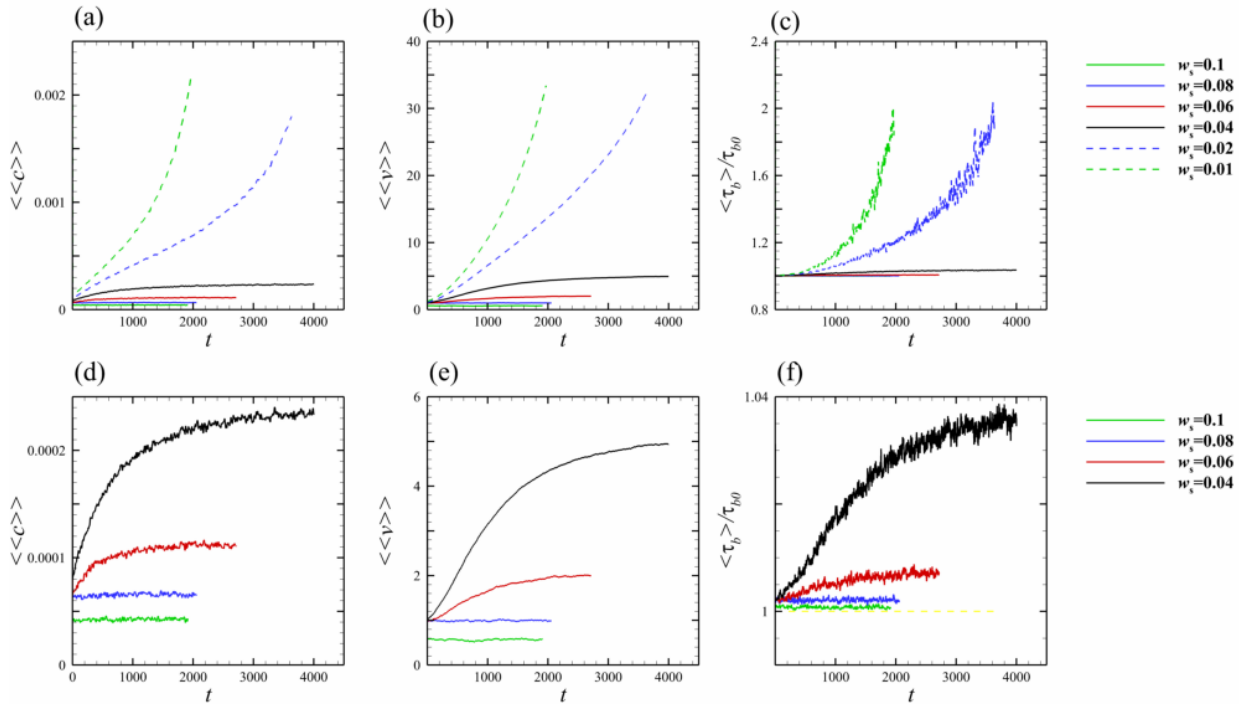

Figure 3.3. Time history of (a) volume-averaged sediment concentration, $\langle\langle c\rangle\rangle$, (b) volume-averaged spanwise velocity, $\langle\langle v\rangle\rangle$, and (c) plane-averaged wall shear stress relative to the initial bed shear stress, $\langle\tau_b\rangle/\tau_{bo}$, of Cases 1 to 6. The zoomed-in time history of $\langle\langle c\rangle\rangle$, $\langle\langle v\rangle\rangle$, and $\langle\tau_b\rangle/\tau_{bo}$, of Cases 3 to 6, are plotted in subfigures (d), (e), and (f), respectively. The yellow dashed line in subfigure (f) represents $\langle\tau_b\rangle/\tau_{bo} = 1$.

From this figure, one can observe a continuous increase in $\langle\langle c\rangle\rangle$, $\langle\langle v\rangle\rangle$, and $\langle\tau_b\rangle/\tau_{bo}$ for $w_s < 0.04$, *i.e.*, Cases 1 and 2; whereas for cases with $w_s \geq 0.04$, *i.e.*, Cases 3-6, $\langle\langle c\rangle\rangle$, $\langle\langle v\rangle\rangle$, and $\langle\tau_b\rangle/\tau_{bo}$ reach statistical stationarity in time. These results suggest that turbulence produced by the spanwise flow overcomes the density stratification created by the sediment suspension for $w_s < 0.04$ at $Re_{\tau o} = 360$. Since the cases with $w_s < 0.04$ did not reach the statistical equilibrium, change in the mean and turbulent quantities with respect to w_s can only be analyzed through the remaining cases. It is important to note that the results herein are restricted to the loose sediment deposits with constant erosion parameters. Any change in the erosion parameters would likely impact the results. However, our analyses of Cases 3-6 suggest that sediment settling velocity plays a vital role by non-linearly changing the turbulent quantities in ACSTCs and thus their transition to auto-suspending or self-accelerating turbidity currents. This will be elucidated in the following sections.

3.3.2. MEAN CONCENTRATION AND VELOCITY PROFILES

To make an initial quantitative comparison on how the sediment settling velocity determines the amount of sediment concentration in the domain, *i.e.*, $\langle\langle c\rangle\rangle$, time- and plane-averaged suspended sediment concentration profiles of cases with $w_s > 0.04$ (Cases 3-6) are plotted in Fig. 4. The time- and plane-averaged quantities, which are discerned by an overbar, ($\overline{\ }$), are obtained after averaging the quantity of interest both in time and over the $x-y$ plane at a bed-normal distance of z from the bed. Hence, time- and plane-averaged suspended sediment concentration reads

$$\bar{c}(z) = \frac{1}{TL_xL_y}\int_{t=t_o}^{t=t_o+T}\int_{y=0}^{y=L_y}\int_{x=0}^{x=L_x} c(x,y,z,t)\,\mathrm{d}x\mathrm{d}y\mathrm{d}t, \tag{23}$$

where t_o is the instant when the flow reaches the statistical equilibrium (or stationarity), and T is the time elapsed after t_o. For reference, the Rouse profile for Case 6 is also shown in Fig. 4(a), where the Rouse profile is given in both dimensional and dimensionless forms as:

$$C(\tilde{z}) = C_R \left[\left(\frac{\tilde{h} - \tilde{z}_R}{\tilde{h} - \tilde{z}} \right) \left(\frac{\tilde{z}}{\tilde{z}_R} \right) \right]^{-\frac{\tilde{w}_s}{\kappa \tilde{u}_\tau}}, \tag{24a}$$

and

$$C(z) = C_R \left[\left(\frac{1 - z_R}{1 - z} \right) \left(\frac{z}{z_R} \right) \right]^{-\frac{w_s}{\kappa}}. \tag{24b}$$

Here, z_R and C_R are the reference distance from the bed and the sediment concentration at z_R, respectively. For Case 6, the von Kármán constant reduces to $\kappa = 0.34$. Therefore, the modulated von Kármán constant ($\kappa = 0.34$) is used for evaluating the Rouse profile. As shown in Fig. 4(a), the sediment concentration profile and the Rouse profile are close above the reference point, $z_R = 0.08$.

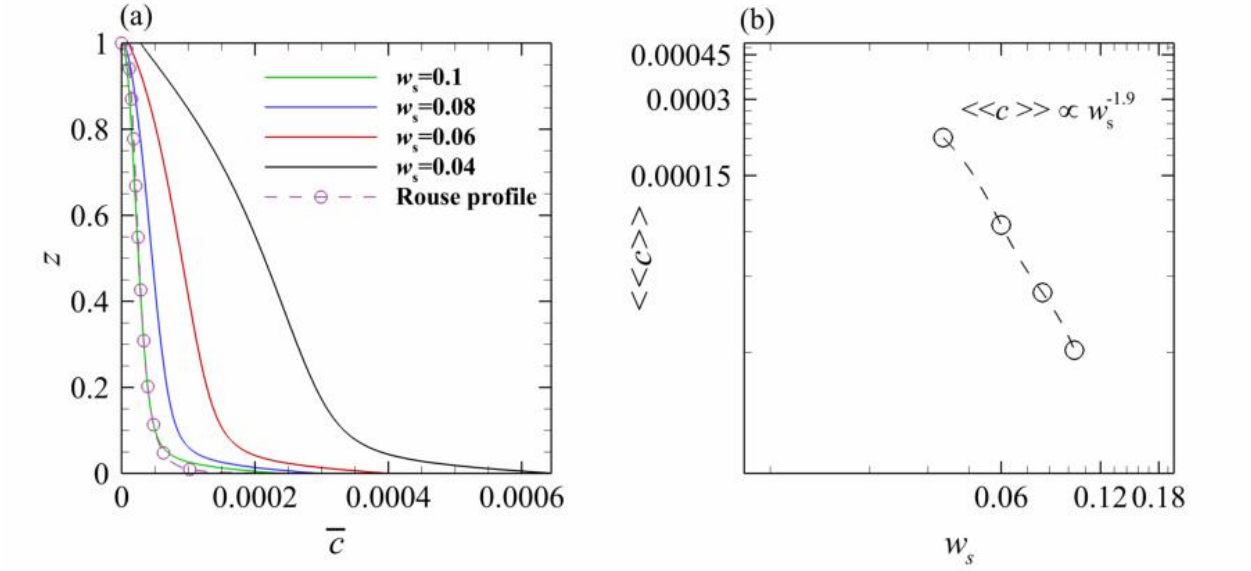

Figure 3.4. (a) Time- and domain-averaged concentration, $\bar{c}$, profiles of Cases 3 to 6, for reference Rouse profile for case 6 is also added. (b) The variation of total concentration, $\langle\langle c \rangle\rangle$, with respect to settling velocity, w_s, both axes are in log scale. The hollow circles in subfigure (b) represent the simulation results.

According to Fig. 4(a), with the decrease in settling velocity, more sediment suspension is expected as the depositional flux decreases. As expected, the concentration is overall smaller for higher settling velocity cases than those of the lower ones except close to the bed. As w_s is one of the governing parameters of $\langle\langle c \rangle\rangle$, the variation of $\langle\langle c \rangle\rangle$ with respect to w_s is shown in Fig. 4(b). Although it is cautioned that the number of simulations is not sufficient for definitive conclusions, the results suggest an inverse power relation between $\langle\langle c \rangle\rangle$ and w_s, *i.e.*, $\langle\langle c \rangle\rangle \propto w_s^{-1.9}$.

To investigate the effect of settling velocity and resultant suspended sediment concentration on the flow characteristics, time- and plane-averaged streamwise and spanwise velocity profiles, *i.e.*, $\overline{u}$ and $\overline{v}$, respectively, are analyzed (See Fig. 5). The clear fluid case (Case 0) is also plotted in the same figure for reference.

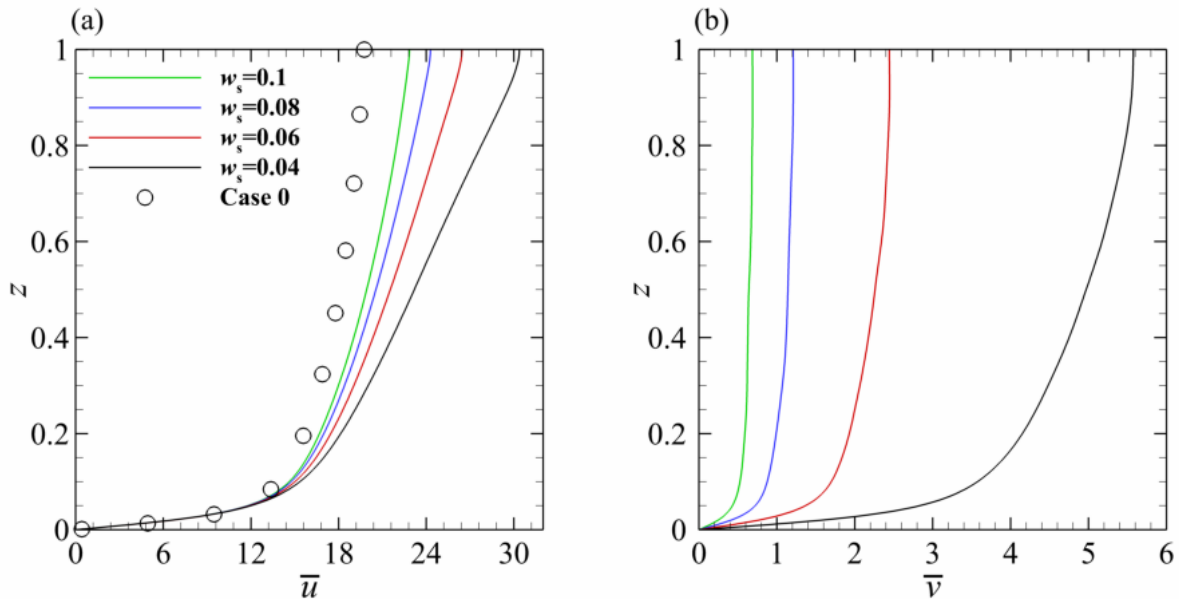

Figure 3.5. Time- and plane-averaged (a) streamwise, and (b) spanwise velocity profiles of Cases 3 to 6. Case 0 is plotted as a reference in hollow circle symbols in subfigure (a).

From Fig. 5(a) one can observe that the streamwise velocity components fall into a single curve below $z = 0.1$. The agreement of the streamwise velocity components within this layer is a likely consequence of the dominant boundary-layer effect. Above $z = 0.1$, the streamwise velocity

increases with the decrease in w_s. One can also notice an increase in the streamwise velocity gradient for $z > 0.1$; a point that will be discussed shortly. With decreasing w_s, an increase in the spanwise velocity can also clearly be observed. In summary, w_s imposes control on velocity profiles in that with the decrease in w_s, the suspended sediment concentration increases, which dissipates turbulence. The dissipation in turbulence gives rise to an increase in viscous shear stress and, thus, leads to higher streamwise velocity. In addition, the increase in suspended sediment concentration increases the cross-shelf velocity, which is concentration dependent.

To verify this conjecture, we assessed the degree of stable density stratification through the velocity profiles in wall units. In a steady unidirectional turbulent boundary-layer flow over a smooth bed, the velocity in the log layer follows $u^+ = 1/\kappa \ln(z^+) + B$, where superscript + discerns the wall units, and κ and B are the von Kármán and additive constants, respectively. The reason to carry out this analysis is that the reduction in the bed-normal turbulent momentum transfer increases the viscous shear stress and hence reduces the von Kármán constant, κ, in the log layer. The aforementioned reduction in κ is a well-known consequence of stable density stratification, and hence, the increase in the slope of the velocity profile will allow us to assess the degree of stable density stratification. Since the flow herein is two-directional, the mean velocity magnitude is defined as $|\overline{\boldsymbol{u}}| = \left(\overline{u}^2 + \overline{v}^2\right)^{1/2}$. The definition of the mean velocity is the same as those in similar boundary-layer problems such as those in turbulent Ekman boundary layers (Spalart *et al.*, 2008; Schlatter *et al*., 2010; Deusebio *et al*., 2014). Position and velocity vectors in wall units, respectively, are obtained as

$$\boldsymbol{x}^+ = \frac{\widetilde{u}_\tau}{\widetilde{\nu}_f}\,\widetilde{\boldsymbol{x}} = Re_\tau\,\boldsymbol{x}, \tag{25}$$

$$|\boldsymbol{u}|^+ = \frac{|\tilde{\boldsymbol{u}}|}{\tilde{u}_\tau} = \frac{|\boldsymbol{u}|}{u_\tau} = \boldsymbol{u}\left[1 + \left(\frac{\langle\langle c\rangle\rangle \sin\theta}{Fr_{\tau 0}^2}\right)^2\right]^{-1/4}, \tag{26}$$

where $\boldsymbol{x}^+ = (x^+, y^+, z^+)$ is the position vector in wall units. Figure 6 plots $|\overline{\boldsymbol{u}}|^+$ profiles for Cases 3 to 6. The clear fluid case (Case 0) is also plotted in the same figure as reference. The increasing slope of $|\overline{\boldsymbol{u}}|^+$ in the log layer with decreasing w_s is clear, which suggests the strengthening sediment-induced stable density stratification with decreasing w_s. In the next subsection, the dissipation of turbulence due to sediment-induced density stratification will be further analyzed through mean turbulent and viscous shear stress profiles.

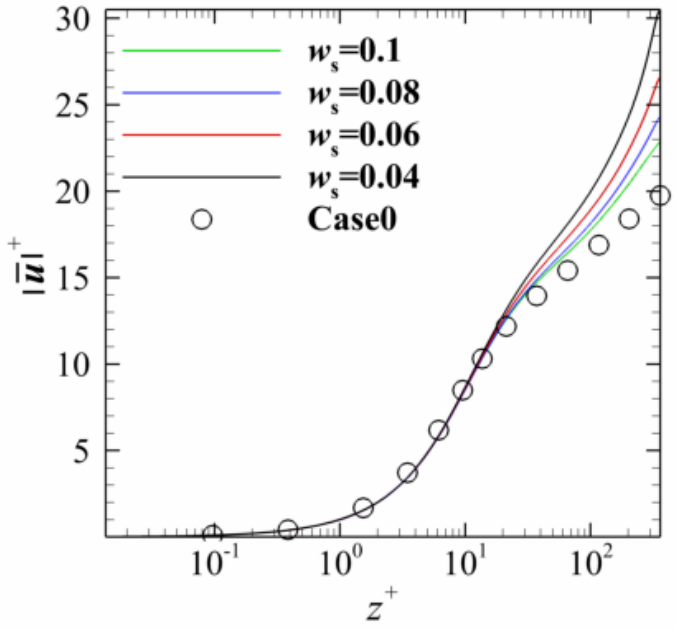

Figure 3.6. Semi-log plots of the mean velocity magnitude, $|\overline{\boldsymbol{u}}|^+$, profiles for Cases 3 to 6 in wall units. Case 0 is plotted as a reference in hollow circle symbols.

3.3.3. MEAN TURBULENT AND VISCOUS SHEAR STRESS PROFILES

The role of sediment settling velocity and thus the sediment suspension on the fluctuating velocity components is assessed through mean turbulent shear stress profiles along the bed-normal direction. Figure 7 plots the Reynolds and viscous shear stress profiles for Cases 3 to 6, all of which are normalized by u_τ^2. Shown in Fig. 7(a, c), the total shear stress in the streamwise direction

linearly decreases in the bed-normal direction, which can be inferred from the integral of the mean momentum equation in the x-direction:

$$\frac{1}{Re_{\tau o}}\frac{\mathrm{d}\overline{u}}{\mathrm{d}z} - \overline{u'w'} = 1 - z. \tag{27}$$

The contribution of each stress term is modulated by the density stratification as a result of changing w_s. The slight decrease in the Reynolds shear stress profiles with decreasing w_s is balanced by an increase in the viscous shear stress, which leads to an increase in the bed-normal velocity gradient. On the other hand, the total shear stress in the spanwise direction changes with respect to the integral of the sediment concentration from the bed, which can be inferred from the bed-normal integration of the mean momentum equation in the y-direction:

$$\frac{1}{Re_{\tau o}}\frac{\mathrm{d}\overline{v}}{\mathrm{d}z} - \overline{v'w'} = \frac{\langle\langle c\rangle\rangle}{Fr_{\tau o}^2}\sin\theta\left(1 - \int_{\xi=0}^{\xi=z}\overline{c}(\xi)d\xi\right). \tag{28}$$

Thus, decreasing settling velocity leads to an increase in the total suspended sediment concentration, which increases both the spanwise Reynolds and viscous shear stresses in magnitude.

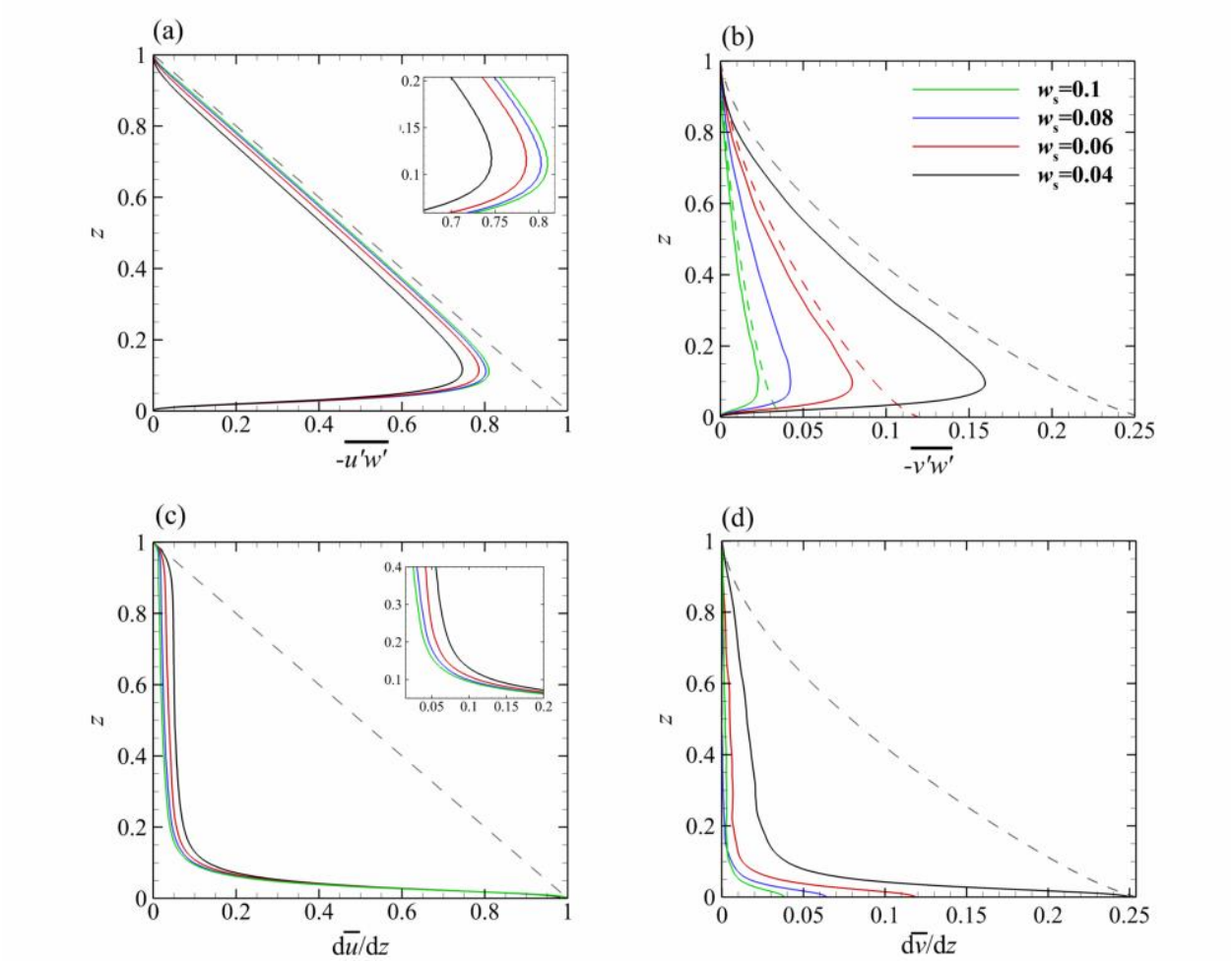

Figure 3.7. The Reynolds shear stress profiles in the (a) streamwise and (b) spanwise directions for Cases 3 to 6. Viscous shear stress profiles in the (c) streamwise and (d) spanwise directions for Cases 3 to 6. The zoomed-in profiles of the Reynolds and the viscous shear stresses in the streamwise direction are plotted as insets in the right corner of subfigures (a) and (c), respectively. The Reynolds and the viscous shear stress profiles shown are normalized by u_τ^2. The black dashed curve in each subfigure represents the total shear stress variation.

Both the Reynolds and viscous shear stresses provide information on the turbulence production, as turbulence production is the product of the mean shear and the Reynolds shear stresses. Given that the flow is two-directional, turbulence production added by the spanwise turbidity current must be assessed. It would be especially convenient if the added turbulence could be quantified as a function of the turbulence production due to the streamwise flow. In this regard, the bed-normal variation of both the mean shear stress and the Reynolds shear stress induced by the spanwise flow relative to those created by the streamwise flow is analyzed. Such analysis will

help assess if such quantification is possible. The directional change of the mean shear and the Reynolds shear stresses in the bed-normal direction is analyzed through their hodographs given in Fig. 8. Dashed lines in Fig. 8(a) and Fig. 8(b) refer to $d\overline{v}/dz = (\langle\langle c\rangle\rangle Fr_{\tau o}^{-2})\, d\overline{u}/dz$ and $\overline{v'w'} = \left(\langle\langle c\rangle\rangle Fr_{\tau o}^{-2}\right)\overline{u'w'}$, respectively. The dashed lines mentioned are used as references to assess the deviation of the stress terms from the principal direction of the bed shear stress. Note in Fig. 8(a) that the rightmost ends of the curves correspond to the top boundary and the leftmost ends of the curves mark the bottom boundary. One can observe from Fig. 8(a) that the mean spanwise shear falls onto $d\overline{v}/dz = (\langle\langle c\rangle\rangle Fr_{\tau o}^{-2})\, d\overline{u}/dz$ except for Case 3, where a deviation above $z = 0.5$ is observed. In Fig. 8(b), each of the Reynolds shear stress hodographs starts from zero, increases quasi-linearly until a peak (upper limb), and then decreases back to zero (lower limb). The difference in the curvature of the upper and the lower limbs becomes emphasized with decreasing settling velocity especially above the peak; however, this difference is of minor importance for turbulence production because the turbulence production is mostly bounded between the peak $-\overline{v'w'}$, *i.e.*, $z \approx 0.1$, and the bed. Below $z \approx 0.1$, both $d\overline{v}/dz$ and $-\overline{v'w'}$ are reasonably well scaled with $d\overline{u}/dz$ and $-\overline{u'w'}$, respectively. This suggests the possibility of quantifying the spanwise production as the scaled streamwise production, which we will further analyze in the next subsection.

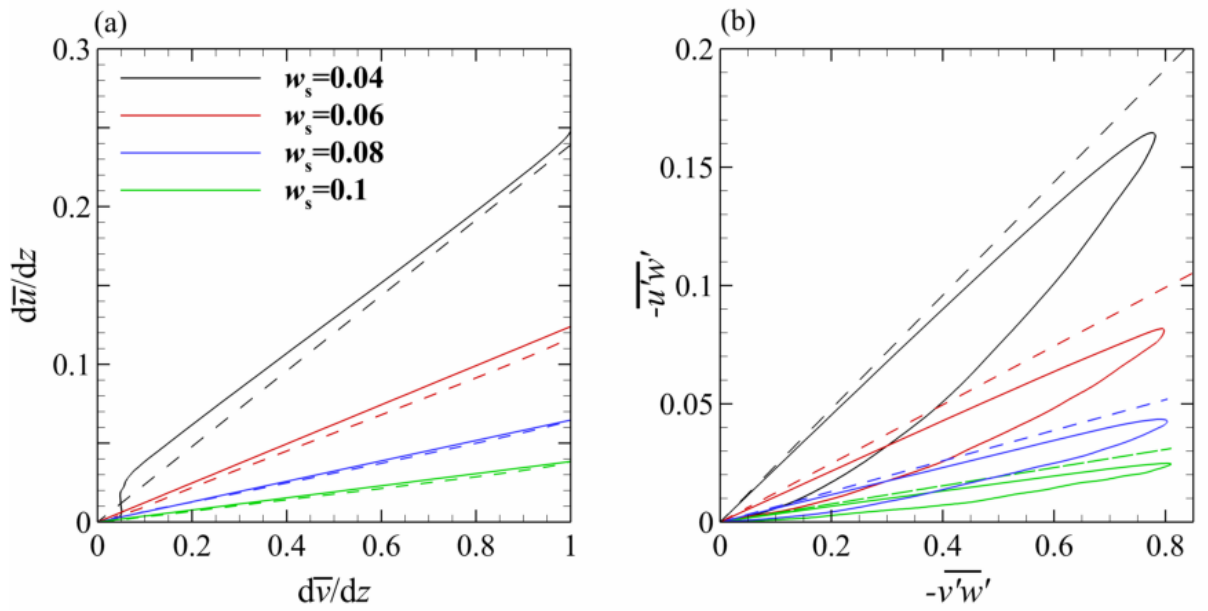

Figure 3.8. Hodographs of the (a) viscous shear stress, *i.e.*, $d\overline{v}/dz$ against $d\overline{u}/dz$, and (b) Reynolds shear stress, *i.e.*, $-\overline{v'w'}$ against $-\overline{u'w'}$, for Cases 3 to 6. The dashed lines correspond to $d\overline{v}/dz = (\langle\langle c\rangle\rangle Fr_{\tau o}^{-2})\, d\overline{u}/dz$ and $-\overline{v'w'} = -(\langle\langle c\rangle\rangle Fr_{\tau o}^{-2})\, \overline{u'w'}$ in subfigures (a) and (b), respectively.

3.3.4. ROLE OF SETTLING VELOCITY ON TURBULENCE MODULATION

Increasing suspended sediment concentration has both augmentative and inhibitive effects on turbulence through stronger spanwise current and sediment-induced stable density stratification, respectively. The Richardson number is a measure of turbulence destruction due to stable density stratification relative to the turbulence production. Therefore, one may expect that the Richardson number will provide further information on turbulence modulation. Simulation results herein allow us to directly compute both the buoyancy destruction and the shear production of turbulence. Therefore, as a first step, we will analyze the role of stable density stratification via the profiles of the flux Richardson number, Ri_f, which is given as

$$Ri_f = -\frac{\varepsilon^{(b)} - P^{(b)}}{P_x^{(s)} + P_y^{(s)}}, \tag{29a}$$

$$\varepsilon^{(b)} = -Fr_{\tau o}^{-2}\overline{c'w'}\cos\theta, \tag{29b}$$

$$P^{(b)} = Fr_{\tau o}^{-2}\overline{c'v'}\sin\theta, \tag{29c}$$

$$P_x^{(s)} = -\overline{u'w'}\frac{\mathrm{d}\overline{u}}{\mathrm{d}z}, \tag{29d}$$

and

$$P_y^{(s)} = -\overline{v'w'}\frac{\mathrm{d}\overline{v}}{\mathrm{d}z}\,. \tag{29e}$$

In Equation (29), $\varepsilon^{(b)}$ and $P^{(b)}$ are the buoyancy destruction and production terms, respectively. In the same equation, $P_x^{(s)}$ and $P_y^{(s)}$ are, respectively, the shear production due to the streamwise and spanwise flows. Figure 9(a) plots Ri_f profiles for Cases 3 to 6. Starting from the bed up to $z \approx 0.8$, the decrease in Ri_f with increasing w_s suggests weakening stable density stratification due to limited sediment suspension from the bed. Alternatively, the magnitude of buoyancy destruction relative to the shear production can be evaluated via the global flux Richardson number, $Ri_{f,g}$ (Ozdemir and Yu, 2018). The global flux Richardson number is similar to that in Equation (29a), but the volume-averaged (or global) values of the production and the dissipation terms in Equation (29b-e) are used instead:

$$Ri_{f,g} = -\frac{\langle\langle \varepsilon^{(b)} \rangle\rangle - \langle\langle P^{(b)} \rangle\rangle}{\langle\langle P_x^{(s)} \rangle\rangle + \langle\langle P_y^{(s)} \rangle\rangle}. \tag{30}$$

Variation of $Ri_{f,g}$ in Fig. 9(b) with respect to w_s draws a similar picture to what was observed from Ri_f profiles. The global flux Richardson number, $Ri_{f,g}$, increases with decreasing w_s. This observation suggests that the rate of increase in the density stratification due to more sediment suspension exceeds that due to decreasing w_s itself from $w_s = 0.10$ to $w_s = 0.04$. Another notable observation from Fig. 9(b) is that $Ri_{f,g} = 0.059$ for $w_s = 0.04$. The observed value of $Ri_{f,g}$ is within the threshold range, $0.058 \leq Ri_{f,g} \leq 0.066$, past which the flow becomes laminar due to stable density stratification (Ozdemir and Yu, 2018). This observation suggests that the flow in Case 3 ($w_s = 0.04$) is close to being critically stratified.

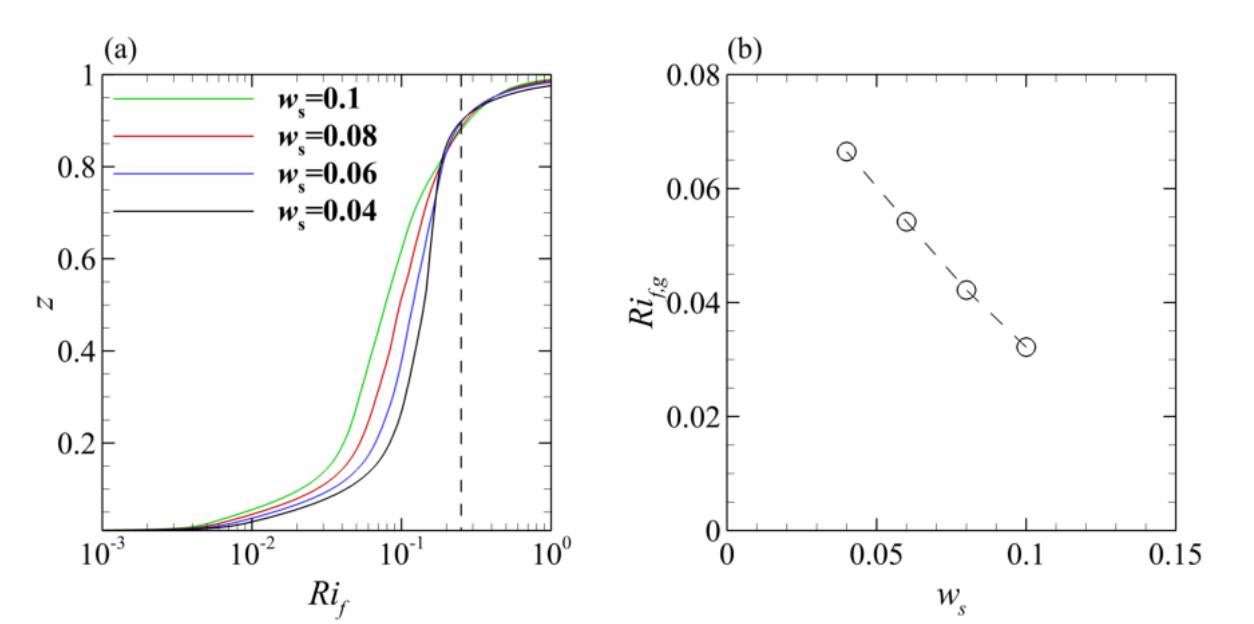

Figure 3.9. (a) Flux Richardson number, Ri_f, profiles of Cases 3 to 6. The black dashed line corresponds to the critical Richardson number, $Ri_{f,cr} = 0.25$, which is the theoretical threshold of stable conditions in a stratified medium. (b) The variation of global flux Richardson number, $Ri_{f,g}$, with respect to settling velocity, w_s (See Equation (31) for its definition).

Strengthening stable density stratification with decreasing sediment settling velocity was also observed from the mean velocity profiles and the profiles of the second-order statistics. In that regard, both the profiles of Ri_f and the variation of $Ri_{f,g}$ with respect to w_s add limited information to what was presented previously. Especially, how a small decrement in w_s (*i.e.*, from $w_s = 0.04$ to $w_s = 0.02$) switches the critically stratified ACSTC to a turbidity current either in auto-suspension or self-accelerating modes cannot be explained by the profiles of Ri_f and the variation of $Ri_{f,g}$ with respect to w_s. However, the variation of each term in $Ri_{f,g}$, *i.e.*, $\langle\langle \varepsilon^{(b)} \rangle\rangle$, $\langle\langle P^{(b)} \rangle\rangle$, $\langle\langle P_x^{(s)} \rangle\rangle$, and $\langle\langle P_y^{(s)} \rangle\rangle$, may provide further information on the aforementioned switch in the spanwise current characteristics. As was also shown in Ozdemir and Yu (2018), the amount of suspended sediment concentration has a limited effect on $\langle\langle P_x^{(s)} \rangle\rangle$. Considering that $\langle\langle P^{(b)} \rangle\rangle$ is an order of magnitude smaller than $\langle\langle \varepsilon^{(b)} \rangle\rangle$ and can be neglected, the rate of change in $\langle\langle P_y^{(s)} \rangle\rangle$ and $\langle\langle \varepsilon^{(b)} \rangle\rangle$ with respect to w_s will possibly provide clues on why the aforementioned switch occurred.

Conceivably, for this switch to occur, the rate of growth in $\langle\langle P_y^{(s)}\rangle\rangle$ with respect to w_s must be substantially larger than that of $\langle\langle \varepsilon^{(b)}\rangle\rangle$. To this end, it is useful to analyze the rate of change in both $\langle\langle P_y^{(s)}\rangle\rangle$ and $\langle\langle \varepsilon^{(b)}\rangle\rangle$ with respect to w_s.

In Ozdemir and Yu (2018), while $\langle\langle \varepsilon^{(b)}\rangle\rangle$ was found to be a function of both $\langle\langle c\rangle\rangle$ and w_s, $\langle\langle P_y^{(s)}\rangle\rangle$ is obtained as a quadratic function of $\langle\langle c\rangle\rangle$. Referring to Section 3.3.2, it was observed that $\langle\langle c\rangle\rangle \propto w_s^{-1.9}$. Therefore, one can obtain relations for both $\langle\langle \varepsilon^{(b)}\rangle\rangle$ and $\langle\langle P_y^{(s)}\rangle\rangle$ as a function of w_s only. The dependence of $\langle\langle \varepsilon^{(b)}\rangle\rangle$ on w_s and $\langle\langle c\rangle\rangle$ can be explained through the mean sediment flux budget, which is obtained upon integrating the plane- and time-averaged advection-diffusion equation, *i.e.*, Equation (9):

$$-w_s\overline{c} + \overline{w'c'} = \frac{1}{Re_\tau S_c}\frac{\mathrm{d}\overline{c}}{\mathrm{d}z}. \tag{31}$$

The terms on the left-hand side of Equation (31) are, respectively, the settling and the turbulent suspension fluxes, and the term on the right-hand side finds the diffusive flux. Referring to Fig. 4, the bed-normal gradient of the mean concentration profiles is negligibly small outside the near-bed region, and thus the settling flux is counterbalanced by the turbulent suspension flux, *i.e.*, $\overline{c'w'} = w_s\overline{c}$. As this balance holds for most of the water column, $\langle\langle \varepsilon^{(b)}\rangle\rangle$ becomes approximately proportional to $w_s\langle\langle c\rangle\rangle$, *i.e.*, $\langle\langle \varepsilon^{(b)}\rangle\rangle \propto w_s\langle\langle c\rangle\rangle$, which was also proposed in Winterwerp (2001) and Cantero *et al*. (2012). Since $\langle\langle c\rangle\rangle \propto w_s^{-1.9}$, one can estimate $\langle\langle \varepsilon^{(b)}\rangle\rangle \propto w_s^{-0.9}$. In the case of $\langle\langle P_y^{(s)}\rangle\rangle$, its quadratic dependence on $\langle\langle c\rangle\rangle$ can be realized from the hodographs of the viscous and Reynolds shear stresses. Referring to Fig. 8, both $-\overline{v'w'}$ and $\mathrm{d}\overline{v}/\mathrm{d}z$ can reasonably be well approximated as functions of $-\overline{u'w'}(\langle\langle c\rangle\rangle Fr_{\tau o}^{-2})\sin\theta$ and $\mathrm{d}\overline{u}/\mathrm{d}z\left(\langle\langle c\rangle\rangle Fr_{\tau o}^{-2}\right)\sin\theta$, respectively. Therefore, after plane- and time-averaging, one can estimate $\langle\langle P_y^{(s)}\rangle\rangle = -\overline{v'w'}\,\mathrm{d}\overline{v}/\mathrm{d}z \propto \langle\langle c\rangle\rangle^2$ which suggests $\langle\langle P_y^{(s)}\rangle\rangle \propto w_s^{-3.8}$. As shown in Fig. 10, the variations of $\langle\langle \varepsilon^{(b)}\rangle\rangle$ and $\langle\langle P_y^{(s)}\rangle\rangle$ with respect to w_s well

fit the functions of $w_s^{-0.9}$ and $w_s^{-3.8}$, respectively. The fact that $\langle\langle \varepsilon^{(b)} \rangle\rangle \propto w_s^{-0.9}$ and $\langle\langle P_y^{(s)} \rangle\rangle \propto w_s^{-3.8}$ suggests that the rate of increase in $\langle\langle P_y^{(s)} \rangle\rangle$ is more intense than that of $\langle\langle \varepsilon^{(b)} \rangle\rangle$ with decreasing w_s. For instance, the decrease of settling velocity from $w_s = 0.04$ to $w_s = 0.02$ amplifies $\langle\langle P_y^{(s)} \rangle\rangle$ more than ten times, but it only increases $\langle\langle \varepsilon^{(b)} \rangle\rangle$ less than two times. The given instance illustrates the non-linear variation of the shear production due to the spanwise current as a function of the sediment settling velocity. This also offers an explanation as to why an almost critically stratified ACSTC, *i.e.,* Case 3, transitions to a turbidity current in auto-suspension or self-accelerating modes with a small decrement in settling velocity.

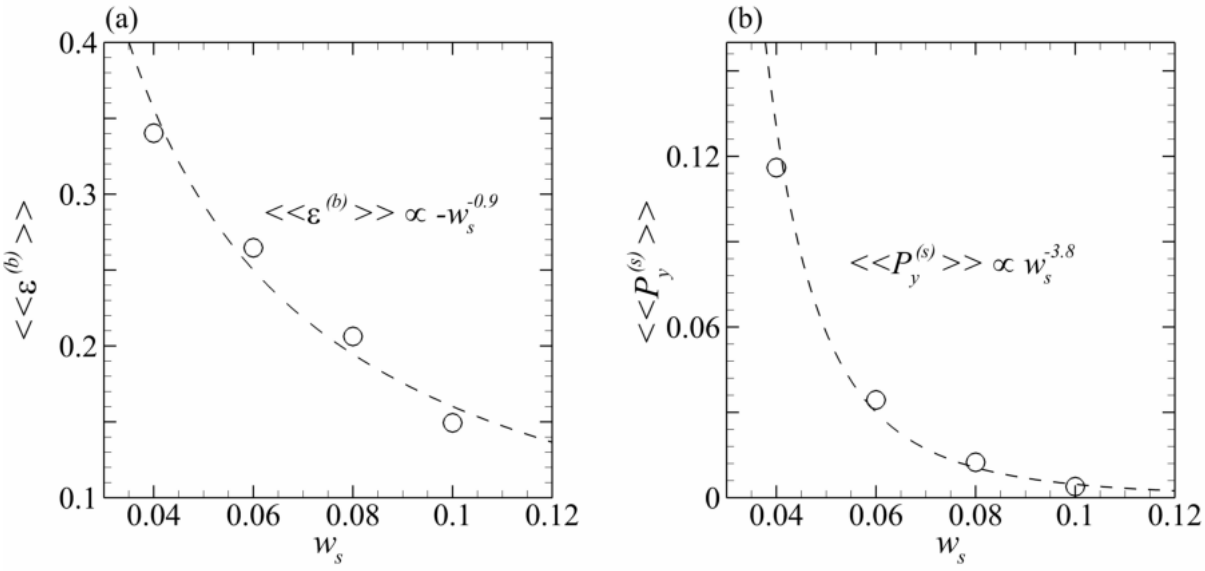

Figure 3.10. Variation of volume-averaged (a) buoyancy dissipation, $\langle\langle \varepsilon^{(b)} \rangle\rangle$, and (b) spanwise production, $\langle\langle P_y^{(s)} \rangle\rangle$, with respect to settling velocity, w_s, for Cases 3 to 6. Best-fitting curves in subfigures (a) and (b) are shown in dashed lines.

3.4. DISCUSSION

3.4.1. PARAMETERIZATION

The only available conceptual model in the literature for WCSTCs is proposed by Wright *et al.* (2001). As the aforementioned model is commonly utilized to interpret most field and some numerical studies on WCSTCs, it is worth to compare the parameters proposed in the conceptual model with those obtained from the simulation results. In the model mentioned, the downslope force created by the suspended sediment-induced density difference is balanced by the shear force at the bed, which is expressed as a modified quadratic relation. This relation translates to the problem posed here as

$$\frac{\langle\langle c\rangle\rangle}{Fr_{\tau o}^2}\sin\theta = C_d\langle\langle v\rangle\rangle|\langle\langle \boldsymbol{u}\rangle\rangle|, \tag{32}$$

where C_d is the drag coefficient. The left-hand side of Equation (32) finds the stress due to density difference created by the sediment suspension, and the right-hand side is the shear stress at the bed. Note from Equation (32) that the modified form of the drag force relation accounts for the cross-shelf current's effect on the bed shear stress. The conceptual model proposed by Wright *et al.* (2001) postulates a value range for the drag coefficient, *i.e.*, $C_d \sim 0.003 - 0.005$, based on the experimental study by Van Kessel and Kranenburg (1996), where C_d is evaluated from the flume experiments of unidirectional mud-laden flows. As will be shown, the values observed in our study falls even below the lower limit of the given range. As an alternative, we sought relations for C_d estimates by linking Equation (32) to the friction coefficient relation for steady turbulent flows. It should be noted that our analysis is restricted to only ACSTCs and it is not valid when waves are present. First, let us consider that the total bed shear stress can be evaluated as

$$\tilde{\tau}_b = \frac{1}{2}\tilde{\rho}_f C_f|\langle\langle \tilde{\boldsymbol{u}}\rangle\rangle|^2, \tag{33a}$$

$$\tau_b = \frac{1}{2} C_f |\langle\langle \boldsymbol{u} \rangle\rangle|^2, \tag{33b}$$

where C_f is the friction coefficient. In this section, the drag and friction coefficients obtained from Equation (32) and Equation (33) by using the simulation results will be referred to as observed drag and friction coefficients, respectively. If the scaling factor between $\langle\langle u \rangle\rangle$ and $\langle\langle v \rangle\rangle$ is the same as that between the bed shear stresses created by the spanwise and the streamwise flows, *i.e.*, $\langle\langle v \rangle\rangle / \langle\langle u \rangle\rangle = \left(\langle\langle c \rangle\rangle Fr_{\tau o}^{-2} \sin\theta\right)/u_{\tau o}^2$, Equation (32) and Equation (33) find $C_d = C_f/2$. Before comparing the observed and the estimated drag coefficients, we first compare $\langle\langle v \rangle\rangle / \langle\langle u \rangle\rangle$ and $\left(\langle\langle c \rangle\rangle Fr_{\tau o}^{-2} \sin\theta\right)/u_{\tau o}^2$ in Fig. 11(a) to check the validity of our assumption. Deviation of $\langle\langle v \rangle\rangle / \langle\langle u \rangle\rangle$ from $\left(\langle\langle c \rangle\rangle Fr_{\tau o}^{-2} \sin\theta\right)/u_{\tau o}^2$ is minimal for $w_s = 0.10$ but becomes discerned when $w_s = 0.04$. We further compared C_d with the estimated $C_f/2$ in Fig. 11(b), where estimated C_f is obtained from the relation proposed by Blasius (1913):

$$C_f = 0.079 (Re)^{-\frac{1}{4}}. \tag{34}$$

In Equation (34), $Re = |\langle\langle \tilde{\boldsymbol{u}} \rangle\rangle| \tilde{h} / \tilde{\nu}_f$. To make a firmer conclusion, we also used the data of Ozdemir and Yu (2018) for $w_s \geq 0.04$ in addition to the simulation results herein. There is an obvious deviation of observed C_d from the estimated $C_f/2$ with increasing sediment concentration. One may attribute the observed deviation to the departure of $\langle\langle v \rangle\rangle / \langle\langle u \rangle\rangle$ from $\left(\langle\langle c \rangle\rangle Fr_{\tau o}^{-2} \sin\theta\right)/u_{\tau o}^2$; however, the difference between the observed C_d and the estimated $C_f/2$ appears to be more intense than that between $\langle\langle v \rangle\rangle / \langle\langle u \rangle\rangle$ and $\left(\langle\langle c \rangle\rangle Fr_{\tau o}^{-2} \sin\theta\right)/u_{\tau o}^2$. Therefore, in Fig. 11(d), we further compare the observed and the estimated $C_f/2$ obtained from Equation (33) and Equation (34), respectively. Also, observed C_d and $C_f/2$, which are obtained from Equation (32) and Equation (34), are also compared in Fig. 11(c). Observed C_d well compares with the observed $C_f/2$, and the variation of the estimated $C_f/2$ with respect to the observed $C_f/2$ is similar

to that between the observed C_d and the estimated $C_f/2$. These observations suggest that the slight disagreement between $\langle\langle v\rangle\rangle/\langle\langle u\rangle\rangle$ and $\left(\langle\langle c\rangle\rangle Fr_{\tau o}^{-2}\sin\theta\right)/u_{\tau o}^2$ is not the primary reason for the deviation of C_d from $C_f/2$ estimated by Equation (35); instead, it is conjectured that C_f reduces due to the increasing level of stable density stratification. Therefore, Equation (34), which is suggested for steady non-stratified flows, cannot account for the density stratification. The agreement between the observed C_d and $C_f/2$ not only supports the above-mentioned conjecture but also suggests that C_d can be estimated by C_f that is modulated by the density stratification in a stably stratified channel flow. Given that in Wright *et al*. (2001), $\langle\langle c\rangle\rangle$ is included in the bulk Richardson number, $Ri_b = \langle\langle c\rangle\rangle(Fr_{\tau o}|\boldsymbol{u}|)^{-2}$, it is possible to estimate C_f, and thus C_d, as a function of Re and Ri_b. To the best of our knowledge, such relation does not exist in the literature, even for stably stratified unidirectional steady channel flows. Its estimation is not possible with the results herein due to the limited number of simulations conducted. Further study is to establish a relation for the drag coefficient as a function of Re and Ri_b will be discussed in Chapter 4.

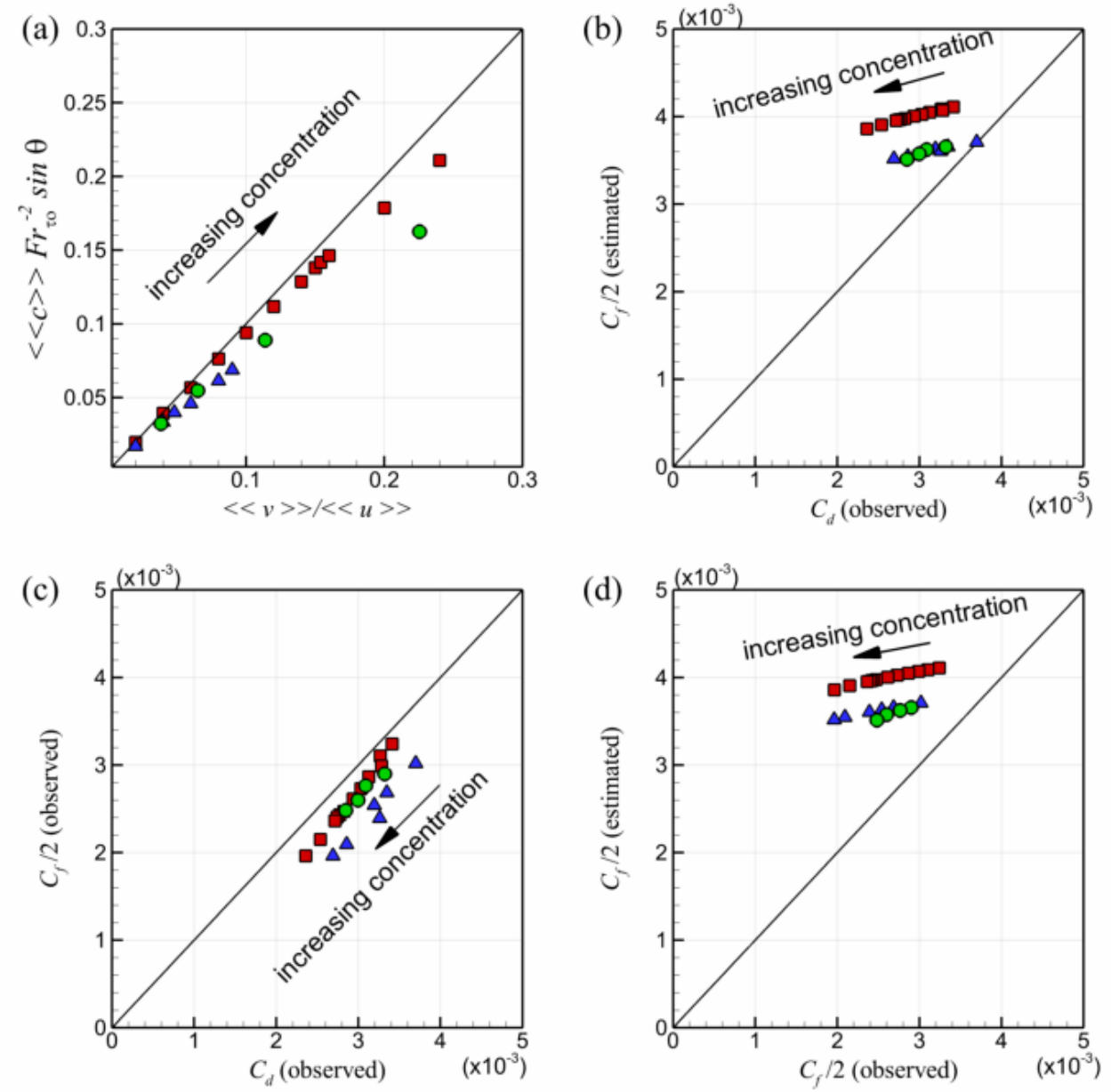

Figure 3.11. (a) Comparison of $\langle\langle v\rangle\rangle/\langle\langle u\rangle\rangle$ with $\langle\langle c\rangle\rangle Fr_{\tau o}^{-2}\sin\theta$. (b) Comparison of observed drag coefficient, C_d, with the half of the estimated friction coefficient, $C_f/2$, obtained from Equation (34). (c) Comparison of observed C_d with observed $C_f/2$. (d) Comparison of observed $C_f/2$ with estimated $C_f/2$. Red squares and blue triangles correspond to the cases with $w_s = 0.04$ and $w_s = 0.1$ in Ozdemir and Yu (2018), respectively. Green circles correspond to the Cases 3-6 in this study. Solid line in each subfigure is a 1:1 line to compare the variables in x- and y-axes. Arrows in each subfigure indicate the variation of the variables with increasing concentration.

3.4.2. COMPARISON WITH PREVIOUS STUDIES

Within a vast literature of turbidity currents, the study by Parker *et al*. (1986) provides insights similar to the findings of the present study, although Parker *et al*. (1986) focused on classical

turbidity currents. The results of Parker *et al.* (1986) suggest that if the rate of turbulence dissipation exceeds the rate of turbulence production, the turbulence will eventually collapse, and the turbidity current will annihilate. Otherwise, sediment entrainment would exceed the sediment deposition, and the flow would eventually result in a self-accelerating turbidity current. To investigate the parametric limits of the self-accelerating and annihilated turbidity currents, Parker *et al*. (1986) adopted three- and four-equation models. While the former results in physically inconsistent results, due to neglecting the turbulent kinetic energy balance, the latter was successful to provide realistic results. In this study, the problem formulation is similar to that in Parker *et al*. (1986); however, instead of using four-equation models, the possibility of transition from ACSTCs to auto-suspending or self-accelerating turbidity currents is investigated via DNS. Since DNS resolves turbulence, its use eliminates the need to close the turbulent kinetic energy balance equation, which adopts parameterization. Perhaps more important, we were able to quantify the total sediment suspension, turbulence production, and buoyancy destruction as functions of the sediment settling velocity. Note that such quantification is tightly linked to the shape of the bed-normal profiles of these variables. In Parker *et al*. (1986), the shape of these variables' bed-normal profile is accounted for in the "shape factor" (cf. Equation (A.36) in Parker *et al*., 1986). Due to the lack of experimental data, Parker *et al*. (1986) assumed a uniform distribution for all the variables mentioned following Pantin (1979). As mentioned in Section 3.3.2, settling velocity, relative to turbulence intensity, governs the concentration profiles. The "shape factor" must, therefore, depend on the settling velocity. In a way, the simulations conducted herein tested the validity of this argument. We were able to obtain relations for total sediment concentration, turbulence production, and buoyancy destruction as a function of the settling velocity. Hence, we

were able to conveniently assess the competition between the turbulence production and buoyant destruction and thus the transition to auto-suspending or self-accelerating turbidity currents.

Another noteworthy difference between this study and Parker *et al*. (1986) is the erosion flux formula adopted. The erosion formula used in Parker *et al*. (1986) is suitable for relatively coarse sediments, *i.e.,* $\tilde{d} = 60{\sim}1000\ \mu m$ (Akiyama and Fukushima, 1985). If one uses the erosion formula proposed by Akiyama and Fukushima (1985) for the sediment size range we selected, a constant but substantially larger erosion flux would be added to the flow in our simulations. It should be mentioned that there is no unified relation in the literature for sediment erosion from the bed. This constitutes a major source of limitation not only to this study but also to any study that needs to consider erosion from the bed.

Parametric limits that delineate ACSTCs from auto-suspending or self-accelerating turbidity currents were also discussed in Wright *et al*. (2001), although only auto-suspending turbidity currents were mentioned. The aforementioned parametric limits were determined based on the conceptual model proposed by Wright *et al*. (2001), which was discussed in Section 3.4.1. When an auto-suspending or self-accelerating turbidity current grows out of an ACSTC, the spanwise velocity far exceeds its streamwise counterpart, $v \gg u$, which leads to $|\boldsymbol{u}| \approx v$. Thus, Equation (32) will reduce to

$$\frac{\langle\langle c\rangle\rangle}{Fr_{\tau o}^2}\sin\theta = C_d\langle\langle v\rangle\rangle^2. \tag{35}$$

Wright *et al.* (2001) also defined a bulk Richardson number, which translates to our problem as $Ri_b = \langle\langle c\rangle\rangle(Fr_{\tau o}|\boldsymbol{u}|)^{-2}$. Thus, Equation (35) further reduces to

$$\sin\theta = C_d Ri_b. \tag{36}$$

Wright *et al*. (2001) argued that erosion and deposition are governed by the sediment-induced density stratification. It was argued that if there is excess sediment suspension exceeding the

critically stratified conditions, it must settle. Similarly, if the flow is below the critically stratified conditions, suspended sediment deficit must be compensated by the erosion from the bed. The critically stratified condition was quantified by the bulk Richardson number (Ri_b), and it was argued that the critically stratified flow must satisfy $Ri_b = 0.25$. In the same study, it was also assumed that a proper value for the drag coefficient is $C_d = 0.003$. Once these values are substituted in Equation (36), the critical slope was obtained as $\sin\theta = 0.012$. It was proposed that above the critical slope, WCSTCs become auto-suspending turbidity currents. In our simulations, we observed that auto-suspending or self-accelerating turbidity currents occur even when $\sin\theta = 0.01$. Perhaps, the reason is that the assumptions made by Wright *et al*. (2001) are too strong. For example, in our simulations $Ri_b \ll 0.25$ even for $w_s = 0.04$ (See Fig. 12). In addition, the maximum drag coefficient observed is slightly lower than $C_d = 0.003$, which reduces with increasing Ri_b and is a function of Re_τ. Perhaps more important, sediment erosion from the bed or deposition to the bed is not necessarily governed by the sediment-induced density stratification.

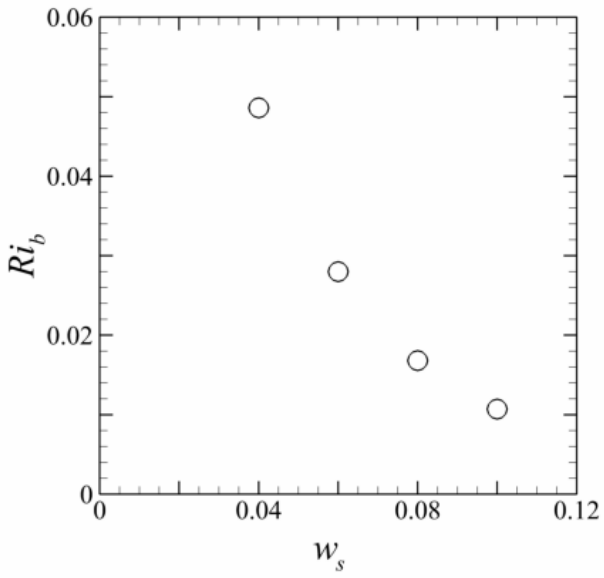

Figure 3.12. Variation of bulk Richardson number, Ri_b, with respect to settling velocity, w_s.

3.5. SUMMARY AND CONCLUSIONS

This chapter investigated the role of sediment settling velocity on the dynamics of ACSTCs, where sediments are sourced from the ephemeral fine sediment deposits. Direct numerical simulations were conducted for a steady, fully developed, turbulent, fine particle-laden channel flow with a mild spanwise slope. Sediment suspension is allowed through sediment mass exchange at the bed. In the problem posed, sediment settling velocity plays a key role in turbulent characteristics of ACSTCs such that increasing settling velocity results in decreasing sediment concentration and hence: (i) diminished turbulence production created by the spanwise turbidity current and (ii) less pronounced stable density stratification created by the sediment suspension. On the other hand, for a given or fixed sediment concentration, sediment settling velocity enhances density stratification. By specifying various sediment settling velocity, the given competing processes were primarily investigated.

The results suggest that sediment settling velocity imposes control on sediment suspension, where volume-averaged suspended sediment concentration is non-linearly related to the inverse of the sediment settling velocity, *i.e.*, $\langle\langle c \rangle\rangle \propto {w_s}^{-1.9}$. Thus, decreasing settling velocity results in higher suspended sediment concentration, which leads to higher spanwise velocity. In addition, the increase in suspended sediment concentration creates enhanced density stratification, which increases the turbulence destruction as the sediment settling velocity reduces from $w_s = 0.1$ to $w_s = 0.04$.

In the conducted simulations, spanwise flow is driven by the density difference due to sediment suspension, while the streamwise flow is driven by a uniform pressure gradient. Dependence of the spanwise flow on non-uniform sediment concentration leads to the directional variation of the mean flow along the bed-normal direction. Thus, enhanced density difference due to decreasing

w_s –or increasing $\langle\langle c\rangle\rangle$– leads to a more pronounced directional variation of the mean flow along the bed-normal direction, especially towards the top boundary. However, the observed directional variation has minimal impact on turbulence production. Both the spanwise Reynolds shear stress and the bed-normal gradient of the spanwise velocity can be well approximated by their streamwise counterparts after scaling by $\langle\langle c\rangle\rangle Fr_{\tau o}^{-2} \sin\theta$. Therefore, turbulence production can be quantified as a quadratic function of the total sediment concentration. As $\langle\langle c\rangle\rangle \propto w_s^{-1.9}$, depth-averaged turbulence production becomes proportional to $w_s^{-3.8}$, which is also realized from the simulation results.

The simulation results also suggest the existence of a critical settling velocity below which the spanwise turbidity current switches its mode from the ACSTC to a self-driven turbidity current. As such, the spanwise turbidity current reaches a self-driven stage without the necessity to keep itself in motion by any external force. The continuous increase of $\langle\langle c\rangle\rangle$, $\langle\langle v\rangle\rangle$, and $\langle\tau_b\rangle/\tau_{bo}$ in time for $w_s < 0.04$, while the rest of the simulated cases reach stationarity in time, suggests the possibility of the spanwise current's reaching the auto-suspension or self-accelerating modes for $w_s < 0.04$, where near-bed turbulence leads to continually increasing erosion from the bed. For $w_s < 0.04$ at $Re_{\tau o} = 360$, the spanwise production non-linearly increases with decreasing settling velocity, *i.e.*, $\langle\langle P_y^{(s)}\rangle\rangle \propto w_s^{-3.8}$, and overcomes the turbulence dissipation due to stable density stratification, whose rate of change with decreasing settling velocity is far lower, *i.e.*, $\langle\langle \varepsilon^{(b)}\rangle\rangle \propto w_s^{-0.9}$. This offers an explanation as to why the spanwise turbidity current switches its mode from the ACSTC to a turbidity current in auto-suspension mode with a small decrement in w_s. Thus, for the selected turbulence level herein, *i.e.*, $Re_{\tau o} = 360$, and the selected erosion parameters, *i.e.*, $\tau_c = 0.9$ and $m_e(1-\phi) = 1 \times 10^{-4}$, the critical settling velocity delineating the ACSTC from a turbidity current in auto-suspension mode is conjectured to lie within $0.02 \leq w_s < 0.04$. Further

simulations within $0.02 < w_s < 0.04$ are needed to define the exact critical settling velocity for this transition.

The results obtained are compared with two conceptual models. We first compared our findings with the model proposed by Parker *et al*. (1986). The hypothesis that motivated this study was essentially very close; sediment entrainment from the bed accelerates the turbidity current, and the energy consumed by the density stratification acts against such an acceleration. As mentioned in Parker *et al*. (1986), such acceleration is "intimately associated with sediment erosion and deposition." Here, we were able to obtain relations between the suspended sediment amount and the settling velocity when the spanwise turbidity current is an ACSTC. This is because the sediment concentration profiles are associated with the settling velocity. In other words, the shape function of the concentration profile (Parker *et al*., 1986) can be related to the settling velocity. Turbulence production added by the spanwise turbidity current and the buoyancy destruction was also quantified as a function of settling velocity. By evaluating the rate of change in turbulence production and the buoyancy destruction when the spanwise turbidity current is an ACSTC, it was possible to explain the role of the settling velocity to ignite an auto-suspending or self-accelerating turbidity currents.

The second comparison was made with the conceptual model for WCSTCs proposed by Wright *et al*. (2001). We first compared the suggested drag coefficient by Wright *et al*. (2001), which is $C_d = 0.003$. Our results suggested a decreasing C_d for increasing sediment concentration that falls below the suggested value of $C_d = 0.003$. We also sought the possibility of a relationship for the drag coefficient of the ACSTCs. Our results suggest that C_d can be estimated by the friction factor (C_f) of a stably stratified turbulent channel flow, *i.e.*, $C_d = C_f/2$. Our results also suggest that both C_f and C_d reduce with strengthening stable density stratification, which can be quantified by the

bulk Richardson number. Therefore, it is possible to estimate C_d as a function of the Reynolds number, $Re = |\langle\langle \tilde{\boldsymbol{u}} \rangle\rangle|\tilde{h}/\tilde{\nu}_f$, and the bulk Richardson number, $Ri_b = [(s-1)\tilde{g}\tilde{h}\langle\langle c \rangle\rangle]/|\langle\langle \tilde{\boldsymbol{u}} \rangle\rangle|^2$. Further study is needed to establish such a relation.

Another comparison of the results herein with the conceptual model by Wright *et al*. (2001) is the parametric limit that delineates ACSTCs from auto-suspending or self-accelerating turbidity currents. The model mentioned assumed that WCSTCs in general, and thus ACSTCs, move in critically stratified conditions, and the drag coefficient used to quantify the bed shear stress is constant. As discussed in detail in Section 3.4.2, this allowed for the shelf-slope to be the only parameter to delineate ACSTCs and auto-suspending turbidity currents. It was proposed that the slopes steeper than 0.012 will lead to auto-suspending turbidity currents. However, the results herein suggest that an ACSTC may not necessarily be critically stratified, and the drag coefficient decreases with the increasing level of turbulence and the density stratification. As such, we also observed the ignition of self-accelerating or auto-suspending turbidity current below $\sin\theta = 0.012$.

The transition of a WCSTC to a turbidity current in auto-suspension mode, to the best of our knowledge, has not been reported in any field and laboratory experiments except for the observations in Waipoa Shelf (Ma *et al*., 2010). However, the occurrence of the transition in the study mentioned is primarily due to the variation of the shelf-slope. In our simulations, the slope is constant, and the transition is due to excess erosion from the bed, which creates excessive down-slope force. Note that we assume an infinite loose fine sediment source at the bed through the boundary conditions. However, loose fine sediment deposits may not be available, which thus may inhibit the ignition of a turbidity current in auto-suspension mode. In fact, apart from the sediment settling velocity, the parameters that affect the described initiation of self-accelerating and self-

sustaining turbidity currents are dependent on erosion parameters such as the normalized excess shear stress, $(|\boldsymbol{\tau}_b|/\tau_c - 1)$, erosion rate, m_e, porosity, ϕ, and bed slope, $\sin\theta$. Perhaps, a broader parametric study would potentially improve the findings in this study.

4. DIRECT NUMERICAL SIMULATIONS OF MINIATURE ALONG-SHELF CURRENT-SUPPORTED TURBIDITY CURRENTS: IMPLICATIONS TO PARAMETERIZATION AT THE FIELD SCALE

4.1. INTRODUCTION

4.1.1. MOTIVATION

Understanding the processes involved in the dispersal of river-borne sediments in coastal ocean is central to quantifying the budgets of geochemically important particulate matter at the global scale and understanding the dynamics of shelf morphology. Wave- and current-supported turbidity currents (WCSTCs) are one of these processes responsible for particulate matter dispersal in the continental shelf. For WCSTCs to occur, near-bed, or boundary-layer, turbulence generated by waves and along-shelf currents must create and maintain sediment suspension. With sediment suspension maintained by alongshore currents and/or waves, persistent cross-shelf force is generated due to density difference between the sediment suspension and the ambient water over the mild-sloped portions of the shelf. Aided by the force mentioned, suspended sediments can propagate towards the shelf break, which may result in substantial amount of sediment displacement in the shelf (Traykovski *et al*., 2000; 2007; Ogston *et al*., 2008; Ma *et al*., 2008; Flores *et al*., 2018).

Following the discovery of WCSTCs, field observations over the last two to three decades worldwide suggest that WCSTCs are more ubiquitous than they are initially thought (Wright *et al*., 1999; Traykovski *et al*., 2000; Ogston *et al*., 2000; Walsh *et al*., 2004; Martin *et al*., 2008; Fain *et al*., 2007; Traykovski *et al*., 2007; Ma *et al*., 2008; 2010; Hale and Ogston, 2014; Wright and Nittrouer, 1995; Jaramillo *et al*., 2009; Traykovski *et al*., 2015; Zhang *et al*., 2016; Flores *et al*., 2018). However, little is known as to their internal structure in part due to lack of direct measurements of concentration and velocity especially in the early observations. This makes it

hard to distinguish the respective roles of potential physical mechanisms associated with high sediment concentration, such as flocculation, rheology, and hindered settling, as well as those associated with ambient hydrodynamics driven by waves, alongshore currents and the turbidity currents that operate in different directions and intensities. To this end, a reductive approach – by ignoring or simplifying some of the physical processes and thereby reducing the number of parameters – would help understand the respective roles of each process and provide a useful basis towards a holistic understanding of WCSTCs. In this regard, studies on alongshore current-supported turbidity currents (ACSTCs), which are a sub-class of WCSTCs, provide a unique opportunity to understand and parameterize the velocity of the turbidity current and the suspended sediment concentration of the turbidity current with reduced complexity. In fact, ACSTCs were reported to be one of the significant agents of river-borne sediment dispersal in the Gulf of Bohai (Wright *et al*., 1988, 2001) and Waipoa Shelf (Ma *et al*., 2008; 2010).

The cross-shelf sediment flux in ACSTCs is generated by sediments which are kept in suspension by alongshore currents only. Absence of waves in ACSTCs reduces the complexities associated with the wave boundary layer. In addition, observed sediment concentrations, ($< \mathcal{O}(10)\mathrm{kg\ m^{-3}}$), are substantially lower than those in WCSTCs. The given sediment concentration is lower than the threshold concentration that delineates fluid mud from a slurry (Mehta, 2013). Therefore, complexities associated with fluid mud, *i.e.*, flocculation, pronounced rheological stresses, hindered settling, can be ignored. Thus, the dominant mechanism becomes the sediment-induced stable density stratification.

With given simplifications, this study investigates how density stratification enhances the cross-shelf velocity and thus the friction coefficient and the role of sediment settling velocity on

the density stratification and the cross-shelf propagation of ACSTCs by using direct numerical simulations (DNS). In the next subsection, the rationale behind these objectives are elucidated.

4.1.2. BACKGROUND

One of the unique characteristics of WCSTCs is the development of equilibrium conditions. In other words, there is a force balance between the force in the cross-shelf direction, the force created by the density difference between the sediment suspension and ambient water, and the opposing shear force at the bed (Wright *et al*., 2001). Although not verified previously, the presence of equilibrium conditions was confirmed by rigorous analyses of the measurements taken close to the Rhine River mouth (Flores *et al*., 2018). Therefore, steady flow conditions apply for ACSTCs, which makes it relatively easier to quantify SSC and the downslope velocity relative to those in highly transient classical turbidity currents. Under such conditions, and using the reference frame shown in Figure 1, this force balance in the cross-shelf direction is formulated as

$$\mathfrak{B} \sin\theta = \rho_f C_d v (u^2 + v_w^2 + v^2)^{1/2}. \quad (1)$$

Following the studies by Grant and Madsen (1979), Feddersen *et al*. (2000), and Wright *et al*. (2001). In Equation (1), $\mathfrak{B}$ is the force due to density anomaly over a unit area, θ is the angle of downslope gradient, C_d is the drag coefficient, v is the downslope velocity of WCSTC, v_w is the shore-normal wave velocity, and u is the alongshore current velocity. In Equation (1), force due to density anomaly is given as

$$\mathfrak{B} = (s-1) g \rho_f \int_{z=0}^{z=h} c(z)\, dz\,. \quad (2)$$

Here, s is the specific gravity of sediments in suspension, g is the magnitude of the gravitational acceleration, ρ_f is the fluid density, *i.e.*, water, c is the volumetric sediment concentration, z is the

vertical distance from bed, and h is the thickness of the turbidity. In ACSTCs waves are absent and hence $v_w = 0$. It follows that Equation (1) further reduces to

$$\mathfrak{B} \sin\theta = \rho_f C_d v(u^2 + v^2)^{1/2}. \quad (3)$$

The left-hand side of Equation (3) finds the downslope force, and the right-hand side finds the bed shear stress. For known θ and v, it is clear from Equation (3) that the magnitude of the drag coefficient and the total sediment suspension are the two key variables for cross-shelf sediment flux. Therefore, in order to quantify the downslope sediment flux, physical mechanisms that affect the total sediment suspension and the drag coefficient must be identified and their variation with respect to the governing parameters must be formulated. From the force balance in Equation (1), presence of the drag coefficient associated with the bed shear stress clearly shows that WCSTCs including ACSTCs are sediment-laden boundary layer flows. Therefore, one must in part refer to the principals of the boundary-layer theory to infer the parameters that govern the drag coefficient. It is well-known that in turbulent boundary-layer flows, the drag coefficient decreases with the increasing Reynolds number because the boundary layer thickness reduces with increasing turbulent intensity thereby enhancing the depth-averaged velocity. The Reynolds number defined with appropriate length and velocity scales must therefore be one of the parameters that govern the drag coefficient. For fine sediment-laden flows, another mechanism that governs the drag coefficient is the sediment-induced stable density stratification (see for example, Winterwerp *et al*., 2009). Dissipation in turbulence due to density stratification gives rise to an increase in shear and thus the velocity. With velocity increased, the drag coefficient reduces. Variables that govern the density stratification in a sediment laden flow are the mean sediment concentration and the representative sediment settling velocity of the suspension (Winterwerp, 2001; 2009; Cantero *et al*., 2012; Ozdemir *et al*., 2010; 2011). Therefore, one of the objectives herein is to analyze the

effect of various sediment concentration and the sediment settling velocity on the velocity structure of ACSTCs. In doing so, a comprehensive understanding of how C_d is modulated by the density stratification will be possible.

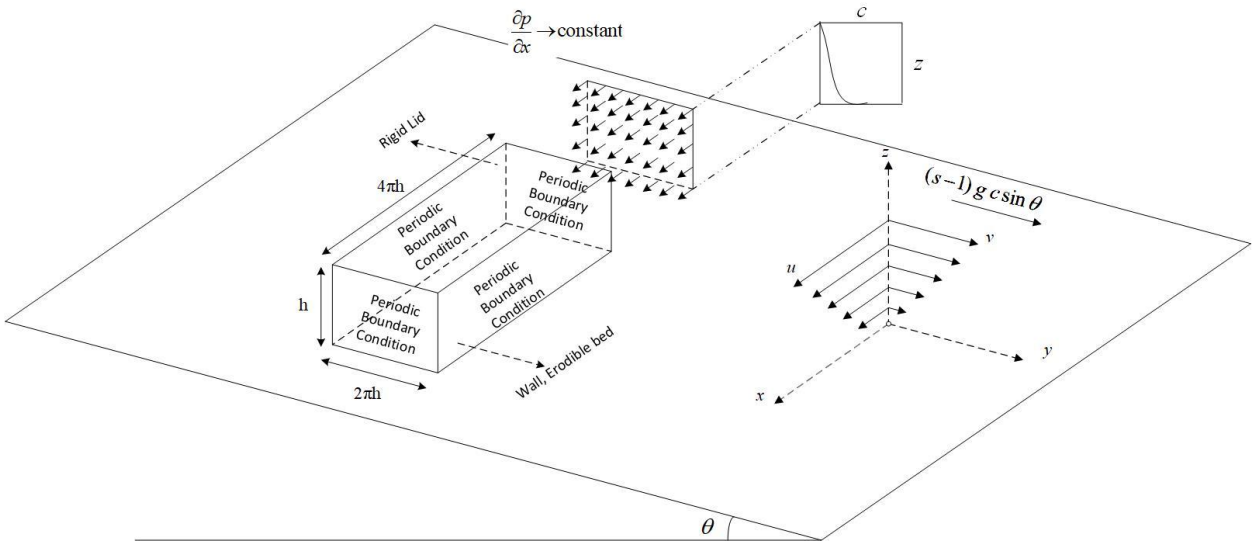

Figure 4.1. Sketch of computational domain with the size of $L_x \times L_y \times L_z = 4\pi h \times 2\pi h \times h$ (not to scale). Periodic boundary conditions are specified in $x - y$ planes for both fluid and sediment phases. For the velocity field, wall boundary condition and rigid lid are specified at the bottom and top boundaries, respectively. The erodible bed is also specified at the bottom boundary. Along-shelf current is mimicked by a mean current driven by the uniform pressure gradient in the x-direction, while the spanwise turbidity current is driven by the spanwise-component of the buoyancy force, $(s-1)gc\,sin\,\theta$, in y-direction due to the bed gradient, θ. The components of the velocity vector in the streamwise and spanwise directions are represented with arrows in x- and y-directions, respectively. A representative concentration profile is also presented at the topmost part of the figure.

The rest of this chapter is organized as in the following. Section 4.2 describes the problem formulations, choice of input parameters for the simulations conducted, the numerical methods used in the simulations, and the notation used in the analyses of the results. Section 4.3 presents the overall results, variation in the drag coefficient and its parameterization. The study is finalized with the summary and conclusions in section 4.4.

4.2. METHODS

4.2.1. PROBLEM DESCRIPTION AND GOVERNING EQUATIONS

To mimic ACSTCs over an erodible bed, we conducted direct numerical simulations on a steady, fine sediment-laden turbulent channel flow over a smooth and erodible bed with mild spanwise slope, *i.e.*, $\sin\theta < 0.012$ (Wright *et al.*, 2001). Following prior studies (Meiburg and Kneller, 2010; Ozdemir *et al*., 2010, 2011), the velocity of the sediment phase, $\boldsymbol{u}^s$, is approximated as the vector sum of the fluid velocity and sediment settling velocity as

$$\boldsymbol{u}^s = \boldsymbol{u}^f + w_s \boldsymbol{e_g}, \tag{4}$$

where $\boldsymbol{u}^f = (u^f,\ v^f,\ w^f)$, with u^f, v^f, and w^f being the velocity components in the streamwise, spanwise, and bed-normal directions, respectively. In Equation (4), w_s is the sediment settling velocity, and $\boldsymbol{e_g} = (\sin\theta\, \boldsymbol{e_y} - \cos\theta\, \boldsymbol{e_z})$ is the unit vector that points in the direction of gravitational acceleration, with $\boldsymbol{e_y}$ and $\boldsymbol{e_z}$ being the unit vectors pointing in the cross-shelf and vertical directions, respectively. The sediment settling velocity in Equation (4) is calculated based on the Stokes law as (Stokes, 1851)

$$w_s = \frac{(s-1)gd^2}{18\nu_f}, \tag{5}$$

where d is the sediment diameter, and ν_f is the kinematic viscosity of the seawater. Sediments are assumed to be spherical and uniform in size, where the sediment diameter ranges as $d \sim 6 \times 10^{-6}$ m $- 19.8 \times 10^{-6}$ m. As it will be clear in the following sections, the volumetric suspended sediment concentration (SSC) is sufficiently dilute for all the cases, *i.e.*, $c < 1\%$ (Cantero *et al*., 2008, 2012). Fine sediment size, along with the dilute suspended sediment concentration, allows us to treat the sediment phase as a continuum. Due to dilute suspended sediment concentration, the fluid phase can also be assumed to satisfy the continuity equation, and

the Boussinesq approximation is adopted for the momentum equation. Therefore, the governing equations for the fluid phase are the continuity and momentum equations which are given as in the following:

$$\boldsymbol{\nabla} \cdot \boldsymbol{u}^f = 0, \tag{6}$$

and

$$\frac{\partial \boldsymbol{u}^f}{\partial t} + \boldsymbol{u}^f \cdot \boldsymbol{\nabla} \boldsymbol{u}^f = -\frac{u_{\tau o}^2}{h} \boldsymbol{e_x} - \frac{\boldsymbol{\nabla} p'}{\rho_f} + (s-1) g c \boldsymbol{e_g} + \nu_f \nabla^2 \boldsymbol{u}^f. \tag{7}$$

In Equations (6) and (7), $u_{\tau o} = (\tau_{b0}/\rho_f)^{1/2}$ is the friction velocity, with τ_{b0} being the bed shear stress for the unidirectional clear fluid case (Case 0 in Table 1). In Equation (7), p' is the dynamic pressure, and c is the volumetric sediment concentration. The first term on the right-hand side of Equation (7) accounts for the mean pressure gradient that drives the along-shelf current. The third term on the right-hand side of the Equation (7) is the buoyancy term and accounts for the coupling between the fluid and sediment phases. While the spanwise component of the buoyancy term, $(s-1) g\, c \sin\theta\, \boldsymbol{e_y}$, drives the cross-shelf propagation of ACSTC, the vertical component of the buoyancy term, $-(s-1) g\, c \cos\theta\, \boldsymbol{e_z}$, also accounts for the sediment-induced stable density stratification.

Sufficiently small sediments allow us to approximate the sediment phase as a continuum. Thus, the governing equation for sediment phase can be given as an advection-diffusion equation (Cantero *et al*., 2008):

$$\frac{\partial c}{\partial t} + \boldsymbol{u}^s \cdot \boldsymbol{\nabla} c = \mathfrak{D}\, \nabla^2 c, \tag{8}$$

where $\mathfrak{D}$ is the diffusivity of the sediment concentration.

4.2.2. COMPUTATIONAL DOMAIN AND BOUNDARY CONDITIONS

The equations are solved in a planar computational channel of the size of $L_x \times L_y \times L_z = 4\pi h \times 2\pi h \times h$ with the number of grid points of $N_x \times N_y \times N_z = 256 \times 128 \times 257$ (See Figure 1). Note that subscripts x, y, and z represent the streamwise (along-shelf), spanwise (cross-shelf), and bed-normal directions, respectively. While equally spaced grid points are used in x- and y-directions, Chebyshev-Gauss-Lobbato collocation points are used for discretization in the bed-normal direction (Canuto *et al.*, 1987). The domain size and grid resolution are specified to capture the essential physical features of ACSTCs, such as the largest and the smallest turbulent scales, while keeping the computational expenses at a reasonable level. The adequacy of the domain size and grid resolution are discussed in Appendix B1 and B2 in chapter 3, and it has been verified to be sufficient to resolve all the turbulent scales.

For both fluid and sediment phases, periodic boundary conditions are specified along the along-shelf and the cross-shelf directions. For the velocity field, no-slip and no-penetration wall boundary condition is imposed at the bottom boundary, *i.e.*, $\boldsymbol{u}^f = 0$. Free-slip and no-penetration boundary condition is also imposed at the top boundary, *i.e.*, $\frac{\partial u^f}{\partial z} = \frac{\partial v^f}{\partial z} = 0$ and $w^f = 0$. For suspended sediments to be sourced from bed erosion, erosional/depositional boundary condition is implemented at the bottom boundary as

$$-\mathfrak{D}\frac{\partial c}{\partial z}\Big|_{z=0} = E - D, \tag{9}$$

where E and D are the erosion and deposition fluxes, respectively. The Partheniades-Ariathurai-type formulation is used to calculate the erosion flux as (Sanford and Maa, 2001):

$$E = \begin{cases} m_e(1-\phi)S & |\boldsymbol{\tau}_b| \geq \tau_c \\ 0 & |\boldsymbol{\tau}_b| < \tau_c \end{cases}, \tag{10}$$

where m_e is the erosion coefficient, ϕ is the porosity of the bed, $S = (|\boldsymbol{\tau}_b|/\tau_c - 1)$ is the normalized excess shear stress with τ_c being the critical shear stress of erosion, and $|\boldsymbol{\tau}_b|$ is the magnitude of the bed shear stress. The bed shear stress is calculated at each time step as:

$$|\boldsymbol{\tau}_b| = \mu_f \left| \frac{\partial \boldsymbol{u}^f}{\partial z} \right|_{z=0}. \tag{11}$$

Here μ_f is the dynamic viscosity of the seawater. The deposition flux is also calculated as (Sanford and Maa, 2001; Winterwerp, 2007):

$$D = w_s c \Big|_{z=0}. \tag{12}$$

Our choice of parameters is further discussed in section 4.2.3.

4.2.3. DESIGN OF NUMERICAL EXPERIMENTS AND SIMULATION PARAMETERS

Its numerical details provided in the following section, the numerical model requires bed slope, domain size, friction velocity, erosion parameters, and sediment settling velocity as input. We conducted 12 simulations for four different settling velocities and three different erosion parameters. A base simulation free of sediments was conducted to obtain the initial conditions. We selected the bed slope as $\sin\theta = 0.01$. Selected bed slope is smaller than the critical slope for ACSTCs to transition to auto-suspending or self-accelerating turbidity current proposed by Wright *et al*. (2001).

Impact of density stratification on turbulence destruction and thus the velocity structure requires accurate resolution of turbulence near the bed. Resolution of turbulence without any assumptions is possible by using DNS. Yet, the scales associated with typical ACSTCs is far beyond the reach of DNS with the current availability of computing power. For example, a typical ACSTC observed in the Gulf of Bohai has velocity ranging from $0.15\ \mathrm{m\ s^{-1}}$ to $0.7\ \mathrm{m\ s^{-1}}$ in $3{\sim}5$ m deep seawater. This makes the range of the Reynolds number approximately $450{,}000$ to

3,500,000, which is almost impossible to simulate with DNS. To make the computational demand affordable, we scaled down the depth of ACSTC to 0.1 m, while keeping the friction velocity close to that of the least energetic ACSTC in the Gulf of Bohai, $u_{\tau o} = 3.6 \times 10^{-3}$ m s^{-1}. Our estimate here is based on a logarithmic velocity profile, where the surface velocity allows for a back calculation of the friction velocity. For this setup, the Reynolds number ranges from 1.5×10^4 to 7×10^4, and hence does not satisfy the Reynolds number similarity. However, at this range of the Reynolds number, the flow shows the main features of developed turbulence as will be shown in Section 3. Despite its shortcoming due to its miniature scale, the results obtained from this setup provide significant insights, when combined with the available theory of sediment transport and boundary-layers, as to the parameterization of ACSTCs.

For sediment erosion from the bed, we assumed a homogenous bed where bed sediment properties, *i.e.*, τ_c, m_e, and ϕ remain constant, *i.e.*, unlimited (Type II) erosion (Sanford and Maa, 2001). The selected friction velocity is low and gives a bed shear stress of $\tau_{bo} = \rho_w u_{\tau o}^2 \approx 0.013$ Pa. For this level of bed shear stress, ACSTC can be created by eroding loose sediment deposits. Therefore, we selected the critical bed shear stress $\tau_c = 0.01\ Pa$ which is based on the study by Curran *et al.* (2007), where the bottom shear stress as low as $0.01\ Pa$ is sufficient to suspend a loose fine sediment. As mentioned previously, the relation between the erosion coefficient and the ratio between the bed shear stress and critical shear stress of erosion determines the erosion flux from the bed, *i.e.*, $m_e \phi\ S_o$. Thus, any increase (decrease) in the erosion flux from the bed can be interpreted as an increase (decrease) in m_e and ϕ or decrease (increase) in τ_c. For convenience, we assigned τ_c as variable while keeping m_e and ϕ constant. The critical shear stress of erosion is considered within the range of $\tau_c \sim 0.01\ Pa - 0.012\ Pa$ while $m_e(1-\phi) =$

3.6×10^{-7} m s^{-1}. The selected range of τ_c gives initial normalized excess shear stress range of $S_o = 0.05$, 0.11, and 0.25, where S_o is defined as

$$S_o = \frac{\tau_{bo}}{\tau_c} - 1. \tag{13}$$

The reason we denote S_o as initial normalized excess shear stress is that the bed shear stress will be augmented by the cross-shelf propagation of ACSTCs. The augmented bed shear stress depends on the amount of SSC which is not known a priori. Therefore, we denote the excess shear stress when ACSTC reaches the equilibrium conditions as S to differentiate it from S_o. For a complete list of simulation parameters, the reader is referred to Table 1.

To assess the effect of sediment settling velocity on both the density stratification and the equilibrium sediment concentration we specified four different settling velocities that range within $w_s \sim 1.44 \times 10^{-4}$ m s^{-1} $- 3.6 \times 10^{-4}$ m s^{-1} for each critical shear stress for erosion. Selected range for sediment settling velocity corresponds to the sediment size range of $d \sim 13 \times 10^{-6}$ m $- 20 \times 10^{-6}$ m, which is medium to fine silt content that is typical for turbidity currents in general (Meiburg and Kneller, 2010).

A case of unidirectional channel flow without sediments at $Re_{\tau o} = 360$ (Case 0 in Table 1) is used as a reference case in this study. For the remaining cases, the velocity field of the Case 0 at its latest time step is used as the initial condition. To obtain accurate and reliable statistics, we ran the simulations long enough past the stationarity until the turbulent statistics become insensitive to additional data. In all the cases, the spanwise velocity reached the stationarity the latest, and thus it was used to identify the statistical equilibrium.

Table 4.1. List of Case identifier, sediment settling velocity (w_s), sediment diameter (d), critical shear stress for erosion (τ_c), bed shear stress (τ_b), friction velocity (u_τ), depth-averaged cross-shelf velocity ($\langle v \rangle$), and depth-averaged along-shelf velocity. Note that bed shear stress (τ_b), the friction velocity (u_τ) and depth-averaged cross-shelf velocity ($\langle v \rangle$) increases with sediment suspension. The increase in depth-averaged along-shelf velocity is due to strengthening density stratification.

Case I.D.	w_s (m s^{-1})	d (m)	τ_c (Pa)	τ_b (Pa)	u_τ (m s^{-1})	$\langle v \rangle$ (m s^{-1})	$\langle u \rangle$ (m s^{-1})
0	0	0	--	0.01296		0	6.16×10^{-2}
A1	3.60×10^{-4}	20×10^{-6}	0.01	0.01298	0.003602	3.00×10^{-3}	7.07×10^{-2}
A2	2.88×10^{-4}	18×10^{-6}	0.01	0.01301	0.003607	5.25×10^{-3}	7.41×10^{-2}
A3	2.16×10^{-4}	15×10^{-6}	0.01	0.01312	0.003622	10.30×10^{-3}	7.97×10^{-2}
A4	1.44×10^{-4}	13×10^{-6}	0.01	0.01380	0.003715	26.50×10^{-3}	9.01×10^{-2}
B1	3.60×10^{-4}	20×10^{-6}	0.011	0.01297	0.003601	2.22×10^{-3}	6.82×10^{-2}
B2	2.88×10^{-4}	18×10^{-6}	0.011	0.01299	0.003604	3.87×10^{-3}	7.06×10^{-2}
B3	2.16×10^{-4}	15×10^{-6}	0.011	0.01305	0.003613	7.68×10^{-3}	7.44×10^{-2}
B4	1.44×10^{-4}	13×10^{-6}	0.011	0.01342	0.003663	18.50×10^{-3}	8.13×10^{-2}
C1	3.60×10^{-4}	20×10^{-6}	0.012	0.012967	0.003601	1.82×10^{-3}	6.72×10^{-2}
C2	2.88×10^{-4}	18×10^{-6}	0.012	0.012981	0.003603	3.33×10^{-3}	6.91×10^{-2}
C3	2.16×10^{-4}	15×10^{-6}	0.012	0.01303	0.00361	6.41×10^{-3}	7.23×10^{-2}
C4	1.44×10^{-4}	13×10^{-6}	0.012	0.013303	0.003647	1.58×10^{-3}	7.80×10^{-2}

4.2.4. NUMERICAL METHODS

In this study, the FineSed3D model is employed (Cheng *et al*., 2015a; 2015b). The FineSed3D model is a hybrid spectral-compact finite-difference model. The FineSed3D model uses pseudo-spectral methods in the periodic directions and a sixth-order compact finite difference scheme in the bed-normal direction. In this model, the semi-implicit second-order Crank-Nicolson method is used to calculate the diffusive terms. The non-linear terms are also calculated by the Arakawa method (Arakawa and Lamb, 1981) and integrated by a third-order, low-storage Runge-Kutta method (Cortese and Balachandar, 1995; Cantero *et al.*, 2008). The 3/2 rule is used for dealiasing (Canuto *et al.*, 1987; Peyret, 2002) and Arakawa method (Arakawa, 1966) are used to minimize

the aliasing errors. For an in-depth description of the numerical methods, the reader is referred to Cheng *et al.* (2015a).

4.2.5. NOTATION AND TERMINOLOGY

The analyses in Section 3 require the use of various variables obtained via different averaging or normalization. For better readability, we find it necessary to define them in this subsection. Mean velocity and concentration, discerned by an overbar, are obtained after averaging them over x-y planes at each discretized point in the vertical direction over a sampling time, T. The described averaging in equation form is shown for mean concentration as

$$\overline{c}(z) = \frac{1}{TL_yL_x}\int_{t=t_o}^{t=T}\int_{y=0}^{y=L_y}\int_{x=0}^{x=L_x} c(x,y,z,t)\,\mathrm{d}x\,\mathrm{d}y\,\mathrm{d}t, \tag{14}$$

where t_o indicates the time when equilibrium conditions starts. Depth-averaged of the mean, which will interchangeably be referred to as the volume-averaged, is obtained after averaging a quantity of interest over time and volume and is indicated by the angle brackets. As an example, the following obtains the volume-averaged concentration:

$$\langle c\rangle = \frac{1}{ThL_xL_y}\int_{t=t_o}^{t=T}\int_{z=0}^{z=h}\int_{y=0}^{y=L_y}\int_{x=0}^{x=L_x} c(x,y,z,t)\,\mathrm{d}x\,\mathrm{d}y\,\mathrm{d}z\,\mathrm{d}t. \tag{15}$$

To assess the role of the bed shear stress on the velocity structure, wall units, discerned by superscript "+", will be used. To obtain the wall units, the friction velocity, u_τ, and viscous length scale, ν/u_τ are respectively used to normalize velocity and distance, respectively. As mentioned, the initial bed shear stress, τ_{bo}, is augmented by the cross-shelf propagation of ACSTC. Therefore, total bed shear stress, τ_b, becomes $\tau_b = [\tau_{bo}^2 + (\mathfrak{B}\sin\theta)^2]^{1/2}$, making the friction velocity $u_\tau = (\tau_b/\rho)^{1/2}$. Thus, the velocity and position vectors, *i.e.*, $\boldsymbol{u} = (u,v,w)$ and $\boldsymbol{x} = (x,y,z)$, respectively, in wall units are

$$\boldsymbol{u}^+ = (u^+, v^+, w^+) = \left(\frac{u}{u_\tau}, \frac{v}{u_\tau}, \frac{w}{u_\tau}\right) \quad \text{and} \quad \boldsymbol{x}^+ = (x^+, y^+, z^+) = \left(\frac{u_\tau x}{\nu}, \frac{u_\tau y}{\nu}, \frac{u_\tau z}{\nu}\right). \quad (16)$$

4.3. RESULTS AND DISCUSSIONS

4.3.1. MEAN CONCENTRATION PROFILES

In this section an initial assessment of the simulation results is presented. Especially, the change in the mean concentration and velocity profiles with respect to initial normalized excess shear stress and settling velocity is analyzed. To identify the effect of initial normalized excess shear stress, S_o, Figure 2 plots the concentration profiles with respect to S_o for each w_s. It is expected that the eddy diffusivity will be closest to that in unidirectional turbulent channel flow for cases with $S_o = 0.05$, and thus the concentration profiles of these cases will be closest to the Rouse profile. Therefore, the Rouse profiles are also plotted in Figure 2 for the lowest of S_o values specified. The Rouse profile is given as

$$\overline{c}(z) = c_o \left[\left(\frac{z}{z_o}\right)\frac{(h - z_o)}{(h - z)}\right]^{-Ro}, \quad (17)$$

where c_o is the reference concentration at the reference height, z_o, and $Ro = w_s/(\kappa u_\tau)$ is the Rouse number. We chose $z_o = 0.008$ m, *i.e.*, $z^+ \approx 30$ in wall units, where turbulence becomes prevalent. Due to absence of an experimental data set to compare the simulation results, comparison with the Rouse profile with least stratified cases will serve as a verification of the model's capability to faithfully capture the turbulent suspension. Maximum concentration in the simulations is slightly larger than $2\ \mathrm{kg\,m^{-3}}$ which corresponds to a volumetric concentration of 1×10^{-3}. The volumetric sediment concentration is sufficiently dilute suggesting that the continuum assumption is reasonable for the sediment phase. With increasing S_o, SSC gets higher for each w_s. While SSC mostly resides approximately within the first $0.01\ m$ from the bed for the highest w_s, a gradual increase in SSC above $z = 0.01$ m with decreasing w_s is visible. A

noteworthy observation is the substantial increase in SSC as bed erodibility increases from $S_o = 0.11$ to 0.25 as opposed to that from $S_o = 0.05$ to 0.11, although the rate of change in S_o is similar. When $S_o = 0.25$, the downslope motion of the ACSTC and opposing shear stress becomes significant in magnitude. This augments the bed shear stress magnitude and allows more sediment suspension. Therefore, the difference mentioned is primarily a result of enhanced excess shear stress introduced by the cross-shelf propagation of ACSTC.

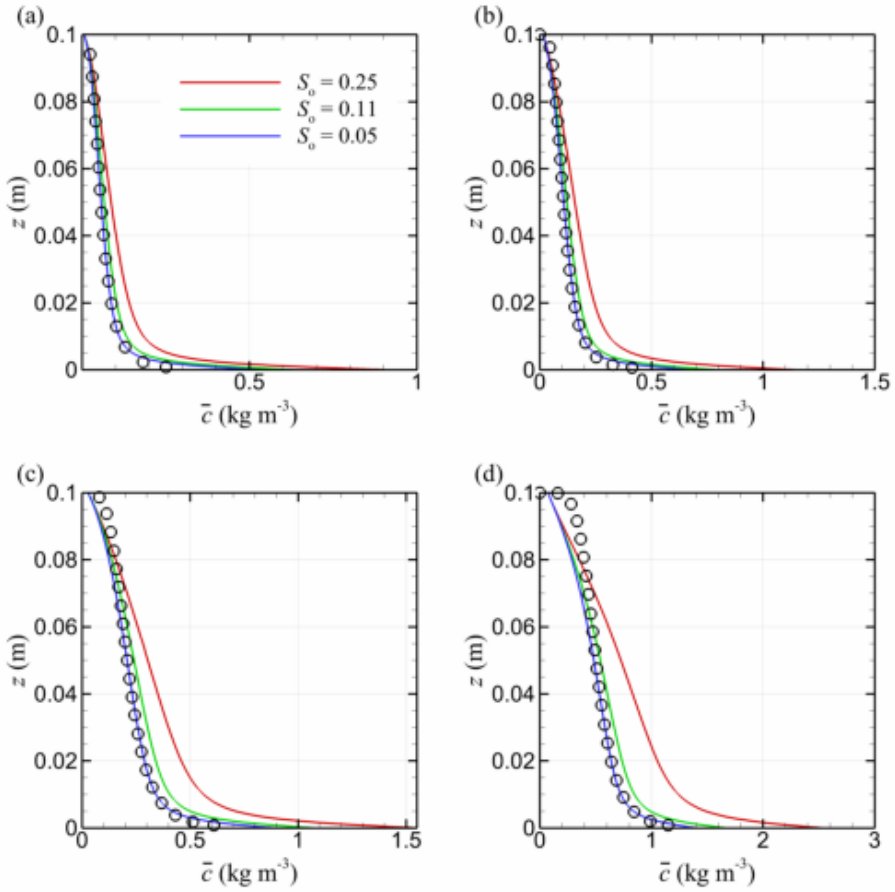

Figure 4.2. Time- and plane-averaged concentration, $\bar{c}$, profiles for (a) $w_s = 3.6 \times 10^{-4}\ m\ s^{-1}$, (b) $w_s = 2.88 \times 10^{-5}\ m\ s^{-1}$, (c) $w_s = 2.16 \times 10^{-5}\ m\ s^{-1}$, and (d) $w_s = 3.6 \times 10^{-5}\ m\ s^{-1}$.

The role of w_s is analyzed in Figure 3, where SSC profiles of cases with the same S_o are plotted. For each w_s, increasing SSC with decreasing w_s is clear. Referring to Figure 2 and Figure 3, both w_s and S_o are clearly the parameters that change the total SSC. Considering that the bottom

boundary provides unlimited sediment supply, both erosion parameters and sediment settling velocity impose control on total SSC. Therefore, total SSC must be quantified by taking the two parameters into account.

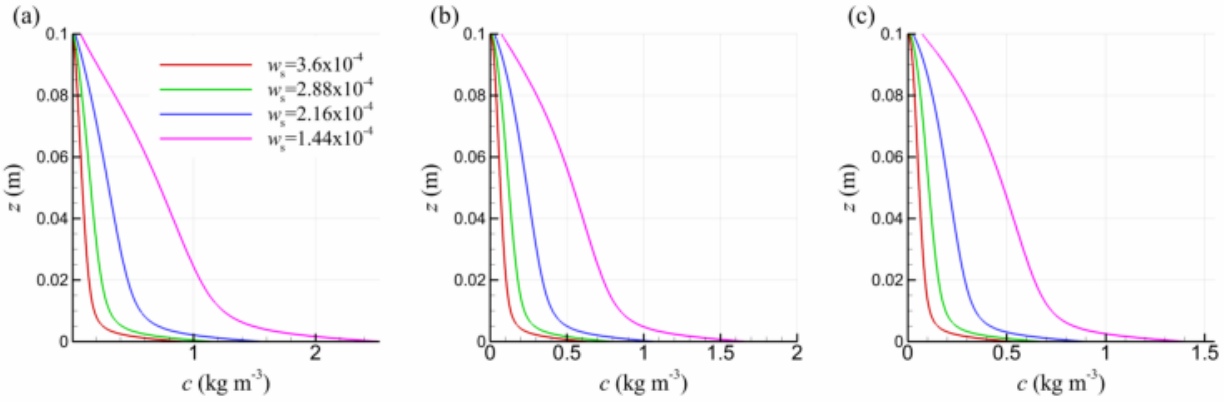

Figure 4.3. Time- and plane-averaged concentration, $\bar{c}$, profiles for (a) $S_o = 0.25$, (b) $S_o = 0.11$, and (c) $S_o = 0.05$.

4.3.2. MEAN VELOCITY PROFILES

Flow in an ACSTC is a boundary-layer flow stratified by sediment suspension. Another important characteristic of the flow in ACSTCs is its two-directionality. Density stratification play a significant role as to the direction of mean velocity. From the velocity hodographs of Case A4 shown in Figure 4, bed shear has a dominant role near the bed, and hence the velocity vector aligns with the bed shear stress. Away from the bed, however, the effect of bed shear stress is relaxed, and there is a deviation in the mean velocity vector's direction. These observations are similar to those in turbulent Ekman boundary layers (*e.g.*, Deusebio *et al.*, 2014; Spalart *et al.*, 2008), albeit with a smaller deviation in the direction of velocity vector here.

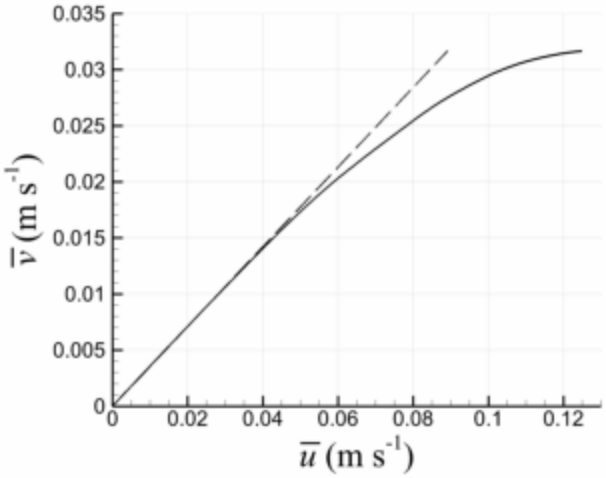

Figure 4.4. Time- and plane-averaged velocity hodograph of Case A4, *i.e.*, $w_s = 1.44 \times 10^{-4}\ m\ s^{-1}$ and $S_o = 0.25$ (solid curve). The principal direction of the bed shear stress (dashed line) shows the directional variation in the time- and plane-averaged velocity vector.

Therefore, to assess the velocity structure in an ACSTC, one must refer to the profile of velocity vector's magnitude, $|\overline{\boldsymbol{u}}| = \left(\overline{u}^2 + \overline{v}^2\right)^{1/2}$, rather than its components. Figure 5 plots the profiles of $|\overline{\boldsymbol{u}}|$ for each S_o. Increasing velocity gradient is discerned for decreasing settling velocity. This increase appears to be maximum for the highest S_o and SSC.

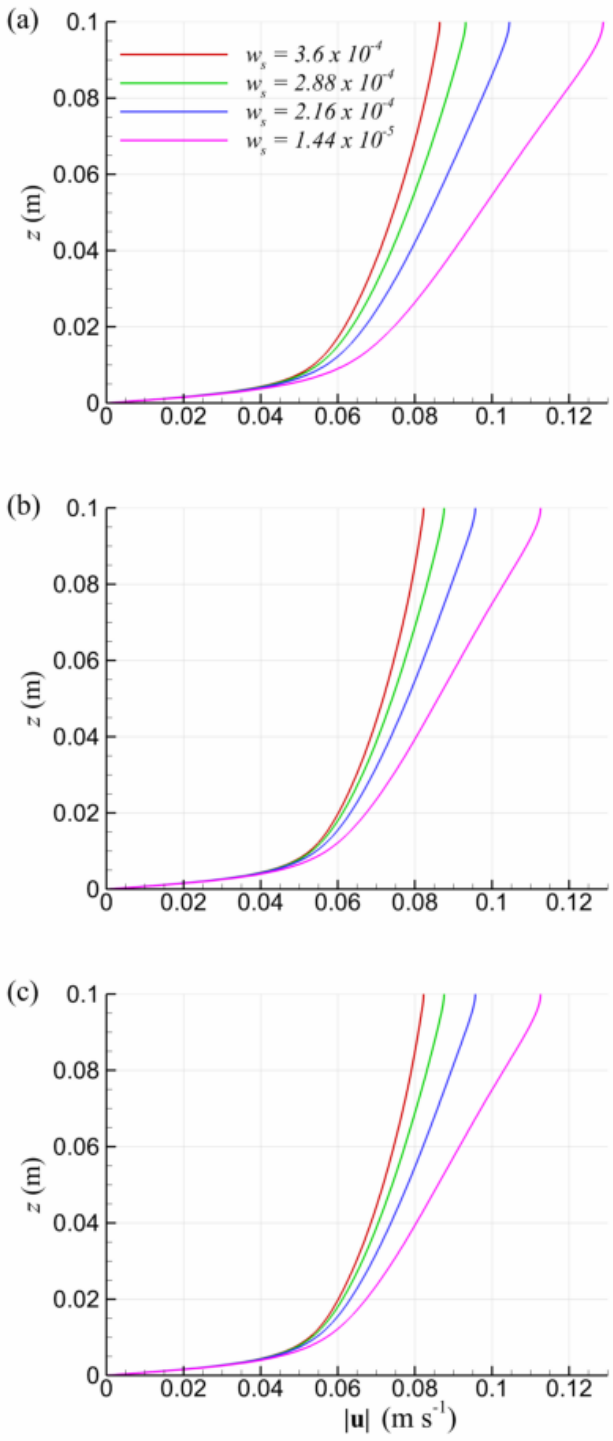

Figure 4.5. Time- and plane-averaged velocity magnitude profiles of cases with (a) $S_o = 0.25$, (b) $S_o = 0.11$, and (c) $S_o = 0.05$.

To have proper understanding of the velocity structure, velocity profiles are plotted in wall units. Velocity profiles in wall units are presented in Figure 6. For comparison, we plotted the log law profile in dashed line, in which the logarithmic velocity profile is

$$|\overline{\boldsymbol{u}}|^+ = \kappa^{-1} \ln z^+ + B. \tag{18}$$

In Equation (18), κ and B are the von Kármán and additive constants, respectively. From Figure 6, it is observed that the log layer gets thinner and the wake layer above the log layer stretches with increasing concentration (or decreasing w_s). This is in line with the observations in the literature reporting that stable density stratification starts modulating the velocity profile in the outer layer (Armenio and Sarkar, 2002; Garg *et al*., 2000). More important, increase in the von Kármán constant with the reduction in settling velocity is noticeable. It is well-known that reduction in the von Kármán constant is a result of stratification-induced turbulence destruction, which reduces the Reynolds shear stress and increases viscous shear stress, thus, the velocity gradient.

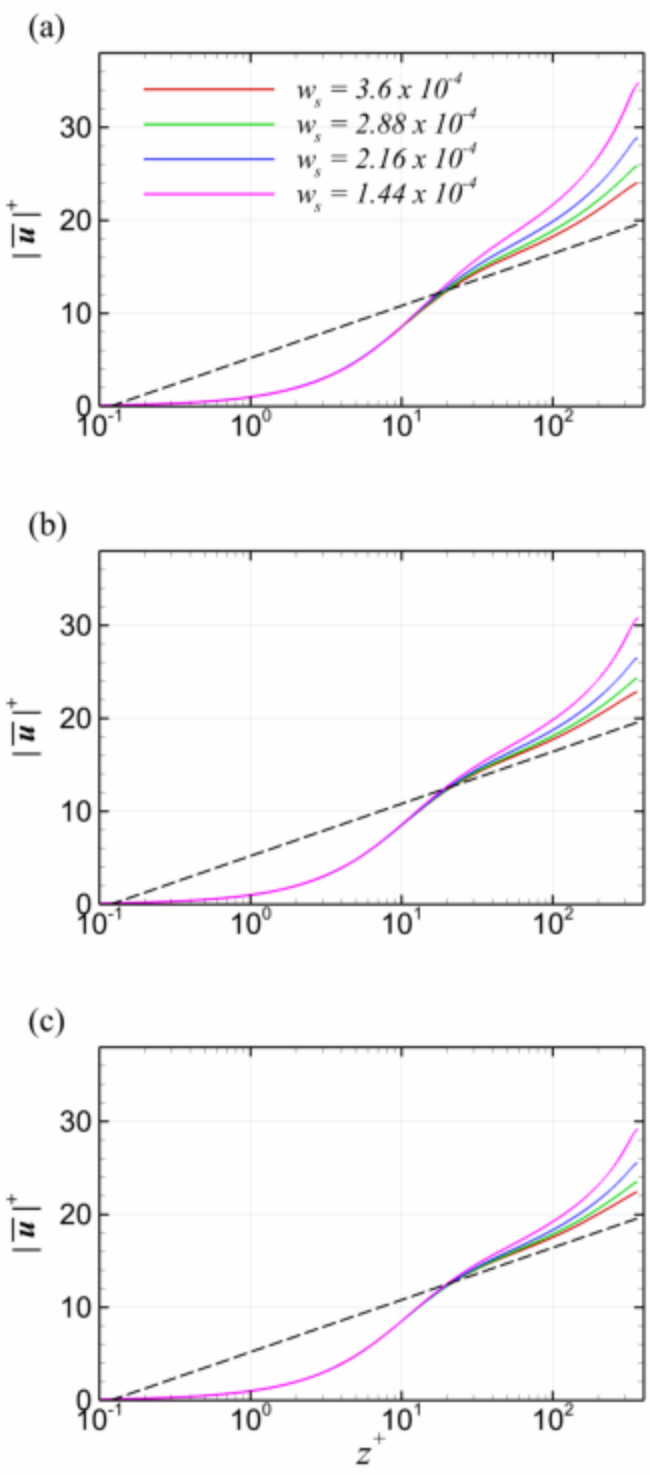

Figure 4.6. Plane- and time-averaged velocity magnitude profiles in wall units, *i.e.*, z^+ versus $|\overline{\boldsymbol{u}}|^+$ (see Equation (16 a, b) for their definition). Subfigures (a) to (c) show the profiles of cases with $S_o = 0.25$, $S_o = 0.11$, and $S_o = 0..05$, respectively.

By expanding the law of the wall, the change in the slope of $|\overline{\boldsymbol{u}}|^+$ in the log layer is assessed though the profiles of the Kármán measure, Ξ, which is defined as

$$\Xi = \left(z^+ \frac{\mathrm{d}|\overline{\boldsymbol{u}}|^+}{\mathrm{d}z^+} \right)^{-1}. \tag{19}$$

Note that Ξ becomes equal to κ in the log-layer allowing us to assess the value of κ. Figure 7(a-c) represents the profiles of Ξ that are contrasted with that of Case 0 in which sediments are neutrally buoyant and cannot create stable density stratification. According to Figure 7(a-c), within $z^+ = [10, 150]$, Ξ reaches a peak value at around $z^+ \simeq 50{\sim}70$ and then decays. With decrease in w_s and S_o, the profiles deviate from Case 0 and result in lower Ξ values suggesting a higher level of density stratification. For Case 0, the peak value is about $\Xi = 0.41$, which is the commonly accepted value of the von Kármán constant. Thus, we chose the peak Ξ values within $z^+ = [50{,}200]$ as the von Kármán constant, where its variation with respect to w_s is shown in Figure 7(d). Decreasing w_s leads to a decrease in κ. From the same figure, reduction in κ with increasing erodibility and sediment concentration is also observed. These two observations suggest that both SSC and w_s play part in sediment-induced density stratification, which is in line with the findings of the previous studies (Winterwerp 2001; 2009, Cantero *et al*., 2012).

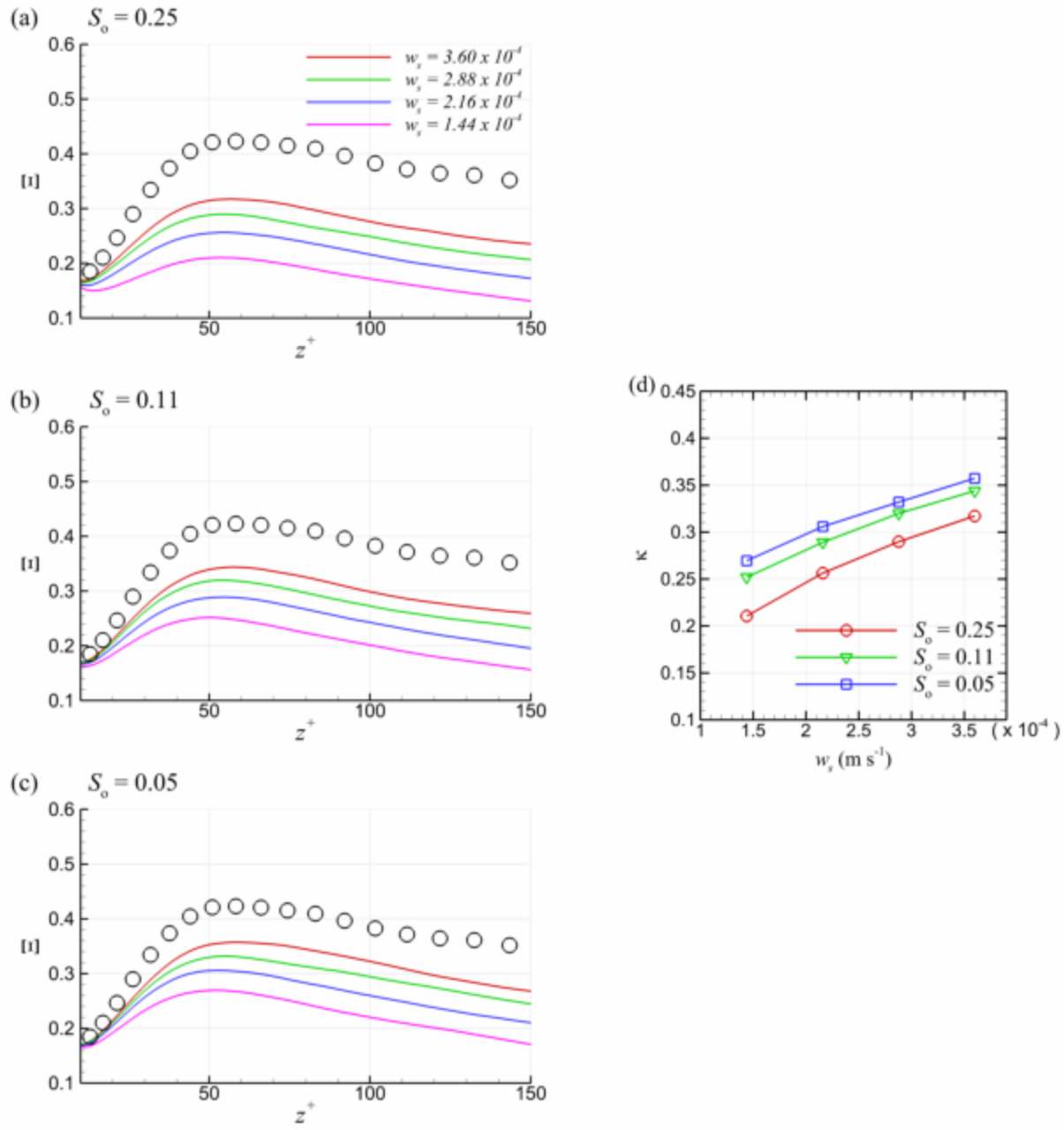

Figure 4.7. (a) Kármán measure, Ξ, profiles in wall units (See Equation (16a,b)). Subfigures (a) to (c) shows Ξ profiles of cases with $S_o = 0.25$, $S_o = 0.11$, and $S_o = 0..05$, respectively. In (a-c) hollow circles corresponds to Ξ profile of Case 0, which is shown to identify the difference between non-stratified and stratified cases. The maximum of Ξ within $z^+ = [25,150]$ is assumed to be the representative value of the von Kármán constant, κ. Variation of the von Kármán constant with respect to w_s is shown in (d) for each S_o.

As the literature on WCSTCs does not consider w_s solely as one of the governing parameters of the density stratification, we find it instructive to provide a brief explanation as to the role of w_s on turbulence destruction, perhaps at the risk of oversimplifying the phenomenon. In a stratified

medium where density stratification is not created by the sediment suspension, turbulence destruction is a result of reduction in the vertical momentum exchange due to density gradient. If density stratification is created by the sediment suspension, it is the negative momentum of settling sediments that reduces the aforementioned momentum exchange. Therefore, not only the sediment concentration, but also the settling velocity of sediment suspension plays a role in turbulence destruction. Perhaps, the variation of κ with respect to the product of settling velocity and sediment concentration will convincingly illustrate this point. For that, we prefer using dimensionless numbers, and as a measure of sediment concentration, we define the Richardson number as in the following:

$$Ri_\tau = \frac{(s-1)g\langle\langle c\rangle\rangle h}{u_\tau^2}\,. \tag{20}$$

Note that Ri_τ can also be interpreted as the ratio between the buoyant and the friction force at the bed. Also normalizing w_s with u_τ, κ is plotted with respect to $Ri_\tau w_s/u_\tau$ in Figure 8. The von Kármán constants collapse into a single line that is a function of $Ri_\tau w_s/u_\tau$ which follows

$$\kappa = \kappa_o\left(1 - 0.41\frac{w_s}{u_\tau}Ri_\tau\right), \tag{21}$$

where κ_o is the von Kármán constant for unstratified boundary layers and is equal to 0.41. Supported by the previous studies, this observation is a clear indication that the product of settling velocity with the sediment concentration quantifies the sediment-induced stable density stratification. The degree of stable density stratification, henceforth, is quantified by $w_s Ri_\tau/u_\tau$ in this chapter.

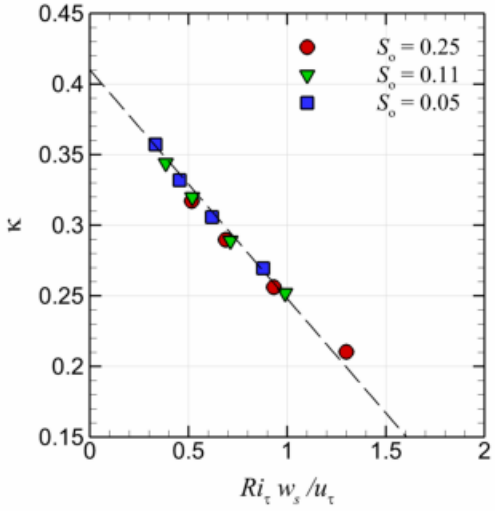

Figure 4.8. Variation of the von Kármán constant with respect to $Ri_\tau w_s/u_\tau$. Dashed line plots Equation (20) which is the best-fit line for κ obtained from the simulations. Equation (20) is obtained by assigning $\kappa = 0.41$ as the intercept in y-axis to ensure physical consistency, *i.e.*, when $Ri_\tau w_s/u_\tau \to 0$, $\kappa \to 0.41$. The coefficient of determination for this fit was obtained as $r^2 = 0.988$.

4.3.3. PARAMETERIZATION OF THE DRAG COEFFICIENT IN ACSTCS

To help quantify the shelf-wide sediment budgets associated with ACSTCs, it is imperative to upscale the fine-scale processes involved in ACSTCs via parameterization. To this end, governing physical mechanisms and associated parameters of the cross-shelf flux must be identified. One of the unique characteristics of WCSTCs is the development of the equilibrium conditions. In other words, a force balance is established between the cross-shelf component of density anomaly and opposing shear force at the bed (Wright *et al*., 2001) which was confirmed by the rigorous analyses of the measurements taken close to the Rhine River mouth (Flores *et al*., 2018). Therefore, steady flow conditions apply, which makes it relatively easier to quantify the downslope velocity relative to those in classical turbidity currents where flow is highly transient. In this regard, the magnitude of velocity with which ACSTCs propagate in the cross-shelf direction are central to the quantification and parameterization of the sediment fluxes induced by ACSTCs.

One of the least understood aspects of WCSTCs and ACSTCs is associated with the values of the drag coefficient, C_d, and its variation with respect to sediment-induced density stratification. The studies in the literature mainly propose a reasonable range of drag coefficients, *i.e.*, $C_d = 0.003{\sim}0.006$ (Wright *et al.*, 2001) for WCSTCs including ACSTCs, and the dependence of C_d on density stratification was acknowledged. However, a mechanistic explanation of the given range of values and a relation to describe the reduction of C_d with appropriate parameters of density stratification is not available to date. In this section, we analyze the variation of C_d with respect to density stratification in reference to the modulation in the velocity structure and seek relation for C_d with appropriate parameters.

In any flow with solid boundary, the (skin) friction coefficient, C_f, is intimately associated with the vertical velocity structure. This is because the friction coefficient for a given bed shear stress (τ_b) is expressed as $C_f = \tau_b/(\rho_f|\boldsymbol{u^2}|)$. Therefore, density stratification-induced reduction in C_f is a result of modulation in the mean velocity structure by the turbulence destruction. It follows from this explanation that the variation in the velocity profile must be analyzed to develop relations for the friction coefficient, and thus drag coefficient. Yet, one complexity associated with ACSTCs is their being two-directional wherein the direction of the velocity vector varies vertically (Ozdemir and Yu, 2018). For these kinds of flows, such as those in the Ekman boundary layers, quadratic drag relation is cast between the magnitude of the bed shear stress and the magnitude of the mean velocity vector. This relation translates to ACSTCs as

$$\tau_b = [\tau_{bo}^2 + (\mathfrak{B}\sin\theta)^2]^{1/2} = \rho_f C_f(\langle u\rangle^2 + \langle v\rangle^2). \tag{22}$$

On the other hand, the relation proposed for the cross-shelf motion of ACSTCs, *i.e.*, Equation (3), considers the cross-shelf bed shear stress only. Using Equations (3) and (22), one can infer that for

C_f to be equal to C_d, the mean velocity vector's direction must align with the principal direction of the bed shear stress (PDBSS):

$$\frac{\mathfrak{B}\sin\theta}{\tau_{bo}} = \frac{\langle v\rangle}{\langle u\rangle}. \tag{23}$$

However, PDBSS and the mean velocity vector do not necessarily align. In this regard, we compare the calculated values of C_d against C_f along with $\langle v\rangle/\langle u\rangle$ against $\mathfrak{B}\sin\theta/\tau_{bo}$ (see Figure 9(a-b)). Values of C_f and C_d are in agreement, but C_d is slightly, yet consistently, larger than C_f. Shown also in Figure 9(b), there is a directional mismatch between the mean velocity vector and PDBSS which becomes pronounced as density anomaly increases. Whether the observed difference between C_d and C_f is solely a result of the aforementioned directional mismatch was checked by comparing C_f with C_d multiplied by $(\langle u\rangle\mathfrak{B}\sin\theta)/(\langle v\rangle\tau_{bo})$, which is shown in Figure 9(c). Almost an exact match between the two confirms that the directional mismatch between the mean velocity vector and PDBSS explains the difference between the C_d and C_f. From the given analyses it is concluded that the variation of C_d closely follows that of C_f, and thus they are tightly linked. From the tight link between C_f and C_d, we conjecture that the governing parameters of C_f also governs C_d. In addition, the link between C_f and C_d provides us with a clear direction to develop relations for C_d; we will first seek a relation for C_f with respect to density stratification, and develop a correction function to account for the difference between C_f and C_d. Therefore, as a first step, we analyze the variation in C_f with varying degree of density stratification.

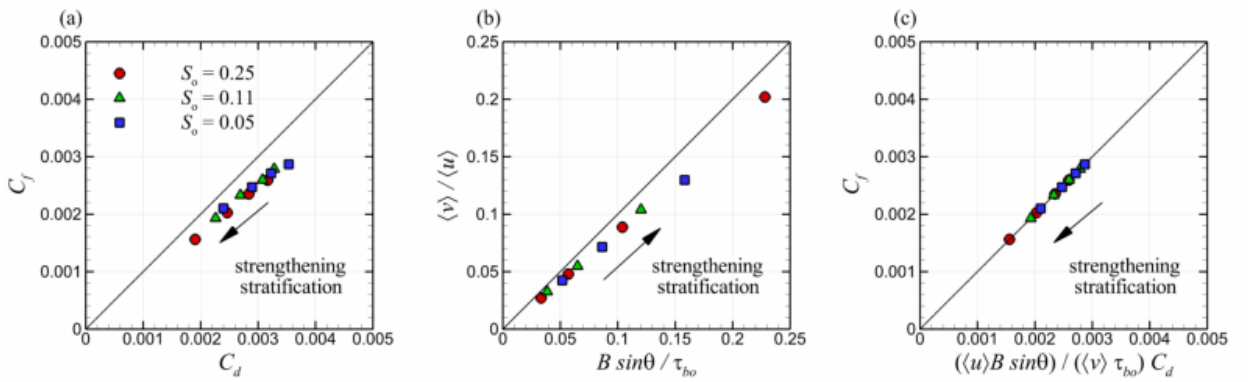

Figure 4.9. (a) Comparison of the drag coefficient (C_d; obtained from Equation (3)) and the friction coefficient (C_f, obtained from Equation (21)) from the simulations herein. (b) $\mathfrak{B}\,sin\,\theta/\tau_{bo}$ versus $\langle v\rangle/\langle u\rangle$ is plotted to assess the directional mismatch between the depth-averaged mean velocity vector and the principal direction of the bed shear stress. The fact that all data points fall below 1:1 line shows that the mean velocity vector shifts towards the alongshore direction. (c) Drag coefficient multiplied by $(\mathfrak{B}\,sin\,\theta\,\langle v\rangle)/(\tau_{bo}\langle u\rangle)$ against C_f to verify the directional mismatch between the principal direction of the bed shear stress and the depth-averaged mean velocity vector is the sole reason for the difference between the drag and the friction coefficients.

4.3.3.1. FRICTION COEFFICIENT ESTIMATION

The values of friction coefficients at the limit conditions of ACSTCs would find a useful basis to develop relations for varying degree of density stratification. The two limit conditions for ACSTCs are: (i) their transition to self-sustaining turbidity currents and (ii) their cease due to dilution of SSC. The former is a transient phenomenon and lacks a well-established relation. The latter, however, provides valuable insights that will be discussed in the following. When sediment suspension vanishes, so does the cross-shelf velocity, and hence the flow becomes almost unidirectional. Under such conditions, the structure of the velocity profile conceivably becomes close to those in steady unidirectional turbulent flows. It follows that the friction coefficient, C_f, must approach to that estimated for steady turbulent boundary layers. Therefore, we compared the C_f values obtained from the simulations with those estimated by the logarithmic skin friction law

$$C_{fo} = \left[\frac{1}{\kappa}\ln\left(Re_o C_{fo}^{1/2}\right) + \mathcal{A}\right]^{-\frac{1}{2}}. \tag{24}$$

Here, Re_o is the Reynolds number calculated by using the depth-averaged mean velocity, $\langle|\boldsymbol{u}|\rangle$, and flow depth, h, and $\mathcal{A}$ is a constant associated with the velocity profile which is taken as $\mathcal{A} = 4.54$ (See Dean, 1978). One must note that the given friction coefficient is $C_{fo} = (u_\tau/\langle|\boldsymbol{u}|\rangle)^2$ for turbulent boundary-layer flows. Comparison of C_{fo} and C_f in Figure 10 suggests that towards vanishing density stratification C_f converges to C_{fo}, and hence C_{fo} can be taken as the limit value when $\langle c\rangle \to 0$. With strengthening density stratification, C_f becomes smaller with a marked departure from C_{fo}.

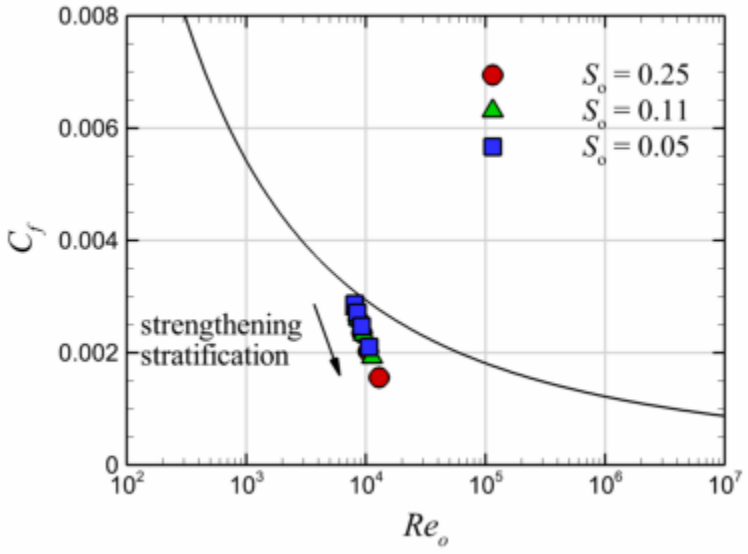

Figure 4.10. Comparison of the friction coefficients from the simulations (in symbols) with the logarithmic law of friction (solid black curve) over Re_o-C_f plane. Solid arrow parallel to the symbols indicate the increasing density stratification.

The question that follows is how to establish a relation to account for the aforementioned decrease in C_f. To do that, one must analyze the modulation in the velocity profiles for various degrees of density stratification. Vertical structure of the velocity is comprised of the viscous, buffer, logarithmic and the wakes layers. Ignoring the slight inaccuracy near the bed, the following well represents the velocity profile:

$$\frac{|\overline{\boldsymbol{u}}|}{u_\tau} = \frac{1}{\kappa}\ln\left(\frac{u_\tau z}{\nu}\right) + B + \frac{\Pi}{\kappa}\mathcal{W}\left(\frac{z}{h}\right). \tag{25}$$

In Equation (25), B is the additive constant, Π is the wake strength and $\mathcal{W}$ is the wake function. In the same equation, dependence of logarithmic and the wake layers on κ clearly suggests that κ is of pivotal importance to the vertical velocity structure, and thus the friction coefficient. Indeed, in steady turbulent boundary layers, C_f is a function of κ (*cf.* Schlichting and Gersten, 2000, p. 537). To this end, contributions of the logarithmic and the wake functions along with the additive constant with respect to decreasing κ is analyzed. For convenience, the details of this analysis are deferred to Appendix C1, but the overall results are shown in Figure 11. With respect to κ^{-1}, contributions of the logarithmic and the wake layers increase, but the additive constant decreases. To be noted, the increase in the logarithmic contribution and the decrease in the additive constant are almost linear. Because the logarithmic part is by far the largest contributor to the depth-averaged mean velocity, depth-averaged mean velocity also increases almost linearly with respect to κ^{-1}. It must be noted that depth-averaged mean velocities shown in Figure 11(d) are normalized by the friction velocity. When normalized by the friction velocity, depth-averaged mean velocity, $\langle|\boldsymbol{u}|\rangle$, becomes equal to the square root of the friction coefficient because $\tau_b/\rho_f = C_f\langle|\boldsymbol{u}|\rangle^2 = u_\tau^2$. Therefore, a relation for $\langle|\boldsymbol{u}|\rangle$ as a function of κ will also provide a relation for C_f. The simplest choice here is to predict this relation through curve fitting; but the consistency of this relation in the limit of $\langle c\rangle \to 0$ must be ensured.

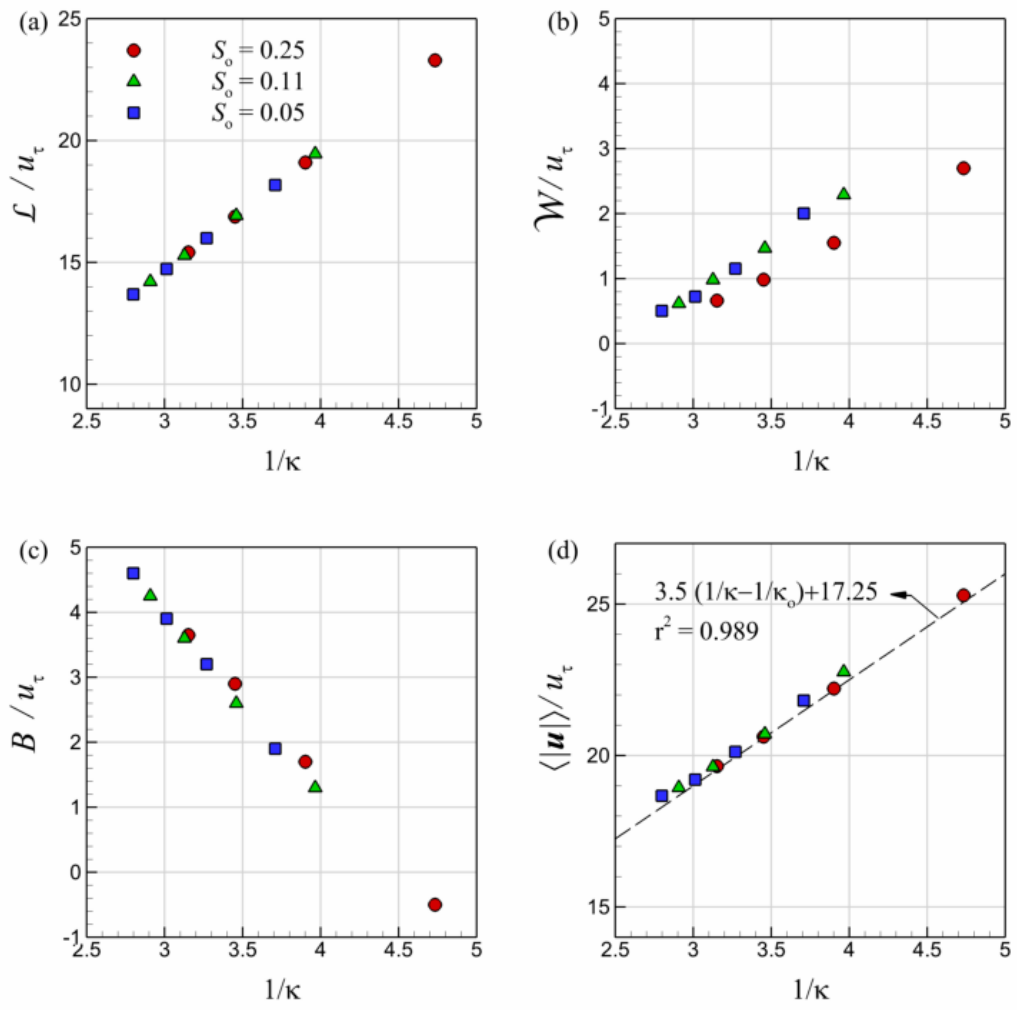

Figure 4.11. (a-c) Variation of depth-averaged mean velocity components with respect to $1/\kappa$, where (a) shows the logarithmic contribution, $\mathcal{L}$, (b) shows the wake function, $\mathcal{W}$, contribution, and (c) is the additive constant's, B, contribution to the depth-averaged velocity. (d) Variation of depth-averaged velocity magnitude with respect to $1/\kappa$. Dashed line in (d) is the line that best fits the data obtained from the simulations. Best-fitting line has a coefficient of determination $r^2 = 0.9966$, and satisfies the limit constraint when $\kappa \to \kappa_o = 0.41$.

To expand our discussion, we believe it is useful to present the relation we obtained up front, which is given as:

$$C_f^{-1/2} = \frac{\langle|\boldsymbol{u}|\rangle}{u_\tau} = C_{fo}^{-1/2} + 3.345\left(\frac{1}{\kappa} - \frac{1}{\kappa_o}\right). \tag{26}$$

By using the form within the parentheses, increasing mean velocity is quantified as a function of κ. The rightmost term satisfies the limit conditions when $\langle c\rangle \to 0$, *i.e.*, $\kappa \to \kappa_o$. If Equation (26) is

evaluated for $\kappa = \kappa_o$, C_f recovers to the logarithmic skin friction law (see Equation (24)). Indeed, while obtaining the best-fit relation, the rightmost term of Equation (25) is introduced as a constraint to satisfy the logarithmic skin friction law when $\kappa = \kappa_o$, *i.e.*, $C_{fo}^{-1/2} = 17.25$. It must also be noted that the coefficient of determination for the relation obtained is notable, *i.e.*, $r^2 = 0.9966$. By using Equation (20), Equation (25) can be further expanded as a function of settling velocity and sediment concentration, which are respectively quantified through w_s/u_τ and Ri_τ:

$$\frac{1}{\kappa} - \frac{1}{\kappa_o} = \frac{1}{\kappa_o}\left[\frac{0.41\left(\frac{w_s}{u_\tau}Ri_\tau\right)}{1 - 0.41\left(\frac{w_s}{u_\tau}Ri_\tau\right)}\right]. \tag{27}$$

Thus, the following gives the friction coefficient

$$C_f = \left\{C_{fo}^{-1/2} + \frac{3.345}{\kappa_o}\left[\frac{0.41\left(\frac{w_s}{u_\tau}Ri_\tau\right)}{1 - 0.41\left(\frac{w_s}{u_\tau}Ri_\tau\right)}\right]\right\}^{-2}. \tag{28}$$

To assess the modeling errors associated with curve fitting observed and estimated C_f are compared in Figure 11, which shows a good agreement.

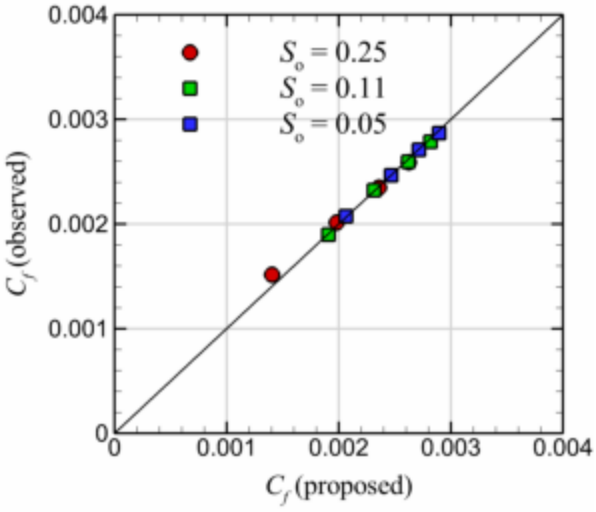

Figure 4.12. Comparison of the proposed versus observed drag coefficients to assess the modeling errors due to curve fitting.

4.3.3.2. CORRECTION FOR THE DRAG COEFFICIENT

The proposed relation for friction coefficient is a step towards establishing a relation for the drag coefficient. However, the difference between the values of C_f and C_d must be revisited to develop a possible correction factor. Referring to Figure 9, the aforementioned difference is a result of the directional mismatch between the PDBS and the mean velocity vector. It is worth reemphasizing that although the directional mismatch is more emphasized for cases with stronger density stratification, the difference between the drag and the friction coefficients becomes pronounced towards least stratified cases. Noting that $\mathfrak{B}/\tau_b = Ri_\tau$ and referring to Equation (3) and Equation (21), the ratio between the friction and the drag coefficients, after algebraic steps, is obtained as

$$\frac{C_f}{C_d} = (Ri_\tau \sin\theta)^{-1} \frac{\langle v \rangle}{\langle |\boldsymbol{u}| \rangle}. \tag{29}$$

Yet, most possibly because $\langle |\boldsymbol{u}| \rangle$ depends on $\langle v \rangle$, curves fitted to $\langle v \rangle / \langle |\boldsymbol{u}| \rangle$ as a function of w_s/u_τ, Ri_τ, and $Ri_\tau w_s/u_\tau$, have notable scatter (not shown). Therefore, an alternative form of Equation

(29) as a function of independent, or weakly dependent, variables provides a more accurate relation. To this end, we define cross-shelf velocity deficit, Δv, as the difference between the cross-shelf velocity if the velocity vector and PDBSS were aligned and that observed in the simulations (see also Figure 13(a)). Also, the magnitude of the mean velocity vector is assumed to be the same for both cases. Thus, the cross-shelf velocity deficit reads

$$\Delta v = (Ri_\tau \sin\theta)\langle|\boldsymbol{u}|\rangle - \langle v\rangle. \tag{30}$$

Our choice of cross-shelf velocity deficit as a variable is based on our observation in Figure 9, where the deviation of the mean velocity vector's direction from PDBSS increases with density stratification. The cross-shelf velocity deficit is tightly linked to the difference in the alignment of $\langle\overline{\boldsymbol{u}}\rangle$ and PDBSS and thus is a function of density stratification. By using Equation (29) and Equation (30), the following is obtained for the ratio between the friction and the drag coefficients after a few algebraic steps

$$\frac{C_f}{C_d} = 1 - (Ri_\tau \sin\theta)^{-1}\frac{\Delta v}{\langle|\boldsymbol{u}|\rangle}. \tag{31}$$

From Equation (31), one may argue that Δv and $\langle|\boldsymbol{u}|\rangle$ are dependent. However, magnitude-wise Δv is far smaller than $\langle|\boldsymbol{u}|\rangle$; hence, dependence of $\langle|\boldsymbol{u}|\rangle$on Δv is very weak. In fact, $\Delta v/\langle|\boldsymbol{u}|\rangle$ well fits a quadratic function of $w_s Ri_\tau$ with minimal scatter as in Figure 13(b), which thus supports our argument. The aforementioned quadratic relation is given as

$$\frac{\Delta v}{\langle|\boldsymbol{u}|\rangle} = 0.024\left(\frac{w_s}{u_\tau}Ri_\tau\right)^2 + 0.0037\left(\frac{w_s}{u_\tau}Ri_\tau\right). \tag{32}$$

It follows from Equation (32) that

$$C_d = f\left(\frac{w_s}{u_\tau}, Ri_\tau, \theta\right)C_f, \tag{33}$$

where f is the correction function, which is given as

$$f\left(\frac{w_s}{u_\tau}, Ri_\tau, \theta\right) = \left\{1 - (Ri_\tau \sin\theta)^{-1}\left[0.024\left(\frac{w_s}{u_\tau}Ri_\tau\right)^2 + 0.0037\left(\frac{w_s}{u_\tau}Ri_\tau\right)\right]\right\}^{-1}. \quad (34)$$

Shown in Figure 14, C_f after multiplied by the given correction function compares very well with the drag coefficient. With all the considerations of the relation between C_{fo} and C_f along with that between C_f and C_d, we propose the following relation for the drag coefficient

$$C_d = f\left(\frac{w_s}{u_\tau}, Ri_\tau, \theta\right)\left\{C_{fo}^{-1/2} + \frac{3.345}{\kappa_o}\left[\frac{0.41\left(\frac{w_s}{u_\tau}Ri_\tau\right)}{1 - 0.41\left(\frac{w_s}{u_\tau}Ri_\tau\right)}\right]\right\}^{-2}. \quad (35)$$

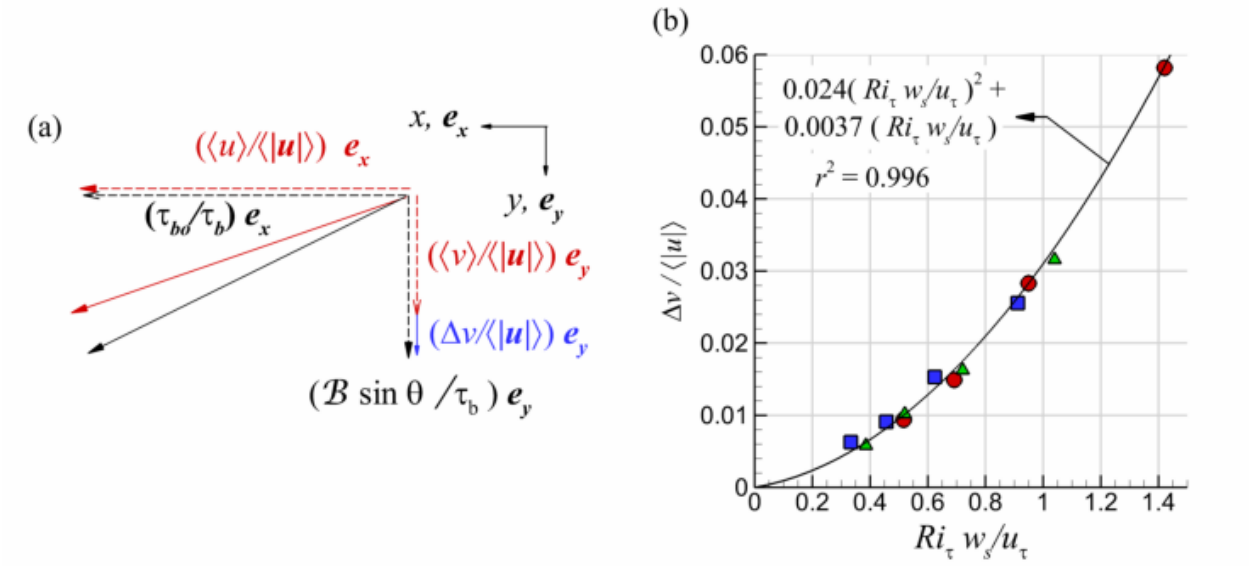

Figure 4.13. (a) Visual description of the cross-shelf velocity deficit. The unit vector indicated in solid red arrow points in the direction of the depth-averaged mean velocity vector. Its components are indicated in red-dashed arrows with along-shelf and cross-shelf components $(\langle u\rangle/\langle|\boldsymbol{u}|\rangle)\ \boldsymbol{e_x}$ and $(\langle v\rangle/\langle|\boldsymbol{u}|\rangle)\ \boldsymbol{e_y}$, respectively. Similarly, solid black arrow represents the unit vector that points in the principal direction of the bed shear stress with along- and cross-shelf components $(\tau_{bo}/\tau_b)\ \boldsymbol{e_x}$ and $(\mathcal{B}\sin\theta)/\tau_b)\boldsymbol{e_y}$, respectively. The vector in solid blue corresponds to the velocity deficit normalized by $\langle|\boldsymbol{u}|\rangle$. Cross-shelf velocity deficit is the difference in the cross-shelf component of the mean velocity vector, if it were to align with the bed shear stress (in solid black), and the actual one. (b) Variation of the normalized cross-shelf velocity deficit with respect to $Ri_\tau w_s/u_\tau$.

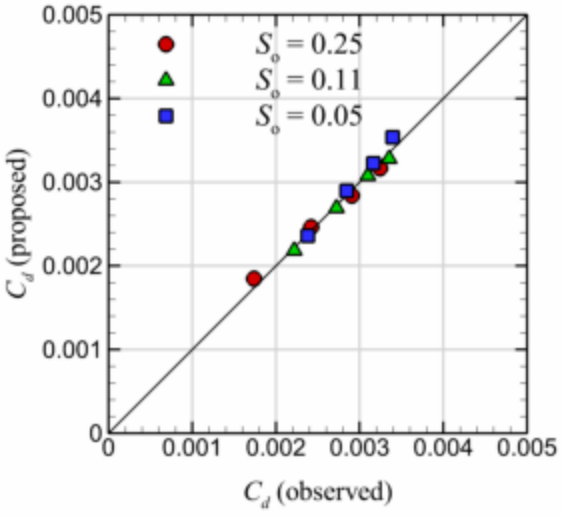

Figure 4.14. Comparison of the friction coefficient corrected by the correction function in Equation (33) with the observed drag coefficients.

4.4. SUMMARY AND CONCLUSIONS

This study investigated the velocity structure of a miniature along-shelf current supported turbidity current created via sediment suspension over erodible bed composed of loose fine sediments. Direct numerical simulations were run for various bed erosion parameters and sediment settling velocities. Suspended sediment concentration and velocity profiles were analyzed. Especially, the change in the velocity profiles with respect to sediment-induced stable density stratification and its effect on the drag coefficient is investigated. The profiles of SSC suggest that the amount of sediment suspension increases with decreasing sediment settling velocity and increasing bed erodibility. The implication is that sediment-induced density stratification perhaps does not impose the strongest control on the amount of sediment suspension. Further investigation is needed to identify the role of density stratification on the total amount of sediment suspension.

The effect of density stratification on the velocity structure is observed through the decreasing von Kármán constant in the logarithmic layer and increasing velocity magnitude in the wake layer. It was also observed in the wake layer that there is a directional change of velocity towards

alongshore direction. The aforementioned directional deviation is found to increase as the density stratification increases. It was also shown that the density stratification can be quantified by the product of the sediment settling velocity and concentration, *i.e.* w_s/u_τ and Ri_τ, respectively. This observation is in line with the previous studies (Winterwerp, 2001; Cantero *et al*., 2012; Ozdemir *et al*., 2011). A linear decrease in the von Kármán constant as a function of $Ri_\tau w_s/u_\tau$ was observed.

To develop a relation for the drag coefficient, friction coefficient (c_f) is defined, similar to those in two-directional flows, and compared with the drag coefficient. In fact, the drag and the friction coefficients must be equal as long as the mean velocity vector and the PDBSS align. Although both of them show a similar variation with strengthening density stratification, the drag coefficient was observed to be larger due to directional change in the velocity towards alongshore direction. The friction coefficient was further analyzed in the limit condition when suspended sediment concentration vanishes and becomes equivalent to those in steady turbulent boundary layers. This was confirmed by the close proximity between the friction coefficient of the least stratified cases and with those in the turbulent boundaries. The deviation of the friction coefficients obtained from the simulations from those of the steady turbulent boundary layers was observed to be functions of $Ri_\tau w_s/u_\tau$. Similarly, the difference between the drag and friction coefficients is quantified as a function of $Ri_\tau w_s/u_\tau$. As a result, a relation, which is a function of the Reynolds number, the Richardson number (Ri_τ), settling velocity and slope is proposed.

The simulations were conducted for a miniature along-shelf turbidity current and does not scale with the actual alongshore turbidity currents. However, the parametric dependence of the drag coefficient to relevant dimensionless numbers provides a useful basis on the mechanisms that determine the drag coefficient. Particularly, dependence of the drag coefficient on the Reynolds

number is notable. Here the Reynolds number must be regarded as a parameter that shapes the velocity profile and the velocity deficit due to boundary effect. Thus, the Reynolds number affects the drag coefficient. Related to this aspect, it must be noted that the simulations are conducted for a smooth bed. In the presence of multi-grain sediment size, roughness elements may form (Hooshmand *et al*., 2015). It is conjectured that the roughness height is an effective, perhaps decisive, parameter particularly at sufficiently high Reynolds numbers similar to those in rough turbulent flows.

5. DIRECT NUMERICAL SIMULATIONS OF MINIATURE ALONG-SHELF CURRENT-SUPPORTED TURBIDITY CURRENTS: ROLE OF EROSION PARAMETERS AND SETTLING VELOCITY ON TRANSITION TO SELF-SUSTAINING TURBIDITY CURRENTS

5.1. INTRODUCTION

Turbidity currents are one of the agents responsible for rapid sediment emplacement of the shelf sediments to deep ocean. They are also threats to submarine infrastructure such as oil pipelines and telecommunication cables. Although substantial number of studies exist regarding their dynamics once generated, how they are triggered is explained through various plausible initiation mechanisms. Among others, earthquake triggered slope failure that creates submarine landslides (Dadson *et al*., 2005), tropical cyclone-induced sediment suspension (Sequeiros *et al*., 2019), hyperpycnal river plumes that rapidly brings sediment suspension to the submarine canyon head (Keuhl *et al*., 2004; Blum and Hattier-Womack, 2009; Weimer and Slatt, 2007) are to name a few (see Meiburg and Kneller, 2010 and the references therein for in-depth review). Initiation of such dense flows are believed to be not possible over mild-sloped shelves. One of the sediment delivery mechanisms over mild-sloped (0.012, Wright *et al*., 2001) shelves is known as wave- and current-supported turbidity currents (WCSTCs) and requires the energy supplied by external hydrodynamic drivers such as alongshore currents and waves, if waves can penetrate to the shelf floor (Ogston *et al*., 2000; Traykovski *et al*., 2000; Wright *et al*., 2001; Parsons *et al*., 2007). If driven by only alongshore currents, they are referred to as alongshore current-supported turbidity currents (ACSTCs). Particularly in narrow shelves, such as that in Waipou New Zealand, sediment suspension can migrate towards the shelf break where waves loose intensity and alongshore currents become prevalent to keep the sediment in suspension (Ma *et al*., 2008). Also observed in the cited study is the thickening of the sediment suspension which suggests the formation of a self-sustaining turbidity current. The described observations in Ma *et al*. (2008) provides a plausible

scenario as to the generation of a turbidity current from initially slow-moving turbidity that can only survive with the aid of turbulence supplied by alongshore currents and waves. The slow-moving turbidity may perhaps provide -referring to Parker (1982)- the required disturbance for highly erosive turbidity currents. In this regard, critical conditions that transforms ACSTCs to self-sustaining turbidity currents will help augment our understanding of possible sediment mass exchange mechanisms between the shelf and the deep ocean.

To the best of the authors' knowledge, there is only one criterion available in the literature for the inception of self-sustaining turbidity currents originating from the WCSTCs (Wright *et al*., 2001) which proposes a critical slope of 0.012. The proposed criterion is based on the assumption that the sediment-laden flow is critically stratified in WCSTCs, and the bed shear stress is quantified with appropriate choice of drag coefficient (see Wright *et al*., 2001 for details). For WCSTCs and ACSTCs to grow into a possible self-sustaining turbidity current, the erosion rate must exceed the rate of deposition either by the change in slope or erosive characteristics at the sediment bed, such as sediment size and porosity. It follows from this argument that the critical conditions for the inception of the transition from ACSTC to self-sustaining turbidity current must be a function of -as it governs the depositional flux- the sediment settling velocity, erosion parameters, and the shelf slope, which is the main hypothesis that will be tested in this study. Because transition from WCSTCs and ACSTCs to self-sustaining turbidity current is a transient phenomenon, a dynamic relation needs to be developed. It will then be possible to assess whether the dynamic relation of suspended sediment concentration allows for the growth of sediment concentration and thus the downslope force in time. Indeed, such approach was adopted to identify the critical conditions that delineate subsiding and highly erosive turbidity currents (Parker, 1982; Fukushima *et al*., 1985; Parker *et al*., 1986). Cited studies either solved the dynamic relations of

the depth-averaged (or layer-averaged as mentioned in these studies) quantities and/or conducted stability analyses for the depth-averaged dynamic equations (Parker *et al*., 1982).

In this study, we developed a simple dynamic depth-integrated equation of the suspended sediment concentration (SSC) for a sediment bed composed of sediments with uniform size and erosion characteristics along and across the shelf. The developed dynamic equation is analyzed in itself which is followed by its temporal stability analysis. Two different criteria were obtained. The criteria obtained were compared with the simulations in chapter 4, along with the two additional simulations presented herein.

The rest of this chapter is organized as follows. Section 5.2 provides a brief description of the methods. In section 5.3, simulation results that help develop the dynamic equation is described which is followed by the derivation and the analyses of the dynamic equation in Section 5.4. Discussions of the findings and concluding remarks are provided in section 5.5.

5.2. METHODS

This study is in part built upon the simulations presented in chapter 4. In addition to those presented in chapter 4, two simulations were conducted for the purpose of this study. The list of simulations with parameters relevant to the problem herein is given in Table 1. Problem setup and numerical details are described in chapter 4 and will not be repeated herein. However, for better readability, it is necessary to emphasize the following as to the parameters selected. Bed shear stress associated with along-shelf current is specified approximately as $\tau_{bo} = 0.013$ Pa. Thus, corresponding friction velocity, $u_{\tau o} = \left(\tau_{bo}/\rho_f\right)^{1/2}$, is obtained as 3.6×10^{-3} m s^{-1}. Along-shelf current induced bed shear stress is also referred to as initial bed shear stress because with the addition of sediment suspension, bed shear stress is augmented by the cross-shelf motion of the

turbidity. When flow reaches the equilibrium conditions, the magnitude of the bed shear stress, τ_b, becomes

$$\tau_b = (\tau_{bo}^2 + \mathfrak{B}\sin\theta)^{1/2}. \quad (1)$$

In Equation (1), $\mathfrak{B}$ denotes the depth-integrated buoyancy force

$$\mathfrak{B} = \rho_f(s-1)g\langle c\rangle h, \quad (2)$$

where, ρ_f is the density of water, s is the specific gravity of sediments, g is the gravitational acceleration, $\langle c\rangle$ is the depth-averaged volumetric sediment concentration, and h is the flow depth. In the simulations conducted, $\rho_f = \rho_w$ is taken to be $\rho_f = 1000$ kg m^{-3}, sediments are assumed to be of quartz origin and thus $s = 2.65$, the flow depth is taken as $h = 0.1$ m and the gravitational acceleration is $g = 9.81$ m s^{-2}. For erosion flux, E, at the bed, we adopted a Partheniades-Aruthrai type of formulation (Sanford and Ma, 2001) with unlimited sediment supply at the bed which is given as

$$E = m_e S(1-\phi)\,. \quad (3)$$

In Equation (3), m_e is the erosion rate, ϕ is the porosity and $S = (\boldsymbol{\tau}_b/\tau_c - 1)$ is the normalized excess shear stress, where τ_c is the critical shear stress for erosion. Both m_e and ϕ are uniform along and across the shelf with $m_e(1-\phi) = 3.6\times10^{-7}$ m s^{-1}. Because suspended sediment concentration is not known a priori, excess shear stress is specified based on the initial bed shear stress which will be referred to as initial normalized excess shear stress, S_o. Assuming three different critical shear stress values for loose fine sediment deposits, namely $\tau_c = 0.010$ Pa, 0.011 Pa, and 0.012 Pa, initial normalized excess shear stress are obtained as $S_o = 0.05$, 0.11, and 0.25. The porosity of the bed is assumed to be uniform and not affected by erosion. In addition to the bed characteristics, hydrodynamic conditions are also uniform in the cross- and along-shelf

directions. Therefore, the sediment concentration and hydrodynamic variables only vary in the vertical direction and in time. Finally, the sine of the angle of shelf slope (θ) is $\sin\theta = 0.01$.

In the additional simulations, we specified $S_o = 0.11$ and with two different sediment settling velocities, *i.e.*, $w_s = 3.6 \times 10^{-5}$ m s^{-1} and $w_s = 7.2 \times 10^{-5}$ m s^{-1}. The sediment diameter for these two cases are, respectively, $d = 6 \times 10^{-6}$ m and $d = 9 \times 10^{-6}$ m, which are finer than those in chapter 4 (see Table 1 for a complete list). The simulations in chapter 4 were run over a sufficient time period to ensure that the equilibrium conditions are reached and that there is sufficient elapsed time after the equilibrium. In doing so, the mean flow quantities can accurately be calculated and analyzed. However, the additional two simulations conducted herein substantially depart from those in the equilibrium state in that the magnitudes of bed shear stress, cross-shelf velocity, and sediment concentration are far larger without showing any sign of reaching the equilibrium conditions (see Figure 1). Our conclusion is that the flow transitioned to an accelerating state to become self-sustaining and thus the simulations were stopped. Whether the growth of all the variables mentioned is a result of numerical instability may be questioned. However, the Courant-Friedrichs-Lewy (CFL) number was approximately 0.3 at the latest time step for Case B6. More important, the fact that the growth in concentration starts accelerating is a result of the aforementioned transition which will be explained through the dynamic equation of SSC in Section 4.1.

Table 5.1. List of sediment settling velocity (w_s), sediment diameter (d), critical bed shear stress for erosion (τ_c), and the normalized excess shear stress due to along-shelf current (S_o) specified in the simulations. In all the simulations, $sin\,\theta = 0.01$, and $m_e(1-\phi)$ is specified to be $3.6 \times 10^{-7}\, m\, s^{-1}$. Highlighted simulations are concluded to transition from ACSTCs to self-sustaining turbidity currents.

Case Identifier	w_s (m s^{-1})	d (m)	τ_c (Pa)	S_o
0	--		--	--
A1	3.60×10^{-4}	20×10^{-6}	0.010	0.25
A2	2.88×10^{-4}	18×10^{-6}	0.010	0.25
A3	2.16×10^{-4}	15×10^{-6}	0.010	0.25
A4	1.44×10^{-4}	13×10^{-6}	0.010	0.25
B1	3.60×10^{-4}	20×10^{-6}	0.011	0.11
B2	2.88×10^{-4}	18×10^{-6}	0.011	0.11
B3	2.16×10^{-4}	15×10^{-6}	0.011	0.11
B4	1.44×10^{-4}	13×10^{-6}	0.011	0.11
B5	0.72×10^{-4}	9×10^{-6}	0.011	0.11
B6	0.36×10^{-4}	6×10^{-6}	0.011	0.11
C1	3.60×10^{-4}	20×10^{-6}	0.012	0.05
C2	2.88×10^{-4}	18×10^{-6}	0.012	0.05
C3	2.16×10^{-4}	15×10^{-6}	0.012	0.05
C4	1.44×10^{-4}	13×10^{-6}	0.012	0.05

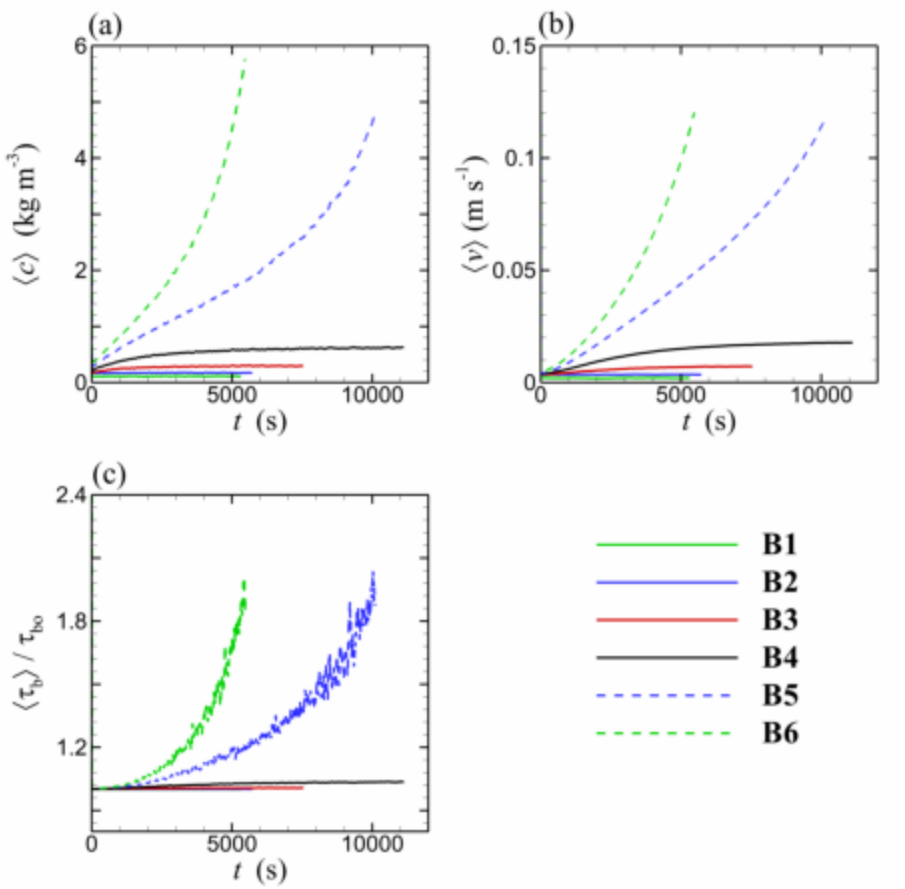

Figure 5.1. Time history of (a) volume-averaged concentration, (b) downslope velocity, and (c) plane-averaged wall shear stress relative to the initial bed shear stress for Cases B1-6.

5.3. SIMULATION RESULTS

The transition of ACSTCs to self-sustaining turbidity currents is closely associated with the amount of sediment that can be suspended by the flow. This is because the shear stress is augmented by the sediment suspension; and if the bed shear stress is sufficient, a continuous feedback between sediment suspension and the bed shear stress may initiate. In fact, it is this continuous feedback mechanism that potentially triggers the self-sustaining turbidity currents. In this regard, quantifying the sediment suspension and the augmentation in the bed shear stress as a function of bed erodibility and the sediment settling velocity will help assess the critical conditions that incepts the self-sustaining turbidity currents. As it will be elucidated, the shape of SSC profiles

and the bed concentration are pivotal for quantifying the total SSC. In the following subsections, our analyses will specifically focus on this aspect.

5.3.1. OVERVIEW: ROLE OF SEDIMENT SETTLING VELOCITY AND EXCESS SHEAR STRESS ON SSC PROFILES

To distinguish the respective roles of erosion and deposition at the bed and turbulent mixing on SSC, a brief discussion on sediment suspension in a steady sediment-laden flow is necessary. In a sediment-laden flow over an erodible bed, equilibrium conditions require a balance between erosion and deposition fluxes at the bed as well as that between the turbulent suspension and settling fluxes in the water column. These two balances are not independent of each other because through erosion, sediments become available for mixing via turbulent suspension. Therefore, total SSC must be governed not only by the parameters that dictate erosion and deposition fluxes, *i.e.*, m_e, S, ϕ and w_s, but also by those that govern the turbulent mixing. Respective roles of mixing and erosion/deposition can be realized from the general form of the analytical sediment concentration profiles, such as the Rouse profile (Rouse, 1937; Vanoni, 1946), given as

$$c(z) = c_o \mathcal{F}(z). \tag{4}$$

Here, $c(z)$ is the depth-dependent concentration, c_o is the reference, or near-bed, concentration and $\mathcal{F}(z)$ is the shape function. The reason we denote $\mathcal{F}$ as the shape function is that it is $\mathcal{F}$ that determines the distribution of SSC in the water column and thus characterizes the shape of SSC profile. While c_o is mostly associated with the bed erosion, $\mathcal{F}$ is mostly linked to turbulence mixing. Total sediment suspension, which is the integral of $c(z)$, must therefore be dependent on both the reference concentration and the shape function.

Governing parameters of turbulent mixing, hence the shape function, can be identified through analyzing the vertical sediment flux balance, which is the vertically integrated advection-diffusion equation of sediment concentration:

$$w_s\overline{c} + \overline{c'w'} = \mathfrak{D}\frac{\mathrm{d}\overline{c}}{\mathrm{d}z}. \tag{5}$$

Here, primes indicate turbulent fluctuations and overbar indicates ensemble-averaged quantities. Using the eddy diffusivity concept, one can approximate the turbulent suspension as a diffusive process:

$$\overline{c'w'} = \mathfrak{D}_t\frac{\mathrm{d}\overline{c}}{\mathrm{d}z}, \tag{6}$$

where $\mathfrak{D}_t$ is the eddy diffusivity. Laminar diffusion term is negligibly small relative to the eddy diffusivity except very close to the bed, and hence Equation (5) further simplifies to

$$\frac{\mathrm{d}\overline{c}}{\mathrm{d}z} = -\frac{w_s\overline{c}}{\mathfrak{D}_t}. \tag{7}$$

Vertical concentration gradient can be considered as a proxy for the SSC profile's shape. As such, it can be inferred that the shape of SSC profile is governed by the sediment settling velocity, w_s, sediment concentration $\overline{c}$, and the intensity of turbulent suspension, correspondingly the eddy diffusivity, $\mathfrak{D}_t$. Another complicating facet as to the mixing is the turbulence destruction through density stratification. Referring to Equation (7), eddy diffusivity will reduce due to dissipation which also changes the shape of SSC profiles. As shown in chapter 4, the reduction in turbulence associated with density stratification is a function of both the settling velocity and the amount of sediment suspension. Therefore, w_s has potentially a more complicated role on total SSC. In regard to described mechanisms that affect total SSC, our analyses will focus on the variation of total SSC with respect to normalized excess shear stress and settling velocity.

To analyze the effect of normalized excess shear stress on the shape of SSC profiles, and the SSC profiles normalized by the bed concentration are plotted in Figure 2, where concentration at the bed can be found in Table 2. In each subfigure of Figure 2, w_s is constant and S_o is variable. For $w_s = 3.6 \times 10^{-4}$ m s^{-1}, normalized SSC profiles almost collapse onto a single profile despite

the variation in excess shear stress. For $w_s = 1.44 \times 10^{-5}\ \mathrm{m\,s^{-1}}$, however, it appears that a slightly larger portion of SSC is in suspension with decreasing S_o. This is chiefly because of the turbulence dissipation due to sediment-induced stable density stratification and is realized from the eddy diffusivity profiles in Figure 2.

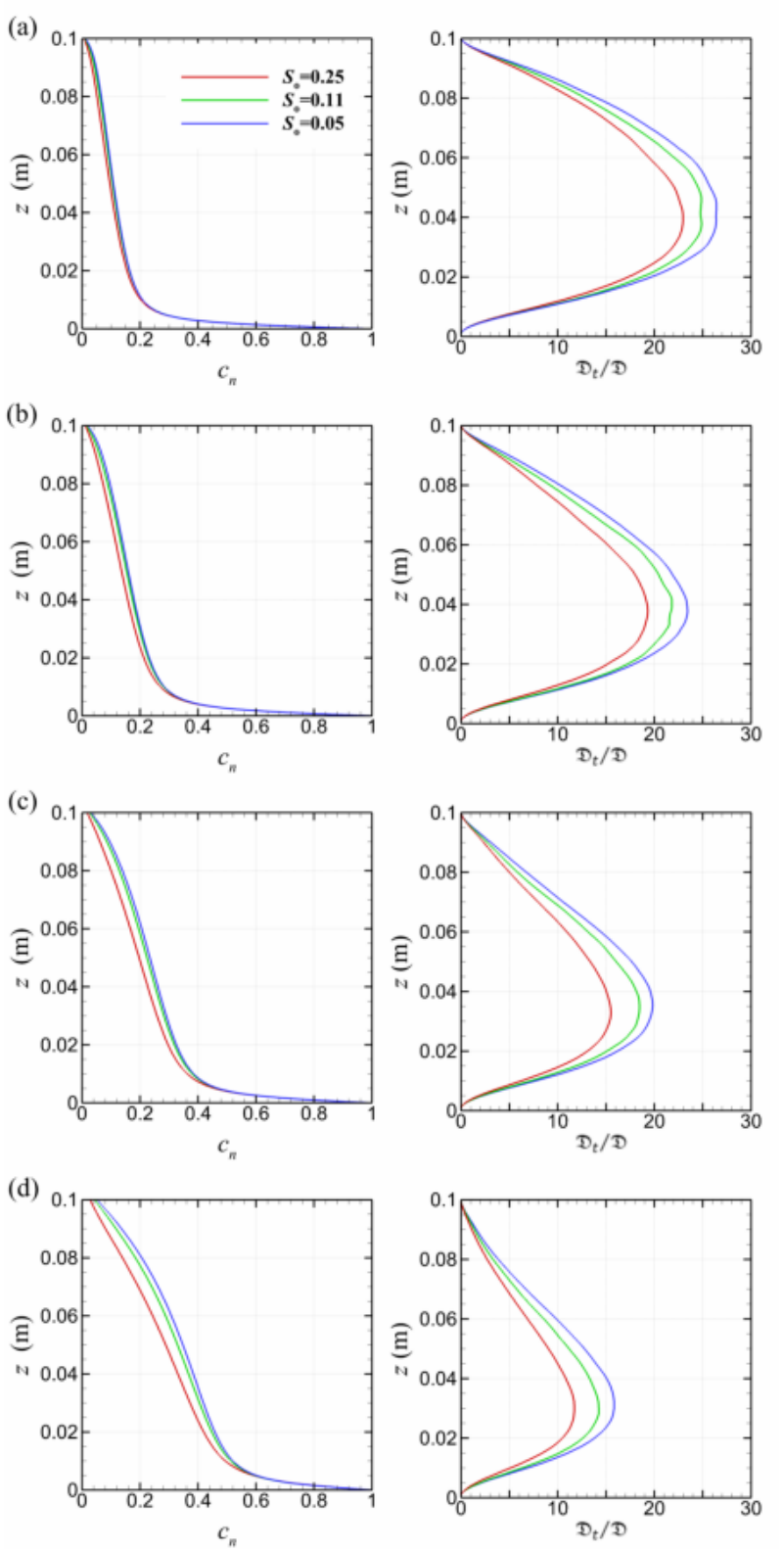

Figure 5.2. SSC profiles normalized by the bed concentration, c_o, (first column) and Eddy diffusivity profiles (second column) for (a) $w_s = 3.6 \times 10^{-5}\ m\ s^{-1}$, (b) $w_s = 2.88 \times 10^{-5}\ m\ s^{-1}$, (c) $w_s = 2.16 \times 10^{-5}\ m\ s^{-1}$, and (d) $w_s = 1.44 \times 10^{-5}\ m\ s^{-1}$.

However, the impact of S_o on the shape of the SSC profiles is minor relative to w_s, which is illustrated in Figure 3. In each subfigure of Figure 3, S_o is constant but w_s is variable. Normalized SSC profiles differ in shape becoming relatively more uniform with decreasing w_s. This occurs even though the eddy diffusivity becomes smaller in magnitude, and the maximum eddy diffusivity moves towards the bed for lower settling velocity (see Figure 3). In other words, turbulent intensity is not sufficient to mix the sediments towards the higher end of w_s values selected in this study.

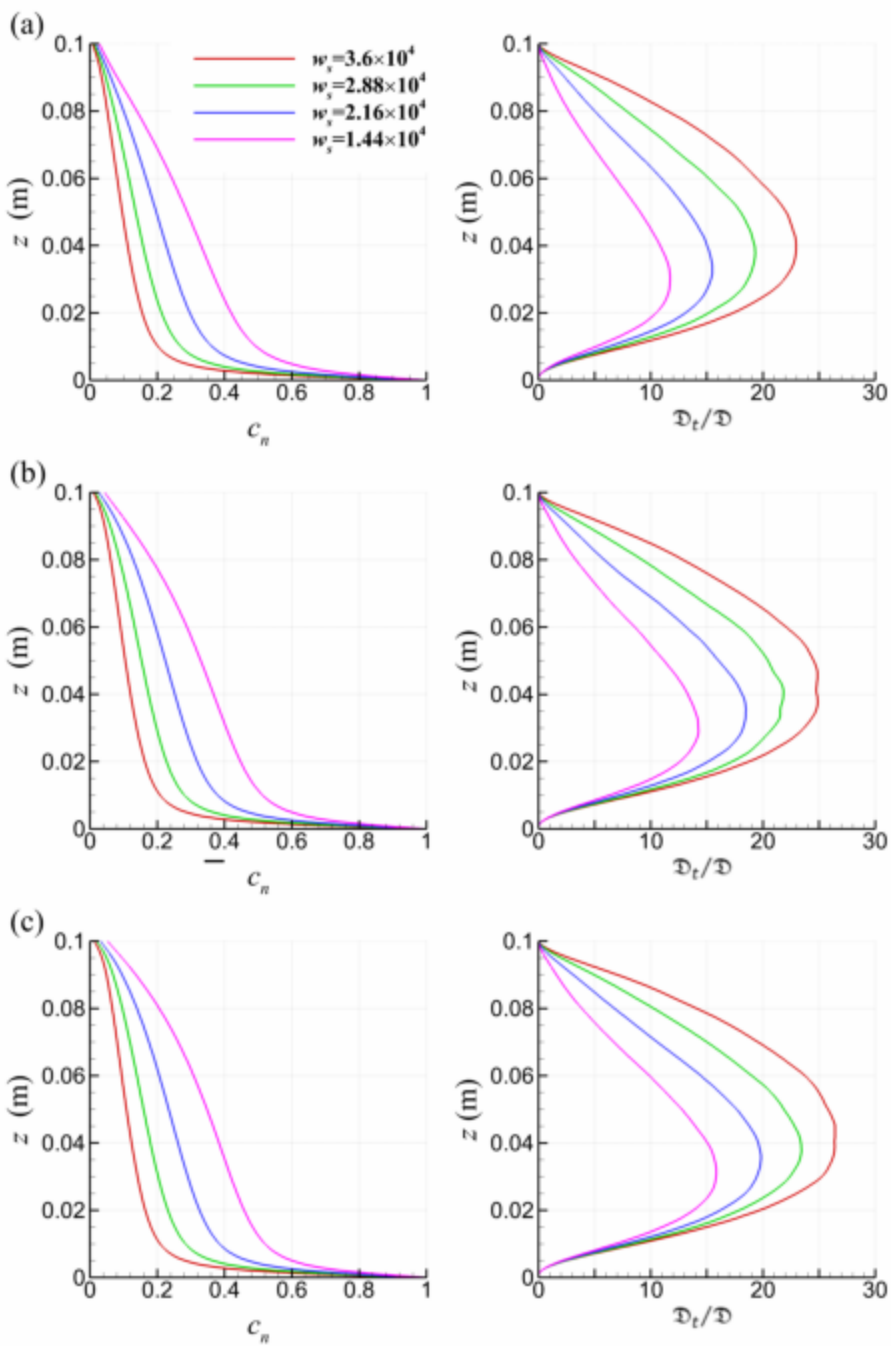

Figure 5.3. SSC profiles normalized by the bed concentration, c_o, (first column) and Eddy diffusivity profiles (second column) for (a) $S_o = 0.25$, (b) $S_o = 0.11$, and (c) $S_o = 0.05$.

The results presented in this section suggest that the shape of SSC profiles is mostly governed by w_s which is slightly modulated by the density stratification for the parameter range herein. It appears that the role of S_o on the shape of SSC profiles is minimal but imposes control on total

SSC through the sediment mass balance at the bed (See Table 2 for c_o values of each simulation). In the following two subsections, variation of total SSC with respect to w_s and erosion parameters will be discussed in detail.

Table 5.2. List of the von Kármán constant (κ), bed concentration (c_o), depth-averaged volumetric sediment concentration ($\langle c \rangle$), and the shape factor (α). Highlighted simulations are concluded to transition from ACSTCs to self-sustaining turbidity currents; therefore, the variables presented cannot be evaluated.

Case Identifier	κ	c_o (kg m^{-3})	$\langle c \rangle$	α (m^{-1})
A1	0.32	0.91	4.14e-05	76.2
A2	0.29	1.14	6.92e-05	55.6
A3	0.26	1.54	0.000127	40.4
A4	0.21	2.61	0.000293	28.8
B1	0.34	0.63	3.09e-05	77.7
B2	0.32	0.79	5.21e-05	57.3
B3	0.29	1.08	9.62e-05	41.8
B4	0.25	1.72	0.000215	30.2
B5	--	--	--	--
B6	--	--	--	--
C1	0.35	0.53	2.67e-05	83.0
C2	0.33	0.68	4.56e-05	62.6
C3	0.31	0.89	8.33e-05	46.3
C4	0.27	1.42	0.000185	33.6

5.3.2. ROLE OF SEDIMENT SETTLING VELOCITY ON DEPTH-AVERAGED SSC

In this section, variation of total SSC with respect to w_s is assessed. Considering that SSC profiles follow the Rouse profile when the density stratification is the least intense, addition of the depth-integrated SSC obtained from the Rouse profiles with respect to w_s will aid in informed interpretation of the results. The Rouse profile is given as

$$\overline{c}(z) = c_o \left[\left(\frac{z}{z_o} \right) \frac{(h - z_o)}{(h - z)} \right]^{-Ro}, \tag{8}$$

where c_o is the reference concentration at the reference height, z_o, and $Ro = w_s/(\kappa u_\tau)$ is the Rouse number. In the analyses to be discussed shortly, we assigned $z_o = 1 \times 10^{-4}$ m so that z_o is sufficiently close to the bed and does not create excessively large concentration due to z/z_o term

in the Rouse profile. We assigned $c_o = m_e(1-\phi)\,S\,w_s^{-1}$ to assess the role of the bed concentration on depth-averaged SSC. It must be emphasized that we use the total SSC obtained from the Rouse profile as a reference and not to validate the simulation results. This is because of the inherent limitation of the Rouse profile due to its sensitivity to z_o value. In this regard, we only compare the trend of the variables obtained from the simulations with those from the Rouse profile.

We first compare the depth-averaged shape function with the SSC profiles normalized by the bed concentration in Figure 4. Given that the von Kármán constant is variable due to density stratification, we use the minimum ($\kappa = 0.21$) and the maximum ($\kappa = 0.35$) of the von Kármán constant observed from the simulations (see Table 2) to compute the depth-average of $\mathcal{F}$, *i.e.*, $\langle\mathcal{F}\rangle$. Both curves that correspond to $\kappa = 0.21$ and $\kappa = 0.35$ shows that the rate of change in $\langle\mathcal{F}\rangle$ strongly depends on w_s/u_τ when w_s/u_τ falls approximately between 5×10^{-3} and 5×10^{-1}. For lower values of w_s/u_τ, $\langle\mathcal{F}\rangle$ becomes almost independent of w_s/u_τ. Our interpretation is that if w_s/u_τ gets lower, SSC profile becomes uniform and the dependency of the shape function on w_s/u_τ vanishes. For relatively higher sediment settling velocity, the shape function becomes dependent on the sediment settling velocity. This dependence gets even stronger with the increase in w_s/u_τ. For w_s range selected herein, $\langle\mathcal{F}\rangle$ falls between the two curves obtained from the Rouse profile. The same range of w_s/u_τ also corresponds to where $\langle\mathcal{F}\rangle$ is highly dependent on w_s. This can also be verified from SSC profiles, where relatively more uniform SSC is observed with decreasing w_s. From the results discussed, the dependence of the shape function on w_s is clear. However, the simulation results, to the extent of the analysis discussed, do not allow for drawing any conclusion regarding the role of density stratification other than its role in modulating the von Kármán constant.

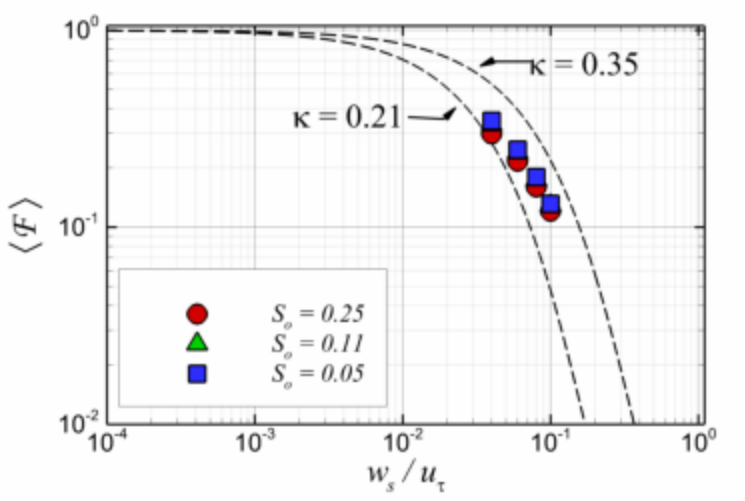

Figure 5.4. Variation of depth-averaged shape function, $\langle \mathcal{F} \rangle$, with respect to w_s/u_τ. The two dashed curves represent $\langle \mathcal{F} \rangle$ obtained from the Rouse profiles with $\kappa = 0.35$ and $\kappa = 0.21$, which are indicated by broken arrows.

Apart from its role on the shape function, w_s imposes control on bed concentration, c_o. This is because of the balance between erosion and deposition fluxes. Referring to the imposed bottom boundary, one can find the bottom concentration as

$$c_o = \left[m_e S(1-\phi) - \mathfrak{D} \frac{\partial \overline{c}}{\partial z}\Big|_{z=0} \right] w_s^{-1}. \tag{9}$$

Equation (9) suggests that total SSC depends on w_s even when the shape function becomes independent of w_s; otherwise, total SSC has a stronger dependence on w_s. With the given considerations, variation of total SSC with respect to w_s/u_τ for both obtained from the Rouse profile and those from the simulations is analyzed in Figure 5. For simplicity, we assume $c_o = m_e S(1-\phi) w_s^{-1}$ for the Rouse profile. We used $\kappa = 0.35$ (solid curve) and $\kappa = 0.21$ (dashed curve) while evaluating the total SSC for the Rouse profiles, which will be referred to as analytical curves. Due to disparate values of S in the simulations, total SSC is normalized by $S(1-\phi)m_e h$ for convenience in presentation. In Figure 5, the rate of change in total SSC obtained from the simulations show similar variation with respect to w_s/u_τ. It must be reemphasized that we use the

Rouse profile only for reference and the match between the simulation results and the analytical curves are subject to change for different values of z_o.

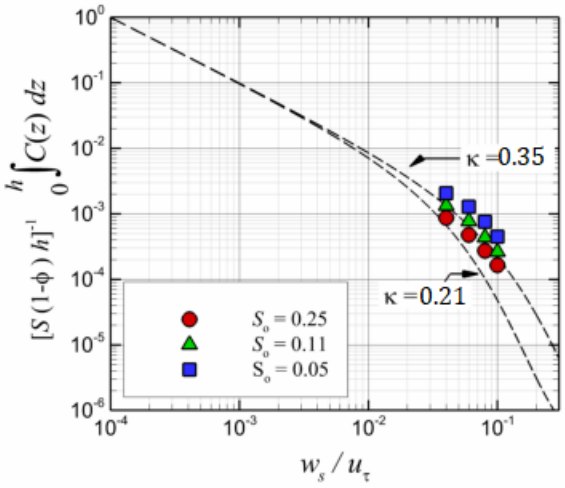

Figure 5.5. Variation of the depth-averaged concentration, normalized by $S(1-\phi)m_e h$, with respect to w_s/u_τ. Normalization factor was chosen for clarity in presentation due to disparate values of S. The two dashed curves represent those obtained from the Rouse profile for $\kappa = 0.35$ and $\kappa = 0.21$, which are the highest and lowest κ observed in the simulations conducted.

The implications of these observations are described as follows. Given that the selected sediment size is larger, and the friction velocity is possibly smaller than commonly observed ACSTCs in the field, a reduced dependence of total SSC on sediment settling velocity is expected for field scale ACSTCs. A more or less uniform sediment concentration would be likely. However, if sediment source is erosion, our analysis suggests a linear dependence on erosion parameters and the inverse of settling velocity, *i.e.*, $\langle c \rangle \sim m_e(1-\phi)\,S\,w_s^{-1}$. The role of density stratification on total SSC is not clearly distinguished from the results other than its role on modulating the von Kármán constant. Analyses that link the eddy diffusivity profiles to parameters that govern the density stratification would be useful but is not within the scope of this study. Nevertheless, at least for the parametric range selected herein, sediment settling velocity and erosion parameters appear to impose much stronger control on total SSC.

5.3.3. ROLE OF BED ERODIBILITY ON DEPTH-AVERAGED SSC

To quantify the increasing bed shear stress, variation of excess shear stress with respect to depth-integrated SSC is analyzed, which is shown in Figure 6. From the same figure, one can observe that at low SSC, excess shear stress is close to that was initially prescribed, *i.e.*, $S \approx S_o$. When $\langle c \rangle \approx 1 \times 10^{-4}$, the deviation between S and S_o is discernable and becomes pronounced with further increase in SSC.

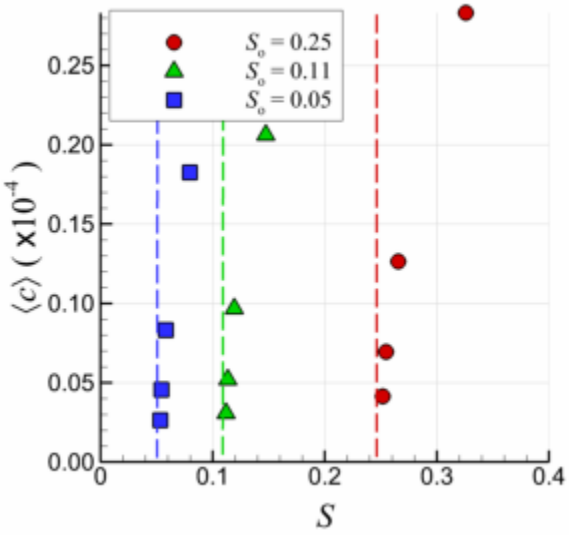

Figure 5.6. Depth-averaged sediment concentration, $\langle c \rangle$, with respect to normalized excess bed shear stress, S. Dashed lines in red, green and blue correspond to the initial normalized excess bed shear stress of $S_o = 0.25$, 0.11, and 0.05, respectively. Sediment mass conscentration approximately ranges between 0.1 $kg\ m^{-3}$ and 0.6 $kg\ m^{-3}$. The dashed lines are drawn to emphasize the increasing deviation of S from their initially prescribed value, *i.e.*, S_o, with increasing sediment suspension and thus the bed shear stress.

The aforementioned deviation can be quantified from the following. Referring to Equation (1), the ratio between the total bed shear stress and the initial bed shear stress is

$$\frac{\tau_b}{\tau_{bo}} = \left[1 + \left(\frac{\mathfrak{B} \sin\theta}{\tau_{bo}}\right)^2\right]^{\frac{1}{2}}. \tag{10}$$

The relation between the total bed shear stress and the downslope force created by the sediment suspension is nonlinear. The nonlinearity mentioned becomes clearer if one expresses the right-hand side (RHS) of Equation (10) as a binomial series sum

$$\frac{\tau_b}{\tau_{bo}} = 1 + \sum_{n=1}^{\infty} \left\{ \left[\prod_{k=1}^{n} \left(\frac{\frac{1}{2}+1}{k} - 1 \right) \right] \left(\frac{\mathfrak{B} \sin\theta}{\tau_{bo}} \right)^{2n} \right\}, \tag{11a}$$

which can be expressed in a more convenient form as in the following:

$$\frac{\tau_b}{\tau_{bo}} = 1 + \frac{1}{2}\left(\frac{\mathfrak{B} \sin\theta}{\tau_{bo}} \right)^2 - \frac{1}{8}\left(\frac{\mathfrak{B} \sin\theta}{\tau_{bo}} \right)^4 + \frac{1}{16}\left(\frac{\mathfrak{B} \sin\theta}{\tau_{bo}} \right)^6 + \cdots. \tag{11b}$$

From Equation (11b), the difference between the total bed shear stress and the initial bed shear stress, *i.e.*, $\Delta\tau_b = \tau_b - \tau_{bo}$, can easily be obtained as

$$\frac{\Delta\tau_b}{\tau_{bo}} = \frac{1}{2}\left(\frac{\mathfrak{B} \sin\theta}{\tau_{bo}} \right)^2 - \frac{1}{8}\left(\frac{\mathfrak{B} \sin\theta}{\tau_{bo}} \right)^4 + \frac{1}{16}\left(\frac{\mathfrak{B} \sin\theta}{\tau_{bo}} \right)^6 + \cdots. \tag{12}$$

Assuming that the higher order terms following the first term on RHS is negligible, Equation (12) can be approximated as

$$\frac{\Delta\tau_b}{\tau_{bo}} \approx \frac{1}{2}\left(\frac{\mathfrak{B} \sin\theta}{\tau_{bo}} \right)^2. \tag{13}$$

Shown in Figure 7, Equation (13) well represents the variation of $\Delta\tau_b$ with respect to $\mathfrak{B} \sin\theta / \tau_{bo}$. In fact, Equation (13) will be used to determine the sediment suspension augmented by the cross-shelf motion, which will be an important term of the dynamic equation that will be described in the next section.

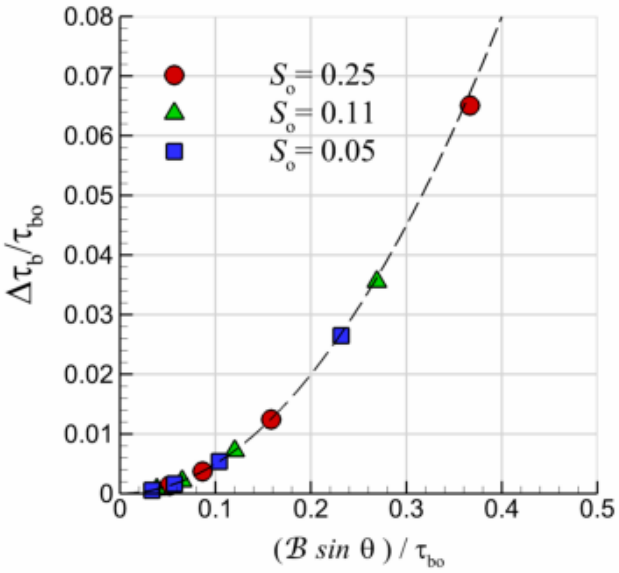

Figure 5.7. Variation of increase in bed shear stress with respect to the downslope bed shear stress. Dashed line compares Equation (13) with those obtained from the simulations. Coefficient of determination is found to be $r^2 = 0.999$.

5.4. TRANSITION OF ACSTCS TO SELF-SUSTAINING TURBIDITY CURRENTS

5.4.1 DYNAMIC EQUATION FOR DEPTH-INTEGRATED SUSPENDED SEDIMENT CONCENTRATION

To cast the dynamic equation for depth-integrated volumetric sediment concentration, c_I, we assume a unit bed area over a shelf. Because the hydrodynamic conditions and the sediment characteristics at the bed are uniform along and across the shelf, there is no variation in concentration in those directions. Therefore, concentration only varies in the vertical direction and in time, unless it is in equilibrium. If concentration is depth-integrated, sediment concentration becomes only a function of time, which is formulated as in the following:

$$\frac{\mathrm{d}c_I}{\mathrm{d}t} = m_e(1-\phi)(S_o + \Delta S) - w_s c_o. \tag{14}$$

Equation (14) simply refers to that the time rate-of-change in c_I is equal to the imbalance between the erosion and deposition fluxes which correspond to the first and the second terms on the RHS of Equation (14), respectively. Erosion flux is created by the excess shear stress due to alongshore

current, *i.e.*, $m_e(1-\phi)S_o$, and the cross-shelf propagation of ACSTCs, *i.e.*, $m_e(1-\phi)\Delta S$ where ΔS is the normalized excess shear stress due to cross-shelf motion of the turbidity. The right-hand side of Equation (14) can be expressed in terms of c_I by utilizing Equations (4) and (13). The bottom concentration (c_o) can be expressed in terms of c_I through shape factor (α) which is obtained after depth-integrating Equation (4):

$$\alpha = \frac{c_o}{c_I} = \left(\int_{z=0}^{z=h} \mathcal{F}(z) dz \right)^{-1}. \tag{15}$$

Similarly, sediment added to suspension through erosion by the cross-shelf propagation can be related to c_I by using Equation (13) where ΔS can be expressed as

$$\Delta S = \left(\frac{1+S_o}{2}\right)\left[\frac{(s-1)g}{u_{\tau o}^2}\sin\theta\, c_I\right]^2. \tag{16}$$

By using Equations (15) and (16), Equation (14) can be re-arranged in the following form

$$\frac{\mathrm{d}c_I}{\mathrm{d}t} = m_e(1-\phi)S_o - (\alpha w_s)c_I + \left\{ m_e(1-\phi)\left(\frac{1+S_o}{2}\right)\left[\frac{(s-1)g}{u_{\tau o}^2}\sin\theta\right]^2 \right\} c_I^2. \tag{17}$$

To be noted, RHS of Equation (17) is a quadratic function of c_I. The implication is that if RHS of Equation (17) does not have real roots, then $\mathrm{d}c_I/\mathrm{d}t > 0$ irrespective of c_I. As a result, c_I will grow indefinitely, suggesting that the system is unstable, and ACSTC will transition to self-sustaining turbidity current (see Figure 8 for graphical illustration). Referring to the description of the unstable case in Figure 8, the analytical solution of Equation (17), if its RHS does not have real roots, is the tangent of time (See Appendix D.1.). In fact, this can also be verified from the time histories of $\langle c \rangle$ obtained from Cases B5-6 in Figure 1. The time history of $\langle c \rangle$ is quite similar to the tangent function. This observation also confirms that increasing sediment concentration, bed shear stress, and cross-shelf velocity in the cases mentioned is not a result of numerical instability but indicates the transition to self-sustaining turbidity current. The implications of Equation (17)

are twofold. First, if Equation (17) is stable one can find the depth-integrated equilibrium concentration, $c_{I,eq}$, when initially there is no sediment suspension. Second, one can obtain the critical conditions for the inception of self-sustaining turbidity currents by evaluating whether RHS of Equation (17) has real roots.

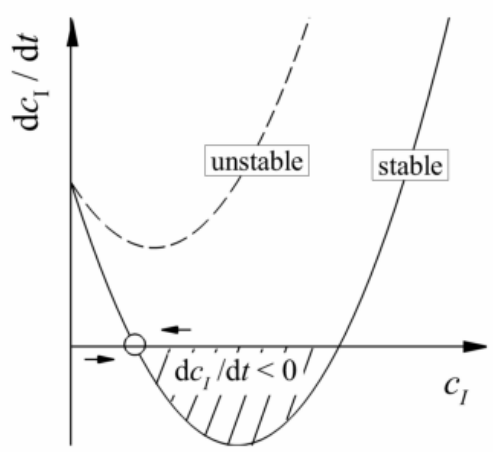

Figure 5.8. Descriptive sketch of c_I versus dc_I/dt for Equation (17). Dashed curve corresponds to a case where right-hand side of Equation (17) has no real roots, and $dc_I/dt > 0$ for $c_I > 0$. In such a case Equation (17) is unstable, and c_I grows indefinitely. Solid curve corresponds to a case where right-hand side of Equation (17) has real roots with shaded area indicating negative dc_I/dt. If initially there is no sediment suspension, *i.e.*, $c_I = 0$, sediment suspension will initially grow and ACSTC will equilibrate at c_I indicated with hollow circle. Upon its increase or decrease, sediment suspension will be forced to return back to the equilibrium concentration because of the negative and positive dc_I/dt, respectively (indicated by the arrows left and right of the hollow circle).

Based on the description given in Figure 8, c_I equilibrates at the smaller root of the quadratic equation on RHS of Equation (17) which is found as

$$c_{I,eq} = (\alpha w_s)\left\{\frac{1-\sqrt{1-\dfrac{2\left[(1-\phi)m_e\dfrac{(s-1)g}{u_{\tau o}^2}\sin\theta\right]^2 S_o(1+S_o)}{(\alpha w_s)^2}}}{m_e(1-\phi)(1+S_o)\left[\dfrac{(s-1)g}{u_{\tau o}^2}\sin\theta\right]^2}\right\}. \tag{18}$$

The equilibrium concentration obtained from the simulations and those estimated by Equation (18) are compared in Figure 9. There is a good agreement between cases with $S_o = 0.25$, but a deviation with decreasing S_o is also noted. The observed mismatch arises because of the diffusive flux at the

bed in the simulations conducted. Particularly when turbulent suspension is low, the diffusive flux starts affecting the total SSC. Nevertheless, with more sediments suspended via turbulence, Equation (18) well predicts the equilibrium concentration. The equilibrium concentration in Equation (18) depends on the sediment settling velocity, slope, and parameters that dictate erosion. In its given form, Equation (18) does not provide a clear to picture as to the role of density stratification. However, contrary to the common notion, sediment-induced density stratification as the sole governing parameter of equilibrium concentration cannot be inferred for the problem herein.

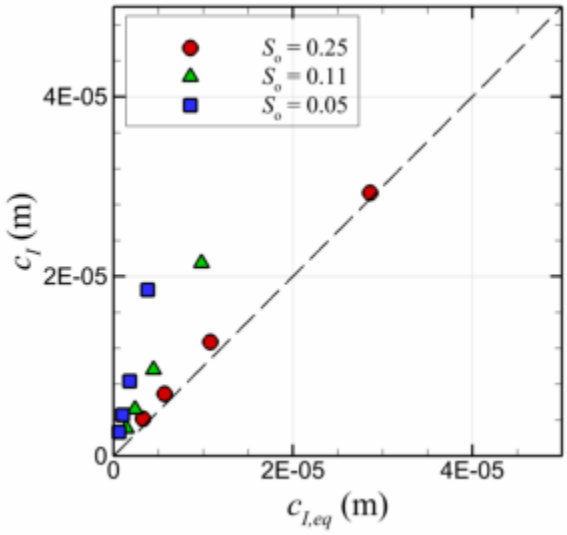

Figure 5.9. Comparison of the depth-integrated concentration estimated by Equation (18), $c_{I,eq}$, against that observed from the simulations. Weakening agreement with decreasing S_o is noted which is a result of the strengthening diffusive flux for these cases.

Equation (17) also brings about a criterion for the onset of transition to self-sustaining turbidity currents from ACSTCs. For stability, the RHS of Equation (17) must have real roots. It follows that its discriminant, Δ, must be greater than zero, where Δ is obtained as flows:

$$\Delta = (\alpha w_s)^2 - 2\left[(1-\phi)m_e \sin\theta \frac{(s-1)g}{u_{\tau o}^2}\right]^2 S_o(1+S_o). \tag{19}$$

Multiplying Δ by c_I^2/c_I^2 followed by straightforward algebraic steps gives the following inequality for stability:

$$\underbrace{\left[\frac{(1-\phi)m_e S_o}{\alpha w_s c_I}\right]}_{I}\underbrace{\left\{\frac{(1-\phi)m_e \sin\theta\,(1+S_o)}{2(\alpha w_s c_I)}\left[\frac{(s-1)gc_I}{u_{\tau o}^2}\right]^2\right\}}_{II} \leq \frac{1}{4}. \tag{20}$$

Note that the above relation is not cast in a compact form to facilitate its physical interpretation. The first term, I, is the ratio between erosional flux created by the alongshore current and the depositional flux. The term I can be regarded as ease of suspension against deposition due to alongshore current because decreasing porosity, increasing erosion rate and excess shear stress all increase the time rate of change in sediment suspension. The only factor for erosion in I is the excess shear stress due alongshore current. Whereas increasing settling velocity and the shape factor leads to enhanced sediment deposition. Referring to Equation (20), the second term, II, can be interpreted as the ease of suspension against deposition due to cross-shelf propagation of ACSTC. Overall, the product of I and II stands for the ease of suspension due to alongshore current which is augmented by the cross-shelf propagation of ACSTCs. In a more compact form, the inception criterion for self-sustaining turbidity current from Equation (19) is given as

$$\mathcal{G} = \frac{m_e(1-\phi)(s-1)g\sin\theta\sqrt{2S_o(1+S_o)}}{(\alpha w_s)u_{\tau o}^2} \leq 1. \tag{21}$$

Comparison of the above criterion with the simulation results is shown in Figure 10. In this comparison, the shape factors are obtained from the simulations except for the two cases where transition to self-sustaining turbidity currents were observed. For these two simulations, the shape factor is conceivably smaller than that obtained from Case B4 because finer sediments can easily be suspended in the water column and become more uniform (see also Figure 4). Nevertheless, to make a conservative estimate, we used α obtained from Case B4. Shown in Figure 10, all stable

cases (cases that remain as ACSTC) satisfy $\mathcal{G} < 1$; whereas for unstable cases, $\mathcal{G} > 1$, even though α is conservatively estimated.

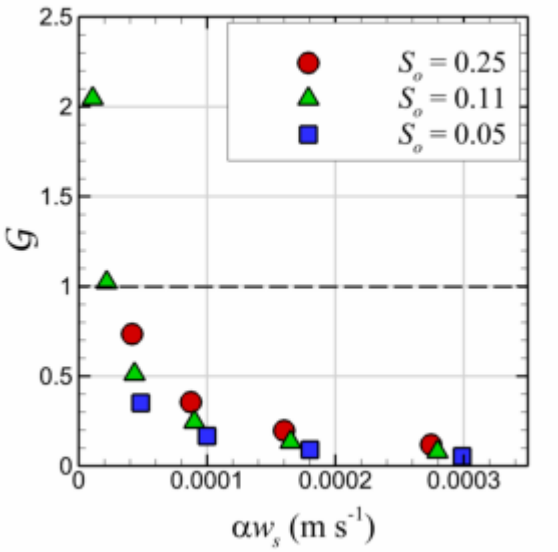

Figure 5.10. Variation of $\mathcal{G}$ (see Equation (21)) with respect to the sediment settling velocity multiplied by the shape factor. Horizontal dashed lines indicate the critical value of $\mathcal{G}$, *i.e.*, $\mathcal{G} = 1$, above which self-sustaining turbidity current occurs. For the two cases that exceeds the critical value of $\mathcal{G}$, simulations indicate the transition from ACSTC to self-sustaining turbidity current (Cases B5-6) and α cannot be obtained. For these two simulations, α is taken to be the same as that in Case B4.

5.4.2. TEMPORAL LINEAR STABILITY ANALYSES

Transition of an ACSTC to self-sustaining turbidity currents can alternatively be estimated via the stability of Equation (17). Equation (17) is a quadratic function of c_I and is therefore nonlinear. Due to nonlinearity, any infinitesimal disturbance in concentration may cause an indefinite growth of c_I that leads to a self-sustaining turbidity current. The growth of infinitesimal concentration disturbance in time is evaluated through temporal linear stability analysis. It is first postulated that the suspended sediment concentration is in equilibrium and the concentration is perturbed with an infinitesimal disturbance, $\tilde{c}$. The disturbance of concentration, $\tilde{c}$, is given as

$$c = c_I + \tilde{c} \quad \text{and} \quad \tilde{c} = \tilde{c}_o \exp(\sigma t), \tag{22}$$

where c is the concentration around equilibrium concentration c_I, *i.e.*, $c \to c_I$ when $\tilde{c} \to 0$. Initial magnitude of $\tilde{c}$ is $\tilde{c}_o$, and σ is the growth rate of concentration disturbance in time. For $\tilde{c}$ to grow σ must be positive. Otherwise, any disturbance in concentration will decay in time until the equilibrium is reached. The governing equation of concentration disturbance is obtained by substituting $c_I + \tilde{c}$ for c and removing the equilibrium equation afterwards. Substituting c into Equation (17) gives

$$\frac{\mathrm{d}(c_I + \tilde{c})}{\mathrm{d}t} = m_e(1-\phi)S_o - (\alpha w_s)(c_I + \tilde{c}) + \left\{ m_e(1-\phi)\left(\frac{1+S_o}{2}\right)\left[\frac{(s-1)g}{u_{\tau o}^2}\sin\theta\right]^2 \right\}(c_I + \tilde{c})^2. \quad (23)$$

After removing the dynamic equation of concentration in equilibrium, the following is obtained

$$\frac{\mathrm{d}\tilde{c}}{\mathrm{d}t} = -(\alpha w_s)\tilde{c} + \left\{ m_e(1-\phi)\left(\frac{1+S_o}{2}\right)\left[\frac{(s-1)g}{u_{\tau o}^2}\sin\theta\right]^2 \right\} 2c_I\tilde{c} + \mathcal{O}(\tilde{c}^2). \quad (24)$$

Because $\tilde{c}$ is infinitesimal initially, $\tilde{c} \gg \tilde{c}^2$ and the second order terms, *i.e.*, $\mathcal{O}(\tilde{c}^2)$, in Equation (24) can be neglected. Thus,

$$\frac{\mathrm{d}\tilde{c}}{\mathrm{d}t} = -(\alpha w_s)\tilde{c} + \left\{ m_e(1-\phi)\left(\frac{1+S_o}{2}\right)\left[\frac{(s-1)g}{u_{\tau o}^2}\sin\theta\right]^2 \right\} 2c_I\tilde{c}. \quad (25)$$

Substituting $\tilde{c} = \tilde{c}_o \exp(\sigma t)$ into Equation (25) and dividing the resultant equation by $\tilde{c}_o \exp(\sigma t)$ gives

$$\sigma = -(\alpha w_s) + \left\{ m_e(1-\phi)(1+S_o)\left[\frac{(s-1)g}{u_{\tau o}^2}\sin\theta\right]^2 \right\} c_I. \quad (26)$$

The stability requires $\sigma < 0$ and thus the stability criterion is obtained as

$$\mathcal{H} = \frac{m_e(1-\phi)(1+S_o)}{\alpha w_s}\left[\frac{(s-1)g}{u_{\tau o}^2}\sin\theta\right]^2 c_I \leq 1\,. \quad (27)$$

If one multiplies Equation (27) by c_I/c_I, it will be clear that $\mathcal{H}$ is twice the ratio of the suspension rate due to cross-shelf propagation to the deposition. Thus, $\mathcal{H}$ can be considered as ease of erosion due cross-shelf propagation of ACSTCs against deposition. The criterion obtained is compared

with the simulation results in Figure 11. Because it is not possible to obtain c_l and α for the cases that are unstable, we used the maxima of α and c_l of the remaining cases with $S_o = 0.11$ as a conservative estimate. While the case with $w_s = 0.01$ gives $\mathcal{H} > 1$, $\mathcal{H}$ is close to the margin for $w_s = 0.02$. It is expected the sediment concentration will increase further for $w_s = 0.02$ leading to an instability. Thus, the criterion posed in Equation (26) also well predicted the transition to self-sustaining turbidity currents in the simulations conducted.

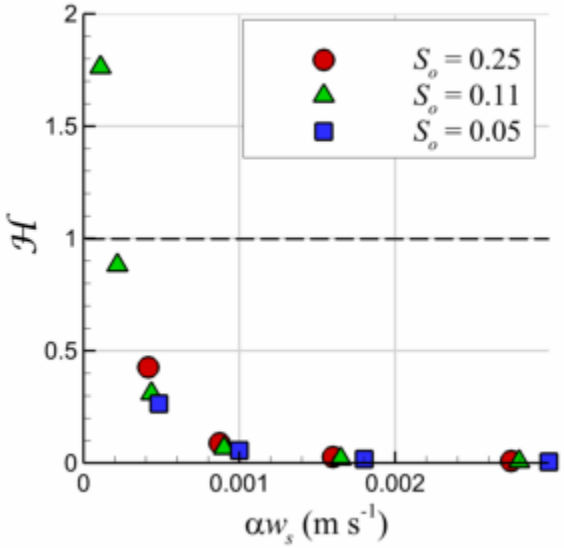

Figure 5.11. Variation of $\mathcal{H}$ (see Equation (27)) with respect to the sediment settling velocity multiplied by the shape factor. Horizontal dashed line indicates the critical value of $\mathcal{H} = 1$ above which self-sustaining turbidity current incepts. For the case that exceeds the critical value of $\mathcal{H}$ simulations indicate the transition from ACSTC to self-sustaining turbidity current (Cases B6). For Case B5 $\mathcal{H}$ is slightly below 1. For Cases B5-6, α and c_l are the same as those in Case B4.

The difference between the criterion obtained in this section, $\mathcal{H}$, and that in section 4.1, $\mathcal{G}$, is the exclusion of the term associated with erosion due to alongshore current in $\mathcal{H}$. The linear stability analysis in this particular problem only considers the growth of concentration disturbance, and erosion due to alongshore current is not a function of sediment concentration. As such, the term associated with the alongshore current is eliminated from the governing equation of the

concentration disturbance. Therefore, the linear stability analysis conducted herein has the limitation of not considering the along-shelf current induced erosion.

5.5. DISCUSSIONS AND CONCLUDING REMARKS

In this study, a simple depth-averaged dynamic equation for sediment concentration is developed for ACSTCs. Time rate-of-change of the depth-integrated concentration, c_I, is obtained to be a quadratic function of c_I, which is nonlinear. Analysis of the equation in itself and its stability analysis rendered two critical conditions for the inception of self-sustaining turbidity currents originating from ACSTCs. The first criterion is the product of the ease of suspension against deposition due alongshore current and that of the cross-shelf propagation of ACSTC. The second criterion, obtained from temporal linear stability analysis, is a measure of the ease of suspension against deposition due to cross-shelf propagation. Both criteria consider the positive feedback loop between the sediment suspension and the bed shear stress. Yet, the first criterion also considers the alongshore current's role on sediment suspension. This is because the linear stability analysis only considers the growth of the concentration disturbance in time. Since the erosion associated with alongshore current is independent of concentration, it is eliminated from the governing equation of concentration disturbance. In this regard, we find the first criterion broader in terms of the physical conditions it covers. In addition, the first criterion does not require the depth-integrated SSC. Nevertheless, both criteria predicted the transition from ACSTCs to self-sustaining turbidity currents.

Another noteworthy observation is related to the criteria associated with the role of sediment settling velocity. With increasing sediment settling velocity, SSC profiles become more skewed towards the bed augmenting the shape factor α. As such, depositional flux, $w_s c_b = \alpha w_s c_I$, becomes a nonlinear function of the sediment settling velocity such that depositional flux becomes

capable of extracting more sediment from suspension making ACSTCs more stable. It must be mentioned that by stability, we refer to ACSTCs preserving their state without transitioning to self-sustaining turbidity current. In fact, the sharp decrease in the stability numbers, *i.e.*, $\mathcal{G}$ and $\mathcal{H}$, with increasing sediment settling velocity clearly illustrates the role of sediment settling velocity.

Apart from the transition criteria, the dynamic equation also estimates the equilibrium concentration when there is no sediment suspension initially. From Equation (18), which estimates the equilibrium concentration, it is not straightforward to assess the role of sediment-induced density stratification. However, the prevalent role of the sediment settling velocity is clear. The simulation results also suggest that depth-integrated concentration reduces with decreasing sediment settling velocity and this dependence becomes even stronger as sediment settling velocity gets larger. For sure the density stratification plays a role, which was observed through the modulation in the von Kármán constant. However, contrary to the common notion, density stratification is not the first-order mechanism to determine the depth-integrated sediment concentration for the problem studied.

The criteria for the inception of self-sustaining turbidity currents from ACSTCs and the equilibrium concentration are found based on the assumption of infinite sediment supply. Whether there is sufficient sediment available in the continental shelf is perhaps highly unlikely. A second limitation is that the erosion rates adopted herein are limited to fine sediments only. Noting that WCSTCs are not limited to fine sediments in the light of the recent observations (Flores *et al*., 2018), it is worth mentioning that the criteria herein are strictly not applicable for seabed with coarse sediment content due to the difference in entrainment formulations. It is particularly important to note that the obtained criteria are restricted to ACSTCs and cannot be extended to

wave-supported turbidity currents. This is because the dynamic equation developed only considers the alongshore currents as the hydrodynamic driver.

6. SUMMARY AND CONCLUSIONS

In this chapter, an overview of the research findings and the answers to the main research questions, along with the recommendations for future studies are included. The current state of knowledge lacks the fundamental knowledge of the role of suspended sediment and bed sediment characteristics on the wave- and current-supported turbidity currents (WCSTCs), particularly when sediment suspension is sourced from the seafloor. In addition, the knowledge on how WCSTC dynamics change under different near-bed turbulence generating mechanisms, such as waves and along-shelf currents, is still limited. Thus, this study aims to identify the role of sediment settling velocity (w_s) and seabed characteristics, *i.e.*, erosion coefficient (m_e), porosity, (ϕ), and critical bed shear stress of erosion (τ_c), on WCSTCs and the resultant cross-shelf fine-sediment transport over an erodible seabed. Direct numerical simulations (DNSs) are conducted to assess the physical processes involved in the dynamics of WCSTCs driven by alongshore currents only.

As mentioned previously, the study of Wright *et al*. (2001) is used as one of the base studies for this dissertation. The main objective of this dissertation was to validate the findings of this study for the case of ACSTC over an erodible bed. The conceptual model proposed by Wright *et al.* (2001) postulates a value range for the drag coefficient, *i.e.*, $C_d \sim 0.003 - 0.005$. However, as it is shown in chapter 3 and chapter 4 of this dissertation, the values observed in our study falls within the range of $C_d \sim 0.002 - 0.004$, where for cases with low settling velocity, high excess shear stress, and thus, high suspended sediment concentration and resultant high stable density stratification, the drag coefficient value falls below the lower limit of the given range by Wright *et al*. (2001). Wright *et al*. (2001) also argued that erosion and deposition are solely governed by the sediment-induced density stratification. It was argued that if there is excess sediment

suspension exceeding the critically stratified conditions, it must settle. Similarly, if the flow is below the critically stratified conditions, suspended sediment deficit must be compensated by the erosion from the bed. The critically stratified condition was quantified by the bulk Richardson number (Ri_b), and it was argued that the critically stratified flow must satisfy $Ri_b = 0.25$. However, our simulation results emphasize the strong role of erosion parameters and sediment settling velocity on the amount of sediment suspension. According to the proposed equation for the equilibrium concentration in chapter 5 of this dissertation, contrary to the assumption of Wright *et al*. (2001), density stratification is not the first-order mechanism to determine the depth-integrated sediment concentration for the problem studied. Lastly, based on proposed $Ri_b = 0.25$ and $C_d = 0.003$, Wright *et al.* (2001) obtained a critical value for the bed slope as $\sin\theta = 0.012$, above which they suggest the transition of WCSTCs to auto-suspending turbidity currents. However, in our simulations, we observed that auto-suspending turbidity currents occur even when $\sin\theta = 0.01$. Perhaps, the reason is that the assumptions made by Wright *et al*. (2001) are too strong. For example, in our simulations $Ri_b \ll 0.25$ even for the lowest settling velocity cases (See Fig. 12 in chapter 3). In addition, the observed drag coefficient falls lower than $C_d = 0.003$ for some cases, which reduces with increasing Ri_b and is a function of Re_τ. Perhaps more important, sediment erosion from the bed or deposition to the bed is not necessarily governed by the sediment-induced density stratification. Thus, this dissertation provides further insights on the parametrization of ACSTCS by introducing new value range for drag coefficient as well as proposing a formula to determine the variation of drag coefficient based on Reynolds number, Richardson number, sediment settling velocity, and the bed slope. Further information is also provided by this dissertation on the possible transition of ACSTCs to self-sustaining turbidity currents. The detailed findings of each chapter are discussed in the following.

The first set of simulations, in Chapter 3, are aimed at evaluating the effect of variable w_s on the flow characteristics of the WCSTCs due only to shore-parallel currents in the absence of waves, *i.e.*, ACSTCs. In this set of simulations, all the parameters are kept constant except for w_s that is chosen within the range of $w_s \sim 0.01 - 0.1$ in its non-dimensional form, which corresponds to a particle size range of $d \sim 6 \times 10^{-6}$ m $- 19.8 \times 10^{-6}$ m. Simulation results suggest that w_s acts as a control on sediment suspension, where volume-averaged suspended sediment concentration is non-linearly related to the inverse of the sediment settling velocity, *i.e.*, $\langle\langle c \rangle\rangle \propto {w_s}^{-1.9}$. In the problem posed, w_s plays a key role in the turbulent characteristics of ACSTCs such that increasing w_s results in decreasing sediment concentration and hence: (i) diminished turbulence production created by the spanwise turbidity current and (ii) less pronounced stable density stratification created by the sediment suspension and the turbulence dissipation. Investigating the effect of various settling velocities on the dynamics of ACSTCs suggests the existence of a critical settling velocity ($w_s < 0.04$) below which the spanwise turbidity current switches its mode from ACSTC to an auto-suspending or self-accelerating turbidity current. In addition, it is shown that with decreasing sediment settling velocity, turbulence production can become a quadratic function of the volume-averaged sediment concentration (Ozdemir and Yu, 2018) which, for the selected erosion parameters and Reynolds number, becomes proportional to $p \propto w_s^{-3.8}$. The transition of a WCSTC to a turbidity current in auto-suspension mode, to the best of our knowledge, has not been reported in any field and laboratory experiments except for the observations in Waipoa Shelf (Ma *et al*., 2010). However, in the mentioned study, the occurrence of the transition is primarily due to the variation of the shelf-slope. In our simulations, the slope is constant, and the transition is due to the excess erosion from the bed, which creates excessive down-slope force.

In the second set of simulations, in chapter 4, we aimed to investigate the velocity structure of a miniature along-shelf current supported turbidity current created via sediment suspension over an erodible bed composed of loose fine sediments. Direct numerical simulations were run for various bed erosion parameters and sediment settling velocities. According to the results, unlike the findings of previous studies (Wright *et al*., 2001), sediment-induced density stratification did not impose the strongest control on the amount of sediment suspension. However, the amount of sediment suspension changes more significantly with respect to sediment settling velocity and bed erosion paraments. Accordingly, the sediment suspension increases with decreasing sediment settling velocity and increased bed erodibility. The effect of density stratification on the velocity structure, however, is observed through the decreasing von Kármán constant in the logarithmic layer and increasing velocity magnitude in the wake layer. It was also shown that the density stratification could be quantified by the product of the sediment settling velocity and concentration, *i.e.*, w_s/u_τ and Ri_τ, respectively. In addition, chapter 4 aimed to develop a relation for the drag coefficient and friction coefficient. According to the results, the drag and the friction coefficients must be equal as long as the mean velocity vector and the principal direction of the bed shear stress (PDBSS) align. Considering the deviation between the mean velocity vector and PDBSS, the difference between the drag and friction coefficients is quantified as a function of $Ri_\tau\, w_s/u_\tau$, and bed slope. Thus, a relation for the drag coefficient as a function of the Reynolds number, the Richardson number, settling velocity, and the slope is proposed in chapter 4.

The last set of simulations, in chapter 5, focuses on developing a depth-averaged dynamic equation for sediment concentration for ACSTCs and determining the critical conditions for the transition of ACSTCs to self-sustaining turbidity currents. In this chapter, an equation for the rate-of-change of the depth-integrated concentration, c_I, based on the quadratic function of c_I is

proposed. Analysis of the equation in itself and its stability analysis suggested two critical conditions for the inception of self-sustaining turbidity currents. While the first criterion is based on the ratio of sediment suspension and deposition due to both alongshore and cross-shelf current, the second criterion is a measure of the ease of suspension against deposition due only to cross-shelf propagation. In this chapter, the role of sediment settling velocity on SSC profiles is specifically investigated. According to the results, with increasing sediment settling velocity, SSC profiles become more skewed towards the bed, augmenting the shape factor α. As such, depositional flux, $w_s c_b = \alpha w_s c_I$, becomes a nonlinear function of the sediment settling velocity, whereas with the increase in sediment settling velocity more sediments are deposited, and ACSTCs become more stable, *i.e.*, lower possibility of transition to self-sustaining turbidity current. The equation proposed for the equilibrium concentration also emphasizes the role of sediment settling velocity, whereas depth-integrated concentration reduces with decreasing sediment settling velocity and this dependence becomes even stronger as sediment settling velocity gets larger. While density stratification plays a role in modulation in the von Kármán constant, its role is not clear through the equilibrium concentration equation. Thus, it is concluded that, contrary to the common notion, density stratification is not the first-order mechanism to determine the depth-integrated sediment concentration for the problem studied.

Several assumptions have been made in this study for both sediment and fluid phases. To further increase the applicability of the present numerical model, future work that does not consider for these assumptions is suggested. The assumptions made in this study is discussed in detail in the following.

1. Grain Size Distribution

Typically, a wide range of particle size exist on the continental shelves. However, due to the complexities associated with mixed sediment-size distribution, the sediment sizing is considered uniform in this study. A well-known phenomenon associated with non-uniform sediment distribution is the winnowing of fine sediments, where coarse sediments act as an armor layer that prevents fine sediment suspension from the bed. This phenomenon can significantly enhance the critical shear stress of erosion and prevent the sediment suspension from the bed (Gomez, 1994; Hong *et al*., 2015). Thus, to get more realistic results that are comparable to the field observations, considering the effect of non-uniform grain size distribution in the WCSTC studies can be a good step for future studies.

2. Sediment-sediment interaction

Another important phenomenon to be considered in future studies is the interaction between sediment particles. In this study, volumetric sediment concentration is considered dilute ($c < 1\%$), sediments are considered to be non-cohesive, and sediment-sediment interactions are considered negligible. Therefore, any physical mechanism particular to cohesive sediments associated with sediment-sediment interaction, such as flocculation, hindered settling, and rheological stresses, are neglected. However, there are many uncertainties related to the physical mechanisms associated with sediment-sediment interactions. For example, how cohesive and non-cohesive sediments interact is still an open question. Particularly, if the sediment concentration reaches high values, the sediment settling velocity can become variable due to flocculation and hindered settling (Richardson and Zaki, 1954; Cheng *et al*. 2015a). Higher settling velocity due to flocculation further increases the effective viscosity and modifies the rheological stresses that change the energy dissipation. In addition, reduced sediment settling due to hindered effect enhances sediment-induced density stratification and results in stronger attenuation of flow

turbulent. Thus, considering the physical mechanisms associated with sediment-sediment interactions is an important step forward to evaluate the dynamics of WCSTCs and resultant sediment transport.

3. The combination of wave- and current-supported turbidity currents

The present study is a systematic study where the effects of waves and currents are investigated individually on the dynamics of WCSTCs. However, waves and currents are likely to present together and operate in concert to suspend sediments and drive WCSTCs. Due to different scale characteristics and the nature of turbulence for waves and currents, their response might be different when they are acting together, and one may affect the other. Previous studies have shown the change in the mean and turbulent characteristics of the current boundary layer due to the superimposition of the waves (Gilberch and Combs, 1963; Sarpkaya, 1966; Lodahl *et al*., 1998). Thus, future studies on WCSTCs when waves and currents co-exist is vital. The results of the present study serve as a benchmark for simulations where waves and currents are present together.

4. Depth-limited erosion

Sediment beds can be broadly divided into two categories: (i) Beds with relatively uniform properties over depth, and (ii) stratified beds in which bed properties, such as bed density and bed shear strength, vary with depth, generally as a result of weight and consolidation. Accordingly, Mehta and Partheniades (1982) introduced two main types of erosion: (i) Unlimited erosion, and (ii) depth-limited erosion. In this study, the assumption of unlimited erosion is adopted, where infinite sediment supply is available. However, in nature, the sediment supply is limited, and the erosion rate generally decreases in time and, in the long run, stops when the bed shear stress equals the critical bed shear stress. Thus, to improve our understanding of physical processes related to

sediment transport, which is highly sensitive to erosion and deposition formulations, the non-uniformity of sediment bed layers needs to be considered in future studies.

5. Bed Roughness

In this study, a smooth bathymetry is considered at the bottom boundary and any effect of bedforms are eliminated. However, In the presence of multi-grain sediment size, roughness elements (bedforms) may form. Bed roughness have the capacity to enhance boundary-layer turbulence and, thus, the sediment carrying capacity of the flow, which further increases the downslope flow speed (Traykovski, 2015; Hooshmand *et al*., 2015). It is conjectured that the roughness height is an effective, perhaps decisive, parameter particularly at sufficiently high Reynolds numbers similar to those in rough, turbulent flows. Thus, considering the formation of bedforms is essential for future studies.

6. Model validation

Experimental and field studies that focus on WCSTCs over an erodible bed are indeed limited, if not missing, in the literature. Thus, further laboratory and field experiments would be preferable for validating the results of the present study. Conventional ocean models in the large scale do not, mostly, account for the wave- and current-induced boundary layer turbulence. However, as it can be conjectured from the results of the present study, sediment transport processes due to WCSTC can result in significant variations in marine geomorphology. Thus, considering the sediment exchange through the interface between the underlying wave- and current-induced turbulent boundary layer and the overlying water column in ocean models is vital. In addition, the transport velocity within the boundary layer needs to be considered to estimate the overall flow velocity. A pioneering study that incorporates the dynamics of WCSTCs into conventional ocean models is provided by Harris *et al*. (2003). They modified the Estuarine and Coastal ocean model-sediment

(Blumberg and Mellor, 1987) by adding a wave boundary-layer grid cell beneath the conventional grid in a three-dimensional model. According to their results, concentrations within the water-column are highly sensitive to the turbulence properties of the turbid layer. Thus, the findings of the present study are essential for the development of more realistic large-scale ocean models.

APPENDIX A. SUPPLEMENTARY MATERIAL TO CHAPTER 2

A.1. COEFFICIENTS OF THE FIRST-ORDER DERIVATIVE COMPACT FINITE DIFFERENCE SCHEME

The coefficients of the general compact scheme for the first-order derivative are:

$$a_j = \frac{(x_j - x_i)\Pi'_m(x_i)}{\Pi_m(x_j)}\{l_j^n(x_i)\}^2, \tag{1}$$

$$b_i = l_i^{m\prime}(x_i) + 2\frac{\Pi'_n(x_i)}{\Pi_n(x_i)}, \tag{2}$$

$$b_j = \{\frac{\Pi_n(x_i)}{\Pi_n(x_j)}\}^2 l_j^{m\prime}(x_i), \tag{3}$$

$$c_j = \frac{\Pi'_m(x_i)}{\Pi_m(x_j)}\{l_j^n(x_i)\}^2\left[1 - \left\{2l_j^{n\prime}(x_j) + \frac{\Pi'_m(x_j)}{\Pi_m(x_j)}\right\}(x_i - x_j)\right], \tag{4}$$

where

$$\Pi'_k(x) = \begin{cases} \Pi_{j\in I_k, j\neq i}(x - x_j) & if\ \ x \in I_k \\ \Pi_k(x)\left(\sum_{j\in I_k}\frac{1}{x - x_j}\right) & if\ \ x \notin I_k \end{cases}, \tag{5}$$

and

$$l_j^{k\prime} = \begin{cases} \frac{\Pi_{l\in I_k\, j}(x - x_j)}{\Pi_{l\in I_k, i\neq j}(x_i - x_j)} & if\ \ x \in I_k \\ l_j^k\left(\sum_{l\in I_k, i\neq j}\frac{1}{x_i - x_j}\right) & if\ \ x \notin I_k \end{cases}. \tag{6}$$

Thus, the coefficients of the first-order derivative for the interior domain for the given points sets of $I_m = \{i-2, i, i+2\}$ and $I_n = \{i-1, i+1\}$ become:

$$a_{i-1} = \frac{(x_i - x_{i-2})(x_i - x_{i+2})(x_i - x_{i+1})^2}{(x_{i-1} - x_{i-2})(x_{i-1} - x_{i+2})(x_{i-1} - x_{i+1})^2}, \tag{7}$$

$$a_{i+1} = \frac{(x_i - x_{i-2})(x_i - x_{i+2})(x_i - x_{i-1})^2}{(x_{i+1} - x_{i-2})(x_{i+1} - x_{i+2})(x_{i+1} - x_{i-1})^2}, \tag{8}$$

$$b_{i-2} = \frac{(x_i - x_{i-1})^2 (x_i - x_{i+1})^2 (x_i - x_{i+2})}{(x_{i-2} - x_{i-1})^2 (x_{i-2} - x_{i+1})^2 (x_{i-2} - x_i)(x_{i-2} - x_{i+2})}, \tag{9}$$

$$b_{i+2} = \frac{(x_i - x_{i-1})^2 (x_i - x_{i+1})^2 (x_i - x_{i-2})}{(x_{i+2} - x_{i-1})^2 (x_{i+2} - x_{i+1})^2 (x_{i+2} - x_i)(x_{i+2} - x_{i-2})}, \tag{10}$$

$$b_i = \frac{1}{x_i - x_{i+2}} + \frac{1}{x_i - x_{i-2}} + \frac{2}{x_i - x_{i-1}} + \frac{2}{x_i - x_{i+1}}, \tag{11}$$

$$c_{i-1} = \frac{(x_i - x_{i-2})(x_i - x_{i+2})(x_i - x_{i+1})^2}{(x_{i-1} - x_{i-2})(x_{i-1} - x_{i+2})(x_{i-1} - x_i)(x_{i-1} - x_{i+1})^2} \left(2 - 2\frac{x_i - x_{i-1}}{x_{i-1} - x_{i+1}} - \frac{x_i - x_{i-1}}{x_{i-1} - x_{i-2}} - \frac{x_i - x_{i-1}}{x_{i-1} - x_{i+2}}\right), \tag{12}$$

and

$$c_{i+1} = \frac{(x_i - x_{i-2})(x_i - x_{i+2})(x_i - x_{i-1})^2}{(x_{i+1} - x_{i-2})(x_{i+1} - x_{i+2})(x_{i+1} - x_i)(x_{i+1} - x_{i-1})^2} \left(2 - 2\frac{x_i - x_{i+1}}{x_{i+1} - x_{i-1}} - \frac{x_i - x_{i+1}}{x_{i+1} - x_{i-2}} - \frac{x_i - x_{i+1}}{x_{i+1} - x_{i+2}}\right). \tag{13}$$

A.2. COEFFICIENTS OF THE SECOND-ORDER DERIVATIVE COMPACT FINITE DIFFERENCE SCHEME

The coefficients of the general compact scheme for the second-order derivative are:

$$a_j = -\left\{\frac{\Pi_m''(x_i)}{\Pi_m(x_j)} l_j^n(x_i) + \frac{2\Pi_m'(x_i)}{\Pi_m(x_j)} l_j^{n\prime}(x_i)\right\} \sum_{r=1}^{n} B_r (x_i - x_j)^r - \frac{2\Pi_m'(x_i)}{\Pi_m(x_j)} l_j^n(x_i) \sum_{r=1}^{n} r B_r (x_i - x_j)^{r-1}, \tag{1}$$

$$b_j = \left\{\frac{\Pi_m''(x_i)}{\Pi_m(x_j)} l_j^n(x_i) + \frac{2\Pi_m'(x_i)}{\Pi_m(x_j)} l_j^{n\prime}(x_i)\right\} \left[1 + \sum_{r=1}^{n} A_r (x_i - x_j)^r\right] + \frac{2\Pi_m'(x_i)}{\Pi_m(x_j)} l_j^n(x_i) \sum_{r=1}^{n} r A_r (x_i - x_j)^{r-1}, \tag{2}$$

$$b_i = \frac{\Pi_n''(x_i)}{\Pi_n(x_i)} + l_i^{m''}(x_i) + 2C_2 + 2\frac{\Pi_n'(x_i)}{\Pi_n(x_i)} l_i^{m'}(x_i) + 2C_1 \left\{ l_i^{m'}(x_i) + \frac{\Pi_n'(x_i)}{\Pi_n(x_i)} \right\}, \tag{3}$$

and

$$c_j = \left\{ \frac{\Pi_n(x_i)}{\Pi_n(x_j)} l_j^{m''}(x_i) + \frac{2\Pi_n(x_i)}{\Pi_n(x_j)} l_j^{m'}(x_i) \right\} \left[1 + \sum_{r=1}^{n} C_r (x_i - x_j)^r \right]$$

$$+ \frac{2\Pi_n(x_i)}{\Pi_n(x_j)} l_j^{m'}(x_i) \sum_{r=1}^{n} r C_r (x_i - x_j)^{r-1}, \tag{4}$$

where

$$\Pi_k''(x) = \begin{cases} 2\Pi_{j \in I_k,} (x - x_j) \left(\sum_{j \in I_k} \frac{1}{x - x_j} \right) & if x \in I_k \\ \Pi_k(x_i) \left(\sum_{j \in I_k} \frac{1}{x - x_j} \right)^2 - \sum_{j \in I_k} \frac{1}{(x - x_j)^2} & if x \notin I_k \end{cases}, \tag{5}$$

and

$$l_j^{k''} = \begin{cases} 2\frac{\Pi_{j \in I_k}(x - x_j)}{\Pi_{j \in I_k, i \neq j}(x_i - x_j)} \left(\sum_{j \in I_k, i \neq j} \frac{1}{x_i - x_j} \right) & if\ x \in I_k \\ l_j^k \left(\left(\sum_{j \in I_k, i \neq j} \frac{1}{x_i - x_j} \right)^2 - \sum_{j \in I_k, i \neq j} \frac{1}{(x_i - x_j)^2} \right) & if\ x \notin I_k \end{cases}, \tag{6}$$

with A_r given as:

$$2A_2 + 2A_1 \{ \frac{\Pi_m(x) l_i^n(x)}{\Pi_m(x_i)} \}' \Big|_{x = x_i} + \{ \frac{\Pi_m(x) l_i^n(x)}{\Pi_m(x_i)} \}'' \Big|_{x = x_i} = 0, \quad i = j \tag{7}$$

$$\sum_{r=1}^{n} A_r \left[(x_j - x_i)^r \left\{ \frac{\Pi_m(x) l_i^n(x)}{\Pi_m(x_i)} \right\}'' \Big|_{x = x_j} + 2r(x_j - x_i)^{r-1} \left\{ \frac{\Pi_m(x) l_i^n(x)}{\Pi_m(x_i)} \right\}' \Big|_{x = x_j} \right]$$

$$+ \left\{ \frac{\Pi_m(x) l_i^n(x)}{\Pi_m(x_i)} \right\}'' \Big|_{x = x_j} = 0, \qquad \forall i, j \in I_n, \quad i \neq j \tag{8}$$

and B_r given as:

$$2B_2 + 2B_1 \{ \frac{\Pi_m(x) l_i^n(x)}{\Pi_m(x_i)} \}' \Big|_{x = x_i} = 1, \qquad i = j \tag{9}$$

$$\sum_{r=1}^{n} B_r \left[(x_j - x_i)^r \left\{ \frac{\Pi_m(x) l_i^n(x)}{\Pi_m(x_i)} \right\}'' \Big|_{x = x_j} + 2r(x_j - x_i)^{r-1} \{ \frac{\Pi_m(x) l_i^n(x)}{\Pi_m(x_i)} \}' \Big|_{x = x_j} \right]$$

$$= 0, \qquad \forall i, j \epsilon I_n, \qquad i \neq j \tag{10}$$

and C_r given as:

$$\sum_{r=1}^{n} C_r \left[(x_j - x_i)^r \left\{ \frac{\Pi_n(x) l_i^m(x)}{\Pi_n(x_i)} \right\}'' \Big|_{x = x_j} + 2r(x_j - x_i)^{r-1} \{ \frac{\Pi_n(x) l_i^m(x)}{\Pi_n(x_i)} \}' \Big|_{x = x_j} \right]$$

$$+ \{ \frac{\Pi_n(x) l_i^m(x)}{\Pi_n(x_i)} \}'' \Big|_{x = x_j} = 0. \qquad j \epsilon I_n, \qquad i \epsilon I_m \tag{11}$$

Thus, the coefficients of the second-order derivative for the interior domain for the given points sets of $I_m = \{i-2, i, i+2\}$ and $I_n = \{i-1, i+1\}$ become:

$$a_{i-1} = 2(x_i - x_{i-2})(x_i - x_{i+2})[B_1^-(2x_i - x_{i+1} - x_{i-1}) + B_2^-(3x_i - 2x_{i+1} - x_{i-1})]$$

$$+ \frac{2(2x_i - x_{i-2} - x_{i+2})(x_i - x_{i+1})(x_i - x_{i-1})[B_1^- + (x_i - x_{i-1})B_2^-]}{(x_{i+1} - x_{i-1})(x_{i-1} - x_{i-2})(x_{i-1} - x_i)(x_{i-1} - x_{i+2})}, \tag{12}$$

$$a_{i+1} = 2(x_i - x_{i-2})(x_i - x_{i+2})[B_1^+(2x_i - x_{i+1} - x_{i-1}) + B_2^+(3x_i - 2x_{i-1} - x_{i+1})]$$

$$+ \frac{2(2x_i - x_{i-2} - x_{i+2})(x_i - x_{i+1})(x_i - x_{i-1})[B_1^+ + (x_i - x_{i+1})B_2^+]}{(x_{i+1} - x_{i-1})(x_{i+1} - x_{i-2})(x_{i+1} - x_i)(x_{i+1} - x_{i+2})}, \tag{13}$$

$$b_{i-2} = \frac{2(x_i - x_{i-1})(x_i - x_{i+1})(x_i - x_{i+2})}{(x_{i-2} - x_{i+1})(x_{i-2} - x_{i-1})(x_{i-2} - x_{i+2})(x_{i-2} - x_i)} \Big\{ C_{12}^- \left(1 + \frac{x_i - x_{i-2}}{x_i - x_{i+1}} + \frac{x_i - x_{i-2}}{x_i - x_{i-1}} \right)$$

$$+ C_{22}^- \left(2 + \frac{x_i - x_{i-2}}{x_i - x_{i+1}} + \frac{x_i - x_{i-2}}{x_i - x_{i-1}} \right)(x_i - x_{i-2}) + \frac{1}{x_i - x_{i+1}} + \frac{1}{x_i - x_{i-1}} \Big\}$$

$$+ \frac{2(x_i - x_{i+1})(x_i - x_{i-1})}{(x_{i-2} - x_{i+1})(x_{i-2} - x_{i-1})(x_{i-2} - x_i)(x_{i-2} - x_{i+2})} [1 + C_{12}^-(x_i - x_{i-2})$$

$$+ \quad C_{22}^-(x_i - x_{i-2})^2], \tag{14}$$

$$c_{i-1} = 2(x_i - x_{i-2})(x_i - x_{i+2})[1 + A_1^-(2x_i - x_{i+1} - x_{i-1}) + A_2^-(x_i - x_{i-1})(3x_i - 2x_{i+1} - x_{i-1})] + \frac{2(2x_i - x_{i-2} - x_{i+2})[1 + A_1^-(x_i - x_{i-1}) + A_2^-(x_i - x_{i-1})^2]}{(x_{i-1} - x_{i+1})(x_{i-1} - x_{i-2})(x_{i-1} - x_i)(x_{i-1} - x_{i+2})}, \quad (15)$$

$$b_i = 2C_{2i} + 2C_{1i}\left\{\frac{2x_i - x_{i-1} - x_{i+1}}{(x_i - x_{i+1})(x_i - x_{i-1})} + \frac{2x_i - x_{i-2} - x_{i+2}}{(x_i - x_{i-2})(x_i - x_{i+2})}\right\} + \frac{2 + 2(2x_i - x_{i+1} - x_{i-1})(2x_i - x_{i-2} - x_{i+2})/(x_i - x_{i-2})(x_i - x_{i+2})}{(x_i - x_{i+1})(x_i - x_{i-1})} + \frac{2}{(x_i - x_{i-2})(x_i - x_{i+2})}, \quad (16)$$

$$c_{i+1} = 2(x_i - x_{i-2})(x_i - x_{i+2})[1 + A_1^+(2x_i - x_{i+1} - x_{i-1}) + A_2^+(x_i - x_{i+1})(3x_i - 2x_{i-1} - x_{i+1})] + \frac{2(2x_i - x_{i-2} - x_{i+2})[1 + A_1^+(x_i - x_{i+1}) + A_2^+(x_i - x_{i+1})^2]}{(x_{i+1} - x_{i-1})(x_{i+1} - x_{i-2})(x_{i+1} - x_i)(x_{i+1} - x_{i+2})}, \quad (17)$$

$$b_{i+2} = \frac{2(x_i - x_{i-1})(x_i - x_{i+1})(x_i - x_{i-2})}{(x_{i+2} - x_{i+1})(x_{i+2} - x_{i-1})(x_{i+2} - x_{i-2})(x_{i+2} - x_i)}\left\{C_{12}^+\left(1 + \frac{x_i - x_{i+2}}{x_i - x_{i+1}} + \frac{x_i - x_{i+2}}{x_i - x_{i-1}}\right) + C_{22}^+\left(2 + \frac{x_i - x_{i+2}}{x_i - x_{i+1}} + \frac{x_i - x_{i+2}}{x_i - x_{i-1}}\right)(x_i - x_{i+2}) + \frac{1}{x_i - x_{i+1}} + \frac{1}{x_i - x_{i-1}}\right\} + \frac{2(x_i - x_{i+1})(x_i - x_{i-1})}{(x_{i+2} - x_{i+1})(x_{i+2} - x_{i-1})(x_{i+2} - x_i)(x_{i+2} - x_{i-2})}[1 + C_{12}^+(x_i - x_{i+2}) + C_{22}^+(x_i - x_{i+2})^2], \quad (18)$$

where:

$$D = 6 + 4(x_{i+1} - x_{i-1})(D_1^+ - D_1^-) - 2(x_{i+1} - x_{i-1})^2 D_1^+ D_1^-, \quad (19)$$

$$A_1^+ D = -4D_1^+ - 2D_1^- + 2(x_{i+1} - x_{i-1})(D_1^+ D_1^- - D_2^+) + (x_{i+1} - x_{i-1})^2 D_2^+ D_1^-, \quad (20)$$

$$A_2^+ D = 4D_1^+ D_1^- - D_2^+ - \frac{2}{(x_{i+1} - x_{i-1})}(D_1^+ - D_1^-) + (x_{i+1} - x_{i-1}) D_2^+ D_1^-, \quad (21)$$

$$A_1^- D = -4D_1^- - 2D_1^+ + 2(x_{i-1} - x_{i+1})(D_1^+ D_1^- - D_2^-) + (x_{i-1} - x_{i+1})^2 D_2^- D_1^+, \quad (22)$$

$$A_2^- D = 4D_1^+ D_1^- - D_2^- - \frac{2}{(x_{i-1} - x_{i+1})}(D_1^- - D_1^+) + (x_{i-1} - x_{i+1}) D_2^- D_1^+, \tag{23}$$

$$B_1^+ D = -\left\{\frac{2}{(x_{i-1} - x_{i+1})} + D_1^-\right\}(x_{i-1} - x_{i+1})^2, \tag{24}$$

$$B_2^+ D = 1 - (x_{i+1} - x_{i-1}) D_1^-, \tag{25}$$

$$B_1^- D = -\left\{\frac{2}{(x_{i+1} - x_{i-1})} + D_1^+\right\}(x_{i+1} - x_{i-1})^2, \tag{26}$$

$$B_2^- D = 1 - (x_{i-1} - x_{i+1}) D_1^+, \tag{27}$$

$$\begin{aligned} C_{1j} D = \frac{(x_{i+1} + x_{i-1} - 2x_j)}{(x_{i+1} - x_j)(x_{i-1} - x_j)} \{10 &+ \frac{4(x_{i+1} - x_{i-1})^2}{\left(x_{i+1} - x_j\right)\left(x_{i-1} - x_j\right)} \\ &+ 2(x_{i+1} - x_{i-1}) \left\{\frac{x_{i+1} - x_j}{x_{i-1} - x_j} - \frac{x_{i-1} - x_j}{x_{i+1} - x_j}\right\} D_1^+ D_1^- \\ &+ D_1^- \left\{4\frac{x_{i+1} + x_{i-1}}{x_{i-1} - x_j} + 4\frac{x_{i+1} + x_{i-1}}{x_{i+1} - x_j} - 2\frac{(x_{i+1} + x_{i-1})^2}{\left(x_{i+1} - x_j\right)^2}\right\} \\ &- D_1^+ \left\{4\frac{x_{i+1} + x_{i-1}}{x_{i-1} - x_j} + 4\frac{x_{i+1} + x_{i-1}}{x_{i+1} - x_j} - 2\frac{(x_{i+1} + x_{i-1})^2}{\left(x_{i+1} - x_j\right)^2}\right\}, \end{aligned} \tag{28}$$

and

$$\begin{aligned} C_{2j} D = 2 &\left\{\frac{1}{(x_{i+1} - x_j)^2} + \frac{1}{(x_{i-1} - x_j)^2} + \frac{1}{(x_{i-1} - x_j)(x_{i+1} - x_j)}\right\} \\ &- 2\frac{(x_{i+1} - x_{i-1})^2}{\left(x_{i-1} - x_j\right)\left(x_{i+1} - x_j\right)} D_1^+ D_1^- \\ &- 2D_1^+ \frac{(x_{i-1} - x_{i+1})}{\left(x_{i-1} - x_j\right)} \left\{\frac{1}{\left(x_{i-1} - x_j\right)} + \frac{1}{\left(x_{i+1} - x_j\right)}\right\} \\ &- 2D_1^- \frac{(x_{i+1} - x_{i-1})}{\left(x_{i+1} - x_j\right)} \left\{\frac{1}{\left(x_{i-1} - x_j\right)} + \frac{1}{\left(x_{i+1} - x_j\right)}\right\}, \end{aligned} \tag{29}$$

with

$$D_1^+ = \frac{1}{x_{i+1} - x_{i-2}} + \frac{1}{x_{i+1} - x_i} + \frac{1}{x_{i+1} - x_{i+2}}, \tag{30}$$

$$D_1^- = \frac{1}{x_{i-1} - x_{i-2}} + \frac{1}{x_{i-1} - x_i} + \frac{1}{x_{i-1} - x_{i+2}}, \tag{31}$$

$$D_2^+ = \frac{2}{(x_{i+1} - x_{i-2})(x_{i+1} - x_i)} + \frac{2}{(x_{i+1} - x_i)(x_{i+1} - x_{i+2})} + \frac{2}{(x_{i+1} - x_{i-2})(x_{i+1} - x_{i+2})}, \tag{32}$$

and

$$D_2^- = \frac{2}{(x_{i-1} - x_{i-2})(x_{i-1} - x_i)} + \frac{2}{(x_{i-1} - x_i)(x_{i-1} - x_{i+2})} + \frac{2}{(x_{i-1} - x_{i-2})(x_{i-1} - x_{i+2})}. \tag{33}$$

APPENDIX B. SUPPLEMENTARY MATERIAL TO CHAPTER 3

B.1. SPECTRAL ANALYSES OF TURBULENT VELOCITY FLUCTUATIONS

The grid resolution adequacy is checked through the spectral analysis of velocity fluctuations in the streamwise and spanwise directions in Fig. A1. Analyses are conducted at the bed-normal distances that correspond to the buffer layer, the log layer, and the far boundary, *i.e.*, $z^+ = 33$, 120, and 240, respectively. The spectral analyses of velocity fluctuations are investigated for Cases 3 and 6.

E_{xx}, E_{yy}, and E_{zz} represent the energy of velocity fluctuations in x-, y-, and z-directions, respectively. For reference, a dashed line that represents the presence of the inertial subrange where Kolmogorov's $-5/3$ scaling applies is also shown. Several orders of decay in the energy of

velocity fluctuations towards the highest wavenumber suggest that the grid resolution is adequate to resolve the smallest scales of the turbulence.

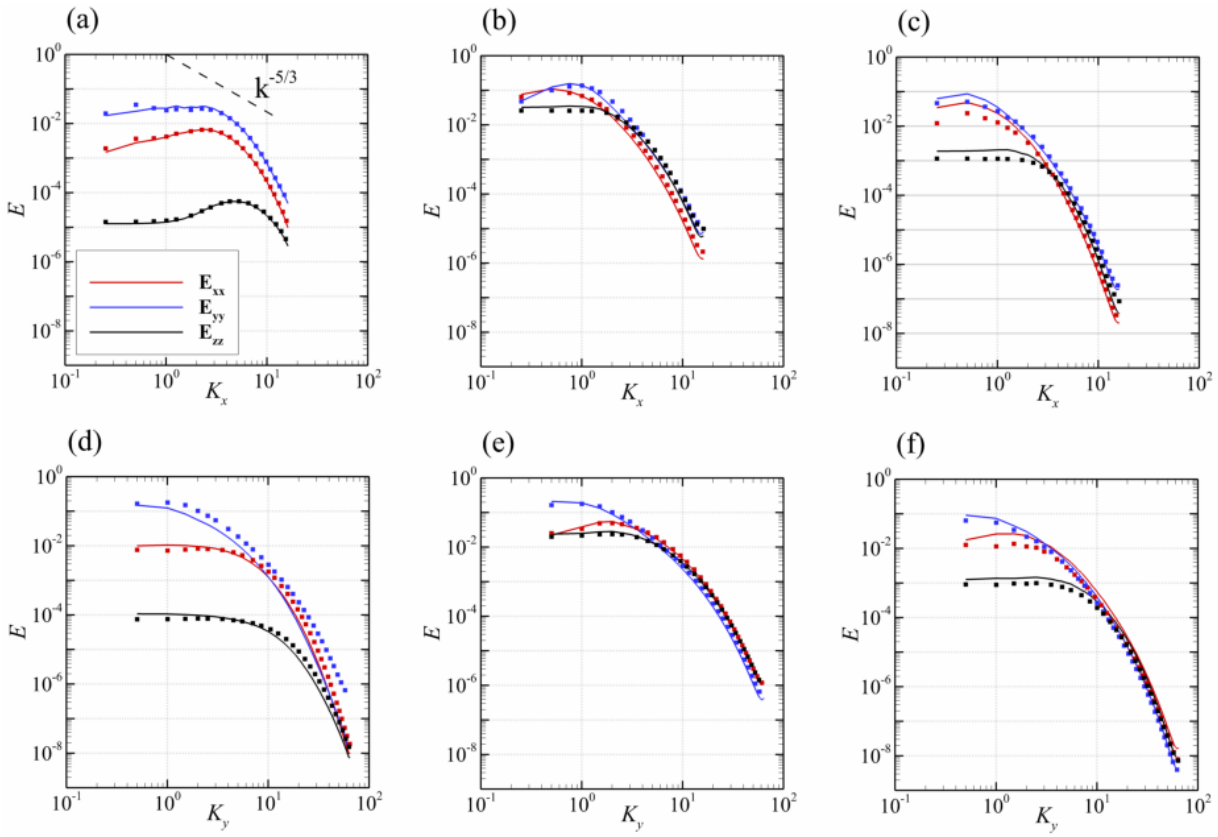

Fig. B1.1. Spectral analyses of velocity fluctuations at (a, d) $z^+ = 33$, (b, e) $z^+ = 120$, and (c, f) $z^+ = 240$. Selected planes respectively correspond to the buffer layer, the log layer, and the far boundary. E_{xx}, E_{yy}, and E_{zz} represent the energy of velocity fluctuations in x-, y-, and z-directions, respectively. Here, $k_x = \pi/\Delta x$ and $k_y = \pi/\Delta y$ are the wavenumbers in x- and y-directions, respectively. The solid curves represent the case with $w_s = 0.1$, and the symbols represent the case with $w_s = 0.04$. The dashed line in subfigure (a) is plotted to check the presence of inertial subrange where the Kolmogorov's -5/3 scaling applies.

B.2. TWO-DIMENSIONAL TWO-POINT CORRELATION ANALYSES

The grid size adequacy is checked through a two-dimensional two-point correlation function in Fig. B1. The two-dimensional two-point correlation is calculated as follows:

$$R_{ii}(r_x, r_y, r_z) = \frac{\overline{u_i'(x + r_x, y + r_y, z)u_i'(x, y, z)}}{K^2}, \quad (1)$$

where r_x and r_y are the separation distances in x- and y-directions, respectively, and $K^2 = \overline{u_j'(x, y, z)u_j'(x, y, z)}$. Here, $i, j = x, y, z$ that correspond to the streamwise, spanwise, and vertical

components, respectively, and the subscript ii denotes the summation over three components. The prime superscript represents the turbulent fluctuations about the mean.

The selected planes are at the bed-normal distances that correspond to the buffer layer, the log layer, and the far boundary, *i.e.*, $z^+ = 33$, 120, and 240, respectively. Three cases with settling velocities of $w_s = 0.1$, $w_s = 0.06$, and $w_s = 0.04$ are selected as representative cases. According to Fig. B1, for all the cases, maximum correlation is located at the center of $r_x - r_y$ planes that decays towards the edges of the domain. Thus, the domain size is sufficient to capture the most energetic turbulent scales.

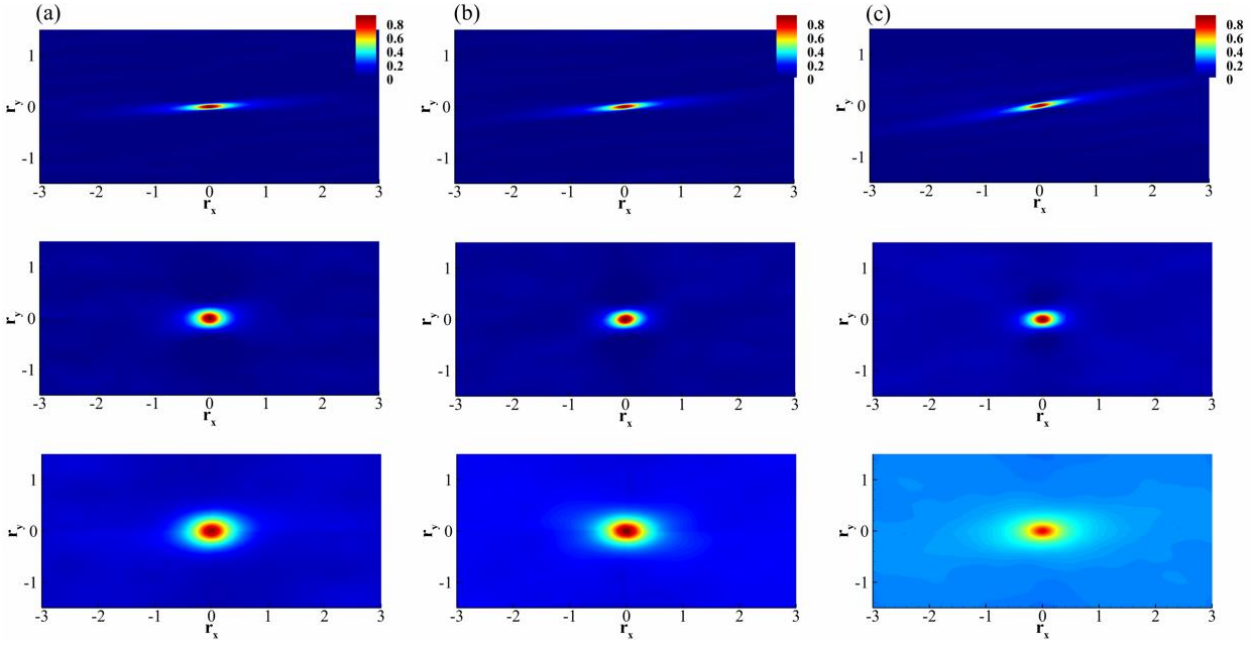

Fig. B2.1 Two-dimensional two-point correlation, R_{ii}, contours of (a) $w_s = 0.1$, (b) $w_s = 0.06$, and (c) $w_s = 0.04$ at $z^+ = 33$ (first raw), $z^+ = 120$ (second raw), and $z^+ = 240$ (third raw). Selected planes correspond to the buffer layer, the log layer, and the far boundary, respectively.

APPENDIX C. SUPPLEMENTARY MATERIAL TO CHAPTER 4

C.1. EVALUATION OF MEAN VELOCITY COMPONENTS WITH RESPECT TO DENSITY STRATIFICATION

This addendum describes how the mean velocity components are evaluated with respect to density stratification. Mean velocity profiles in a turbulent boundary-layer flows are described by the law of the wall and law of the wake (Pope, 2001), which is represented in Equation (27) within the first two and the last terms on the right-hand side of Equation (27), respectively. Strengthening density stratification not only modulates κ but also changes the additive constant, B, wakes strength, Π, and the wake function, $\mathcal{W}(z/h)$. For the evaluation of these variables, we plotted the velocity defect profiles for visual inspection, where the velocity defect is the difference between the free stream velocity, u_o, or the velocity at z/h and the mean velocity profile:

$$\frac{u_o - |\overline{\boldsymbol{u}}|}{u_\tau} - = \frac{u_o}{u_\tau} - \left[\frac{1}{\kappa}\ln\left(\frac{u_\tau z}{\nu}\right) + B + \frac{\Pi}{\kappa}\mathcal{W}\left(\frac{z}{h}\right)\right]. \quad (1)$$

Although the same analyses could have been carried out over the velocity profiles, we chose the velocity defect profiles to be consistent with the literature on this topic. When velocity defect is plotted in semi-log scale, with the logarithm of z/h in the x-axis, the log layer can be distinguished from the linear part of the profile. The left and the right of the log layer are the viscous and the wake layers, respectively. Since the von Kármán constant is evaluated from the Kármán measure profiles, the additive constant becomes the only free parameter to find the best fitting curve in the log layer. The value of B is obtained from the curve that best fits the linear part in the velocity defect profile (see the green curves in Figure B1). The value of the best fit curve at $z/h = 1$ renders Π/κ, which thus evaluates the wake intensity after multiplying it with κ. For non-stratified turbulent boundary layers, an ad hoc approximation of the wake function is $\mathcal{W} = 2\sin^2(\pi z/2h)$

(Pope, 2001). However, our analyses indicate that the wake function mentioned does not accurately represent the velocity in the wake layer. Rather,

$$\mathcal{W}\left(\frac{z}{h}\right) = 2\sin^4\left(\frac{\pi}{2}\frac{z}{h}\right), \tag{2}$$

closely match the velocity profile in the wake layer (See the dashed black curve in Figure A1). List of the von Kármán and additive constants along with the wake strength is given in Table A1.

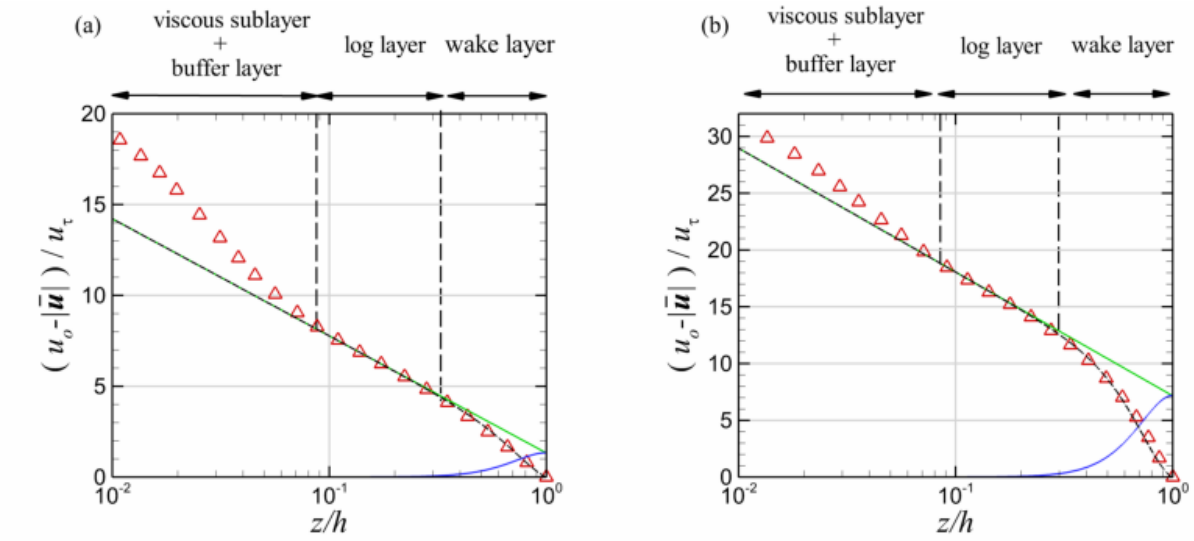

Figure C1.1. Semi-log plots of the velocity defect profile (in symbols) and its components for (a) the least stratified case (Case C1) and the most stratified case (Case A4). Logarithmic and wake profiles are shown in solid green and solid blue curves, respectively.

Table C1.1. List of the von Kármán and additive constants and wake strength values obtained from the simulations.

Case ID	**von Kármán Constant** κ	**Additive Constant** B	**Wake strength** Π
A1	0.32	3.65	0.28
A2	0.29	2.9	0.38
A3	0.26	1.7	0.53
A4	0.21	-0.5	0.76
B1	0.34	4.25	0.25
B2	0.32	3.6	0.37
B3	0.29	2.6	0.5
B4	0.25	1.3	0.77
C1	0.35	4.6	0.24
C2	0.33	3.9	0.32

C3	0.31	3.2	0.47
C4	0.27	1.9	0.72

APPENDIX D. SUPPLEMENTARY MATERIAL TO CHAPTER 5

D.1. ANALYTICAL SOLUTION OF EQUATION (17)

The analytical solutions of Equation (17) is more conveniently discussed if it is written in the following form

$$\frac{\mathbf{d}\boldsymbol{c_I}}{\boldsymbol{m_e}(\mathbf{1}-\boldsymbol{\phi})\boldsymbol{S_o}-(\boldsymbol{\alpha w_s})\boldsymbol{c_I}+\left\{\boldsymbol{m_e}(\mathbf{1}-\boldsymbol{\phi})\left(\frac{\mathbf{1}+\boldsymbol{S_o}}{\mathbf{2}}\right)\left[\frac{(\boldsymbol{s}-\mathbf{1})\boldsymbol{g}}{\boldsymbol{u_{\tau o}^2}}\sin\boldsymbol{\theta}\right]^{\mathbf{2}}\right\}\boldsymbol{c_I^2}}=\mathbf{d}\boldsymbol{t}. \qquad (\mathbf{1})$$

The equation above can be solved after integrating both sides. Note that initially there is no sediment suspension, *i.e.*, $\boldsymbol{c_I}=\mathbf{0}$ when $\boldsymbol{t}=\mathbf{0}$. With the given initial condition, the solution reads

$$\boldsymbol{c_I}(\boldsymbol{t})=\frac{\boldsymbol{\alpha w_s}-\sqrt{|\boldsymbol{\Delta}|}}{\boldsymbol{\alpha w_s}\left\{\boldsymbol{m_e}(\mathbf{1}-\boldsymbol{\phi})(\mathbf{1}+\boldsymbol{S_o})\left[\frac{(\boldsymbol{s}-\mathbf{1})\boldsymbol{g}}{\boldsymbol{u_{\tau o}^2}}\sin\boldsymbol{\theta}\right]^{\mathbf{2}}\right\}}\tanh(\sqrt{\boldsymbol{\Delta}}\boldsymbol{t}), \qquad (\mathbf{2})$$

where $\boldsymbol{\Delta}$ is the discriminant of RHS of Equation (17):

$$\boldsymbol{\Delta}=(\boldsymbol{\alpha w_s})^{\mathbf{2}}-\mathbf{2}\left[(\mathbf{1}-\boldsymbol{\phi})\boldsymbol{m_e}\sin\boldsymbol{\theta}\frac{(\boldsymbol{s}-\mathbf{1})\boldsymbol{g}}{\boldsymbol{u_{\tau o}^2}}\right]^{\mathbf{2}}\boldsymbol{S_o}(\mathbf{1}+\boldsymbol{S_o}). \qquad (\mathbf{3})$$

Note that the term in front of the hyperbolic tangent function on the right is the equilibrium concentration ($\boldsymbol{c_{I,eq}}$). When $\boldsymbol{\Delta}>\mathbf{0}$, $\boldsymbol{c_I}$ converges to $\boldsymbol{c_{I,eq}}$ in time. If $\boldsymbol{\Delta}<\mathbf{0}$, hyperbolic tangent function becomes the tangent function and the concentration diverges to infinity when $\boldsymbol{t}$ approaches to $\boldsymbol{\pi}/(\mathbf{2}\sqrt{\boldsymbol{\Delta}})$.

BIBLIOGRAPHY

Akiyama, J., Fukushima, Y., 1985. Entrainment of non-cohesive bed sediment into suspension. External Memo. No. 175, St. Anthony Falls Hydraulic Laboratory, University of Minnesota, Minneapolis, USA.

Arakawa, A., 1966. Computational design for long-term numerical integration of the equations of fluid motion: Two-dimensional incompressible flow. Part 9. J. Comput. Phys. 1, 119.

Arakawa, A., and Lamb, V. R., 1981. A potential enstrophy and energy conserving scheme for the shallow water equations. Mon. Wea. Rev. 109(1), 18–36.

Armenio V., and Sarkar, S., 2002. An investigation of stably stratified turbulent channel flow using large-eddy simulation. Journal of Fluid Mechanics, 459, 1-42.

Blasius, P. R. H., 1913. Das Aehnlichkeitsgesetz bei Reibungsvorgangen in Flüssigkeiten. Forschungsheft 131, 1–41.

Blum, M. D., and Hattier-Womack, J., 2009. Climate change, sea-level change, and fluvial sediment supply to deepwater depositional systems. External Controls on Deep-Water Depositional Systems.

Blumberg, A. F., and Mellor, G. L., 1987. A description of a three-dimensional coastal ocean circulation model, in Three-Dimensional Coastal Ocean Models, Coastal Estuarine Sci. 4, 1-16.

Boersma, B. J., 2011. A 6th order staggered compact finite difference method for the incompressible navier-stokes and scalar transport equations, Journal of Computational Physics, 230, 4940–4954.

Boyd, J. P., 2001. Chebyshev and Fourier spectral methods, DOVER publication Inc.

Calantoni, J., Holland, K. T., and Drake, T. G., 2004. Modelling sheet-flow sediment transport in wave-bottom boundary layers using discrete-element modelling. Philosophical Transactions–Royal Society of London. Series A: Mathematical, Physical and Engineering Sciences 362, 1987–2002.

Cantero, M. I., Balachandar, S., and Garcia, M., 2008. An Eulerian–Eulerian model for gravity currents driven by inertial particles. Int. J. Multiphase Flow, 34, 484.

Cantero, M. I., Shringarpure, M., and Balachandar, S., 2012. Towards a universal criteria for turbulence suppression in dilute turbidity currents with non-cohesive sediments. Geophys. Res. Lett. 39, 14.

Canuto, C. G., Hussaini, M. Y., Quarteroni, A., and Zang T. A., 2011. Spectral Methods: Fundamentals in Single Domains, Springer.

Canuto, C., Hussaini, M. Y., Quarteroni, A., and Zang, T. A., 1987. Spectral Methods in Fluid Dynamics. Springer.

Cheng, Z., Yu, X., Hsu, T. J., Ozdemir, C. E., and Balachandar, S., 2015a. On the transport of fine sediment in the wave boundary layer due to resuspension/deposition-A turbulence-resolving numerical investigation. J. Geophys. Res. Oceans, 120, 1918–1936.

Cheng, Z., Yu, X., Ozdemir, C. E., Hsu, T. J., and Balachandar, S., 2015b. A Turbulence-Resolving Numerical Model for Fine Sediment Transport in the Bottom Boundary Layer – FINESED3D (Version 1.0).

Chorin, A. J., 1968. Numerical solution of the navier-stokes equations, Math. Comp., 22, 745–762.

Cortese, and Balachandar, S., 1995. High performance spectral simulation of turbulent flows in massively parallel machines with distributed memory. Int. J. Supercomput. Appl. 9(3), 187.

Curran, K., Hill, P., Milligan, T., Mikkelsen, O., Law, B., Madron, X. D., and Bourrin, F., 2007. Settling velocity, effective density, and mass composition of suspended sediment in a coastal bottom boundary layer, Gulf of Lions, France. Cont. Shelf Res., 27, 1408–1421.

Dadson, S. J., Hovius, N., Pegg, S., Dade, W. B., Horng, M. J., and Chen, H., 2005. Hyperpycnal river flows from an active mountain belt. Geology. 32, 733-736.

Dean, R. B., 1978. Reynolds number dependence of skin friction and other bulk flow variables in two-dimensional rectangular duct flow. Journal of Fluids Engineering, 100(2), 215–223.

Deusebio, E., Brethouwer, G., Schlatter, P., and Lindborg, E., 2014. A numerical study of the unstratified and stratified Ekman layer. J. Fluid Mech., 775: 672–704.

Eriksen, C. C., 1978. Measurements and models of fine structure, internal gravity waves, and wave breaking in the deep Ocean. Journal of Geophysical Research: Oceans 83(C6): 2989-3009.

Fain, A., Ogston, A., and Sternberg, R. W., 2007. Sediment transport event analysis on the western Adriatic continental shelf. Continental Shelf Research, 27, 431–451.

Feddersen, F., Guza, R. T., Elgar, S., and Herbes, T. H. C., 2000. Velocity moments in alongshore bottom stress parameterization. Journal of Geophysical Research: Oceans, 105, 8673-8686.

Flores, R. P., Rijnsburger, S., Meirelles, S., Horner-Devine, A. R., Souza, A. J., Pietrzak, J. D.,Henriquez, M., and Reniers, A., 2018. Wave Generation of Gravity-driven Sediment Flows on a Predominantly Sandy Seabed. Geophysical Research Letters. 45: 7634-7645.

Francisco, E. P., Espath, L. F. R., Laizet, S., Silvestrini, J. H., 2018. Reynolds number and settling velocity influence for finite-release particle-laden gravity currents in a basin. Computers and Geosciences. 2018. 110: 1–9.

Friedrichs, C. T., and Wright, L. D., 2006. Gravity-driven sediment transport on continental shelves: A status report. Cont. Shelf Res. 26, 2092.

Fukushima Y., Parker, G., and Pantin H. M., 1985. Prediction of ignitive turbidity currents in Scripps Submarine Canyon. Marine Geology, 67, 55–81.

Garg, R. P., Ferziger, J. H., Monismith S. G., and Koseff J. R., 2000) Stably stratified turbulent channel flows. I. Stratification regimes and turbulence suppression mechanism. Physics of Fluids, 12, 2569.

Geyer, W. R., Hill, P. S., and Milligan T., 2000. The structure of the Eel River plume during floods. Cont. Shelf Res. 20, 2067.

Gilberch D. A., and Combs, G. D., 1963. Critical Reynolds numbers for incompressible pulsating flows in tubes. Developments in Theoretical ad Applied Mechanics. 1, 292-304.

Gomez, B., 1994. Effects of particle shape and mobility on stable armor development. Water Resour. Res. 30(7), 2229–2239.

Grant, W. D., and Madsen, O. S., 1979. Combined wave and current interaction with a rough bottom. J. Journal of Geophysical Research: Oceans, 84, 1979-1808.

Hale, R. P., and Ogston, A. S., 2015. In situ observations of wave-supported fluid-mud generation and deposition on an active continental margin. Journal of Geophysical Research: Earth Surface, 120(11), 2357-2373.

Harris, C. K., Traykovski, P. A., Geyer, W. R., 2003. Including a Near-Bed Turbid Layer in a Three- Dimensional Sediment Transport Model with Application to the Eel River Shelf, Northern California. 18th International Conference on Estuarine and Coastal Modeling.

Harris, C. K., Traykovski, P. A., Geyer, W. R., 2005. Flood dispersal and deposition by near-bed gravitational sediment flows and oceanographic transport: A numerical modeling study of the Eel River shelf, northern California. J. Geophys. Res. 110, 9-25.

Härtel, C., Meiburg, E., and Necker, F., 2000. Analysis and direct numerical simulation of the flow at a gravity current head, Part 1. Flow topology and front speed for slip and no slip boundaries. J. Fluid Mech. 418, 189.

Hermidas, N., Eggenhuisen, J., Jacinto, R. S., Luthi, S. M., Toth, F., and Pohl, F., 2018. A Classification of Clay-Rich Subaqueous Density Flow Structures. J. Geophys. Res. 123, 945-966.

Hong, A., Tao, M., and Kudrolli, A., 2015. Onset of erosion of a granular bed in a channel driven by fluid flow', Physics of Fluids (1994-present). 27(1), 013301.

Hooshmand A., and Horner-Devine, A. R., 2015. Structure of turbulence and sediment stratification in wave-supported mud layers. Journal of Geophysical Research: Oceans, 120. 2430-2448.

Howard, L. N., 1961. Note on a paper of John W. Miles. Journal of Fluid Mechanics 10(4): 509-512.

Hsu, T.-J., Ozdemir, C. E., and Traykovski, P. A., 2009. High-resolution numerical modeling of wave-supported gravity-driven mudflows, J. Geophys. Res., 114, C05014.

Jaramillo, S., Sheremet, a., Allison, M. A., Reed, A. H., and Holland, K. T., 2009. Wave-mud interactions over the muddy Atchafalaya subaqueous clinoform, Louisiana, United States:

Wave-supported sediment transport. Journal of Geophysical Research: Oceans, 114(C4):C04002.

Kuehl, S. A., Brunskill, G. J., Burns, K., Fugate, D., Kniskern, T., and Meneghini, L., 2004. Nature of sediment dispersal off the Sepik River, Papua New Guinea: Preliminary sediment budget and implications for margin processes. Continental Shelf Research, 2.

Lamb, M. P., and Parsons, J. D., 2005. High-Density Suspensions Formed Under Waves. Journal of Sedimentary Research, 75(3):386-397.

Lamb, M. P., Asaro, E. D., and Parons, J. D., 2004. Turbulent structure of high-density suspensions formed under waves. Journal of Geophysical Research, 109(C12):1-14.

Liang, H., Lamb, M. P., and Parsons, J. D., 2007. Formation of a sandy near bed transport layer from a fine-grained bed under oscillatory ow. Journal of Geophysical Research, 112(C2):C02008.

Lodahl, C. R., Sumer, B. M., and Fredsoe, J., 1998. Turbulent combined oscillatory flow and current in a pipe. J. Fluid Mech. 373, 313-348.

Ma, Y., Friedrichs, C. T., Harris, C. K., and Wright, L. D., 2010. Deposition by seasonal wave- and currentsupported sediment gravity flows interacting with spatially varying bathymetry: aiapu shelf, New Zealand. Marine Geology, 275: 199–211.

Ma, Y., Wright, L. D., and Friedrichs, C. T., 2008. Observations of sediment transport on the continental shelf off the mouth of the Waiapu River, New Zealand: Evidence for current-supported gravity flows. Continental Shelf Research, 28(4), 516-532.

Martin, D. P., Nittrouer, C. A., Ogston, A. S, and Crockett, J. S., 2008. Tidal and seasonal dynamics of a muddy inner shelf environment, Gulf of Papua. Journal of Geophysical Research: Oceans, 113, 1-18.

Mehta A. J., Samsami, F., Khare, Y., Sahin, C., 2013. Fluid Mud Properties in Nautical Depth Estimation. J. Waterway Port Coastal and Ocean Engineering. 140, 210- 222.

Mehta, A. J., 1991. Understanding fluid mud in a dynamic environment. Geo-Marine Letters. 1, 113-118.

Meiburg, E., and Kneller, B., 2010. Turbidity currents and their deposits. Annual Review of Fluid Mechanics. 42, 135.

Moin, P., and Kim, J., 1982. Numerical investigation of turbulent channel flow, Journal of Fluid mechanics, 118, 341–377.

Ogston A. S., Sternberg, R. W., Nittrouer, C. A., Martin, P., Gon, M. A., and Crocketti, J. S., 2008. Sediment delivery from the Fly River tidally dominated delta to the nearshore marine environment and the impact of El Nin˜o. Journal of Geophyical. Research: Oceans, 113, 1-11.

Ogston A. S., Sternberg, R. W., Nittrouer, C. A., Martin, P., Gon, M. A., and Crocketti, J. S., 2008. Sediment delivery from the Fly River tidally dominated delta to the nearshore marine environment and the impact of El Nin˜o. J. Geophys. Res. 113, 1-11.

Ogston, A., Cacchione, D., Sternberg, R., and Kineke, G., 2000. Observations of storm and river flood-driven sediment transport on the northern California continental shelf. Cont. Shelf Res., 20(16), 2141–2162.

Ozdemir, C. E., and Yu, X., 2018. Direct numerical simulations of spanwise slope-induced turbidity currents in a fine sediment-laden steady turbulent channel: Role of suspended sediment concentration and settling velocity. Physics of Fluids, 30, 126601.

Ozdemir, C. E., Hsu, T. J., and Balachandar, S., 2010a. A numerical investigation of fine particle laden flow in oscillatory channel: The role of particle-induced density stratification. J. Fluid Mech. 665, 1.

Ozdemir, C. E., Hsu, T. J., and Balachandar, S., 2011. A numerical simulation of lutocline dynamics and saturation of fine sediment in the oscillatory boundary layer. J. Geophys. Res. 116, C09012.

Pantin, H. M., 1979. Interaction between velocity and effective density in turbidity flow: phase-plane analysis, with criteria for autosuspension. Mar. Geol. 31: 59–99.

Parker G., 1982. Conditions for the ignition of catastrophically erosive turbidity currents. Marine Geology 46, 307–27

Parker, G., Fukushima, Y., and Pantin, H. M., 1986. Self-accelerating turbidity currents. Journal of Fluid Mechanics, 171, 145–181.

Parsons, J. D., Friedrichs, C. T., Traykovski, P. A., Mohrig, D., and Imran, J., 2007. The mechanics of marine sediment gravity flows. In Continental Margin Sedimentation: From Sediment Transport to Sequence Stratigraphy, eds.

Peyret, R., 2002. Spectral Methods for Incompressible Viscous Flow. Springer, New York.

Pope S., 2001. Turbulent Flows. Cambridge University Press, ISBN 0-521-59125-2.

Richardson, J., and Zaki, W., 1954. Sedimentation and fluidisation: Part I. Trans. Instn Chem. Engrs. 32(0).

Ross, M. A., and Mehta, A., 1989. On the Mechanics of lutoclines and fluid mud. Journal of Coastal Research, special issue 5, 51–61.

Rouse, H., 1937. Modern conceptions of the mechanics of fluid turbulence. Trans. A.S.C.E., 102.

Sanford, L. P., and Maa, J. P. Y., 2001. A unified erosion formulation for fine sediments. Mar. Geol., 179(1), 9–23.

Sarpkaya, T., 1966. Experimental determination of the critical Reynolds number for pulsating Pouseuille flow. Trans. ASME: J. Basic Engng. 589-598.

Schlatter, P., and Örlü, R., 2010. Assessment of direct numerical simulation data of turbulent boundary layers. J. Fluid Mech., 659 (1), 116–126.

Schlichting, H., and Gersten, K., 2000. Boundary layer theory. Springer.

Scotti, R. S., and Corcos, G. M., 1972. An experiment on the stability of small disturbances in a stratified free shear layer. Journal of Fluid Mechanics 52(3): 499-528.

Scully, M., Friedrichs, C., and Wright L., 2002. Application of an analytical model of critically stratified gravity-driven sediment transport and deposition to observations from the Eel River continental shelf, Northern California, Cont. Shelf Res., 22(14), 1951–1974.

Sequeiros O. E., Pittaluga, M. B., Frascati, A., Pirmez, C., Masson, D., Weaver, P., Crosby, A. R., Lazzaro, G., Botter, G., and Rimmer J. G., 2019. How typhoons trigger turbidity currents in submarine canyons. Science Report, 9, 9220.

Shringarpore, M., Cantero, M. I., and Balachandar, S., 2012. Dynamics of complete turbulence suppression in turbidity currents driven by monodisperse suspensions of sediment. J. Fluid Mech. 712, 384.

Shukla, R. K., Zhong, X., 2005. Derivation of high-order compact finite difference schemes for non-uniform grid using polynomial interpolation. J. Computational Physics. 204. 404-429.

Spalart, P. R., Coleman, G. N., and Johnstone, R., 2008. Direct numerical simulation of the Ekman layer: a step in Reynolds number, and cautious support for a log law with a shifted origin. Phys. Fluids, 20, 101507.

Sternberg, R. W., Cacchione, D. A., Paulson, B., Kineke, G. C., Drake, D. E., 1996. Observations of sediment transport on the Amazon subaqueous delta. Cont. Shelf Res. 20, 2113-2140.

Sternberg, R. W., Kranck, K., Cacchione, D. A., and Drake, D. E., 1988. Suspended sediment transport under estuarine tidal channel conditions. Sed. Geol., 547, 257–272.

Stokes, G. G.,1851. On the effect of internal friction of fluids on the motion of pendulums. Transactions of the Cambridge.

Traykovski, P., Geyer, W., Irish, J., and Lynch, J., 2000. The role of wave-induced density-driven fluid mud flows for cross-shelf transport on the Eel River continental shelf. Continental Shelf Research, 20(16), 2113-2140.

Traykovski, P., Wiberg, P., and Geyer, W. R., 2007. Observations and modeling of wave-supported sediment gravity flows on the Po prodelta and comparison to prior observations from the Eel shelf. Cont. Shelf Res., 27, 375–399.

Traykovski, Trowbridge, P. J., and Kineke, G., 2015. Mechanisms of surface wave energy dissipation over a high-concentration sediment suspension, Journal of Geophysical Research: Oceans, 120, 1638–1681.

Trowbridge, J.H., Kineke, G. C., 1994. Structure and dynamics of fluid mud on the Amazon continental shelf. J. Geophys. Res. 99, 865-874.

Turner, J. S., 1973. Buoyancy effects in fluids. Cambridge University Press, Cambridge. UK.

Van Kessel, T., and Kranenburg, C., 1996. Gravity current of fluid mud on sloping bed. J. Hydraul. Eng.122, 711 – 717.

Vanoni, V.A., 1946. Transportation of suspended sediment by water. Trans. A.S.C.E., 111.

Walsh, J. P., Nittrouer, C. A., Palinkas, C. M., Ogston, A. S., Sternberg, R. W., and Brunskill, G. J., 2004. Clinoform mechanics in the Gulf of Papua, New Guinea. Continental Shelf Research, 24, 2487-2510.

Weimer P., and Slatt R. M., 2007. Introduction to the petroleum geology of deepwater setting. In AAPG Studies in Geology. Tulsa, Oklahoma: American Association of Petroleum Geologists.

Williamson, J.H., 1980. Low-storage Runge-Kutta schemes, J. Computational Physics, 35, 48-56.

Winterwerp, J. C., 2001. Stratification effects by cohesive and non-cohesive sediment. Journal of Geophysical Research: Oceans, 106(C10), 22, 559.

Winterwerp, J. C., 2007. On the sedimentation rate of cohesive sediment, in Estuarine and Coastal Fine Sediments Dynamics. Proceedings in Marine Science, 8, 209–226.

Winterwerp, J. C., Lely, M., and He, Q., 2009 Sediment-induced buoyancy destruction and drag reduction in estuaries, Ocean Dynamics, 59, 781-791.

Wright L. D., Kim, S. C., and Friedrichs, C. T., 1999. Across-shelf variation in bed roughness bed stress and sediment transport on the northern California shelf. Marine Geology, 154, 99-115.

Wright L. D., Wiseman, W. J., Prior, D. B., Suhayda, J. N., Keller, G. H., Yang, Z. S., and Fan, Y. B., 1988. Marine dispersal and deposition of Yellow River silts by gravity driven underflows. Nature, 332, 629-632.

Wright, L. D., & Nittrouer, C. A., 1995. Dispersal of river sediments in coastal seas: Six contrasting cases. Estuaries, 18(3), 494-508.

Wright, L. D., Friedrichs, C. T., Kim, S. C., and Scully, M. E., 2001. Effects of ambient currents and waves on gravity-driven sediment transport on continental shelves. Mar. Geol. 175, 25.

Wright, L. D., Wiseman, W. J., and Yang, Z. S., 1990. Processes of marine dispersal and deposition of suspended silts off the modern mouth of the Huanghe (Yellow River). Cont. Shelf Res. 10, 1.

Wright, L., and Friedrichs, C., 2006. Gravity-driven sediment transport on continental shelves: A status report. Continental Shelf Research, 26(17-18):2092-2107.

Zhang, W., Cui, Y., Santos, A. I., and Hanebuth, T. J. J., 2016. Storm-driven bottom sediment transport on a high-energy narrow shelf (NW Iberia) and development of mud depocenters. Journal of Geophysical Research: Oceans, 121(8), 5751-5772.

VITA

Sahar Haddadian is born in 1989 in Tabriz, Iran. She graduated from University of Tabriz, Tabriz, Iran, with bachelor's degree in Civil-Structural Engineering in 2011. Sahar received her master's degree in 2013 in Civil-Hydraulic Structures Engineering from University of Tehran, Tehran, Iran. As her interest in Civil Engineering grew, she decided to continue her graduate education in Civil-Coastal Engineering at the Department of Civil and Environmental Engineering at Louisiana State University. Her main doctoral work focus is on the numerical modeling of current-supported turbidity currents over erodible bed. Upon completion of her doctorate's degree, she will begin to work in industry as a Coastal Engineer.